ADVANCED DEFECTED GROUND STRUCTURES (DGSs) FOR RADIO-FREQUENCY AND MILLIMETER-WAVE APPLICATIONS

XU SHANSHAN

School of Electrical and Electronic Engineering

A thesis submitted to the Nanyang Technological University
in partial fulfillment of the requirement for the degree of
Doctor of Philosophy

2017

ABSTRACT

The high performance radio-frequency/millimetre-wave filters are highly demanded for modern wireless communication and radar systems. General requirements for high-performance RF filters are low insertion-loss, small form-factor, sharp selectivity, and low manufacturing cost. In the past, substrate integrated waveguide (SIW) has been proven to be effective in integrating planar and non-planar circuits together based on a standard printed circuit board (PCB) to reduce system cost. Inheriting the properties of conventional waveguide, SIW also has good characteristics of low insertion loss, high quality-factor and high power handling capability but with drawback of relative larger circuit size. Meanwhile, defected ground structure (DGS) is an artificial defect on the ground plane. Two unique capabilities of DGS make it a promising solution for filter designs: 1. Prohibiting wave propagation at desired frequencies, namely the stopband property to improve filter selectivity; 2. Slow-wave effect for circuit miniaturization applications.

This work mainly focuses on the fundamental theory and study of DGS, and its applications to conventional microstrip and SIW filter designs. Several novel DGS structures are proposed and used for high performance miniaturized filter designs.

Firstly, a new dual-T DGS is proposed to extend LPF stopband rejection. The DGS is proposed and etched on the ground plane of the transformed radial stub to form a high-performance LPF with wide stopband rejection.

Secondly, a new DGS is co-designed with SIR to form a new asynchronously tuned resonator. It is formed by mixed coupled stepped impedance resonator (SIR) and coplanar waveguide SIR (CPW-SIR) is proposed, analyzed, and applied to the 2.4-/5.2-GHz dual-band filter designs. The CPW-SIR is created using DGS on the ground plane. Fractional bandwidth (FBW) design graph is constructed for the dual-band filter synthesis. Two filter prototypes (first-order and fourth-order) are fabricated and measured, which validate our design theory.

Thirdly, new DGS structures are developed that form resonators when loaded on SIW technology. A novel back-to-back E-shaped defected ground structure (DGS) for miniaturized dual-band substrate integrated waveguide (SIW) bandpass filter designs is proposed. The SIW loaded by novel DGS supports evanescent-mode wave propagation below the cut-off frequency of SIW, while achieves two transmission poles at the passband and two controllable transmission zero points. Furthermore, the novel loading scheme by loading different-sized DGS resonators on two sides of SIW is proposed for dual-band bandpass filter designs. Meanwhile, the balanced DGSs are investigated for mm-Wave filter applications.

Lastly, a 2.4-/5.2-/60-GHz tri-band bandpass filter (BPF) is designed using two-layer PCB technology for the future WLAN and mobile applications. SIR, SIW, DGS, and CPW techniques are mixed-used in the design approach. To accommodate such large frequency ratio with common input/output, a 2.4-/5.2-GHz dual-band BPF and a 60-GHz BPF are separately designed and connected in parallel with auxiliary low-pass filters (LPFs) and BPFs for signal isolation and matching between the RF and mm-wave frequencies.

ACKNOWLEDGEMENTS

This dissertation would not have been possible without the help and support of many people.

First, I would like to thank my advisor, Prof. Goh Wang Ling and Prof. Yeo Kiat Seng. They have invested enormous amount of time in my technical training and their guidance has always been valuable. The motivation and enthusiasm has inspired me to pursue further analysis and understand complex problems.

I would also like to thank Prof. Ma Kaixue who is now at the University of Electronic Science and Technology of China (UESTC). Before he left NTU, Prof. Ma was with Nanyang Technological University. His experience and knowledge of microwave filters provide valuable guidance and direction for my research.

The support and encouragement of my parents, Mr. Xu Donglin and Mrs. Shi Luhong, was a great contributor in completing my Ph.D. degree. I can never forget their support, dedication and unending love throughout my life.

At last, I must thank my husband, Dr. Meng Fanyi, for his continuous support and unequal love in my Ph.D. journey.

ABBREVIATIONS

RFIC	Radio Frequency Integrated Circuit
mm-Wave	Millimeter-Wave
LPF	Low-pass Filter
BPF	Bandpass Filter
HPF	High-pass Filter
BSF	Band-stop Filter
TL	Transmission Line
SIW	Substrate Integrated Waveguide
DGS	Defected Ground Structure
CPW	Co-Planar Waveguide
VNA	Vector Network Analyzer
IL	Insertion Loss
RL	Return Loss
FBW	Fractional Bandwidth
5G	5^{th} Generation

SIR	Stepped Impedance Resonator
WLAN	Wireless Local Area Network
FCC	Federal Communications Commission
CSRR	Complementary Split-Ring Resonators
PBG	Photonic Bandgap
HFSS	High-Frequency Structure Simulator
ADS	Advanced Design System
SOTL	Short, Open, Load, Thru

TABLE OF CONTENTS

LIST OF FIGURES

Chapter 1

Chapter 2

Chapter 3

Chapter 4

Chapter 5

Chapter 6

CHAPTER 1

Introduction

1.1 Background

The radio-frequency (RF) systems have achieved a remarkable advancement at a tremendous speed. It enables realization of low-lost commercial portable wireless communication system, as well as advanced wireless communications for military application, working environment, and security monitoring. As data transferring becomes more bulky and complex, the demand to support high frequency high bandwidth traffic requires a magnificent enhancement of system performance at an exponential rate.

Figure 1.1 shows the bandwidth at different frequency bands. At millimeter-wave (mm-wave) regime, where the available bandwidth is 10-100 times wider than GSM counterparts, it enables high speed wireless links. Besides, at higher frequency, the size of passive components and packaging that forms an important part of most wireless systems, could be designed much more compact and achieve small form-factor for communication chipsets.

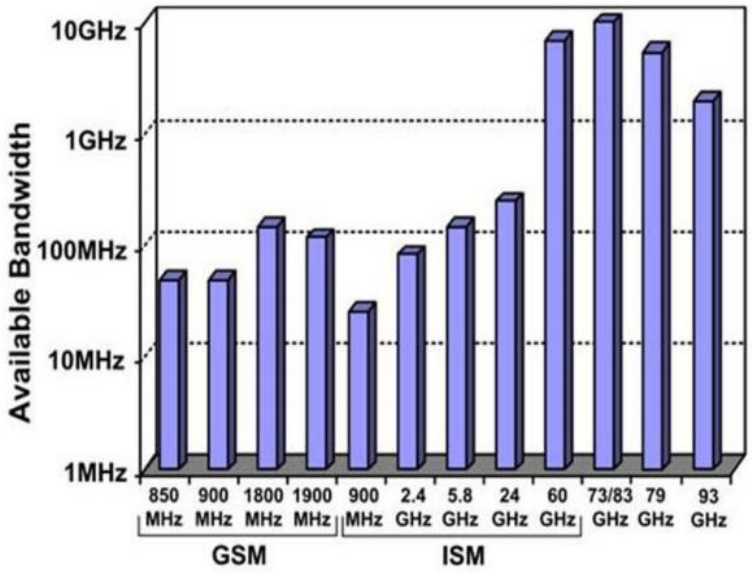

Figure 1.1 Available bandwidth at different bands.

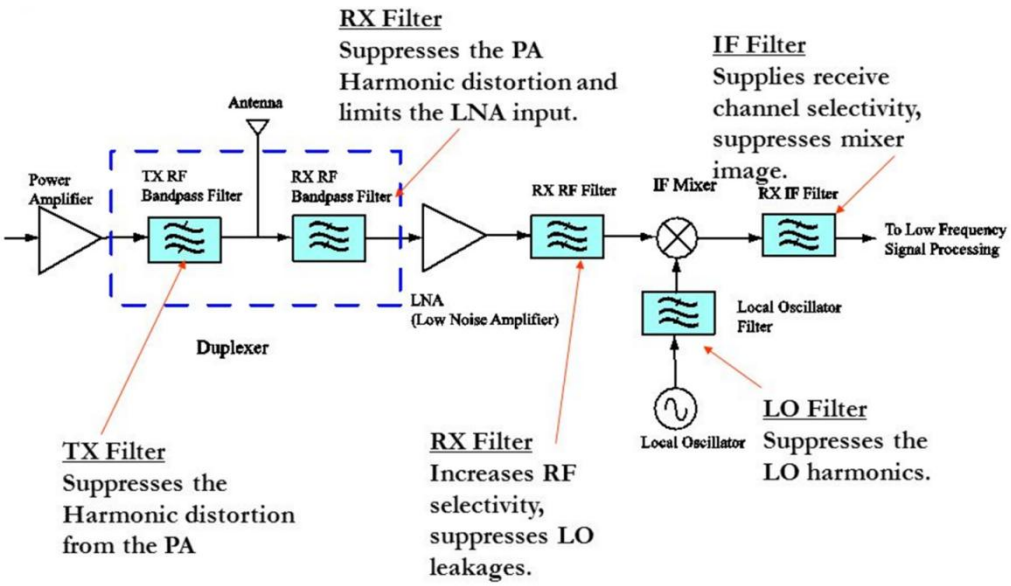

Figure 1.2 Functions of various filters in RF systems.

Microwave filters are a key component in any RF wireless system. It is used to filter off unwanted or spurious signals, as shown in Figure 1.2. Even modern trends if implementing RF systems have been to try to move away from analogue filtering as much as possible and to implement filtering using digital signal processing wherever possible, it is only achievable at lower frequencies where the analogue signal can be successfully migrated into the digital domain. In processing signals at RF frequencies, the conventional approaches to filter designs will still be dominant in a foreseeable future.

The recent advance of novel materials and fabrication technologies, including micro-electromechanic system (MEMS), micromachining, high-temperature superconductor (HTS), and low-temperature cofired ceramics (LTCC), has stimulated the rapid development of new microstrip and other filters. In the meantime, advances in computer-aided design (CAD) tools such as full-wave electromagnetic (EM) simulators have revolutionized filter design. Many novel microstrip filters with advanced filtering characteristics have been demonstrated. The challenges are the optimization between size, performance, cost, as well as requirements from recent multi-band systems.

1.2 Miniaturized Filters

In mobile or portable applications, the system size is of top priority. Being one of the commonly used components, it is undeniable tread that filters tend to be implemented as compact as possible. Microstrip filters are already small in

size compared with other filters, such as waveguide filters. Nevertheless, smaller microstrip filters are still desirable, even though reducing the size of a filter generally leads to an increase in dissipation losses in a given material and, consequently, reduced performance. Miniaturization of microstrip filters may be achieved by using high dielectric constant substrates or lumped elements [1-39]. However, very often, for specified substrates, a change in the geometry of filters is required and, therefore, numerous new filter configurations become possible.

It is known that due to the resonator size requirements, filters are not possible to shrink forever. Currently, the popular approach is to use new fabrication technologies, like the multi-layer PCB, LTCC, and etc. To use lump element also reduces the filter size. And most frequently, designers tend to use folded resonator structures and slow-wave structures to further reduce the filter sizes.

1.3 Multi-Band Filters

The intention to develop multi-band filters is to accommodate multi-band RF systems, without increasing the overall system form-factor which is true if multiple single-band filters are used. It is inevitable that most of our current RF systems tend to operate in multiple frequency bands, like the 2.4-GHz and 5.2-GHz WLAN band, the sub-GHz systems, the 24-GHz and 77-GHz automotive

radars, and etc. Thus, the development of high-performance multi-band filters is a must in the next decades.

In literature, a multiband bandpass filter (BPF) is intuitively implemented with separate filtering paths [1, 23, 40, 41]. In [23], two different-sized complementary split-ring resonators (CSRR) were parallel loaded on surface of the substrate integrated waveguide (SIW) to obtain a dual-band frequency response. In [41], a dual-band filter was designed utilizing multilayer ceramic technology by combining two separate BPFs with matching networks. However, these filters take advantages of waveguide structures and multilayer technology. Indeed if transmission line (TL) based implementations is adopted, this parallel filtering paths topology leads to area overhead [4, 42].

In general, TL-based multiband filters utilize multimode resonators [3, 4, 6, 9, 31, 32]. In [31], a generalized single-band to multiband frequency mapping technique was developed. Several multiband filters were synthesized by loading the hairpin and the meandered resonators to the conventional single-band parallel-coupled half-wavelength resonator filters. In [3], a series of multiple stubs loaded ring resonators were reported for dual-, tri-, and quint-band BPF designs. In the past, due to its design flexibility, stepped impedance resonator (SIR) is widely deployed for multiband filter applications [4, 6, 9, 32]. In [32], several dual-band filters were realized with magnetic coupling between the adjacent SIRs. In [6] and [9], the coupled three-section SIRs were theoretically investigated and experimentally verified for dual-band BPF designs.

1.4 Motivation and Objectives

Great interest in the miniaturized and multi-band filters has been aroused both from the academic and the industrial areas. Researchers or filter designers all over the world are aiming for better performance in terms of filter loss, size, and functionality. The properties of slow-wave effects and multi-mode resonators guarantee potential applications in microwave filter designs. The amazes and challenges of miniaturized and multi-band filter designs actually draw the designers' passions.

The high performance RF/millimeter-wave circuits are highly demanded for modern wireless communications which emphasized a great deal of attention on compact size, low cost and high performance. In addition, the noise issues are very important which are closely related to the loss, efficiency, and impedance matching of the front-end structures. It is important for filters to have high performance with compact size, low insertion loss and good selectivity which means sharper transition knees. For its bandgap property and slow-wave effect, DGS is a promising technique for the above high performance filter designs and can be used to achieve better filter performance while maintain a compact size. On the other hand, SIW has good characteristics inheriting from rectangular waveguide and makes it a suitable platform to integrate with other planar structures such as microstrip, CPW and slot line, allowing hybrid and monolithic design. Therefore, the author finds it interesting and highly beneficial to incorporate DGS technique with SIW waveguide.

The objective of this thesis is to study the effect of the DGS on the wave propagation, and to propose and investigate novel DGS structures suitable for conventional TL as well as SIW integration. The detail objectives are listed as below:

- Understand the fundamental properties of DGSs
- Propose novel DGSs for filter design and miniaturization
- Develop new and high-performance filter solutions for the latest RF/mm-Wave standards

1.5 Organization of the Dissertation

The dissertation is organized as follows.

Chapter 2 provides a literature review on the various filter design techniques. Various DGSs are studied based on the resonant properties. SIW is investigated and reviewed for filter applications. In addition, SIR is studied based on its fundamental resonant properties for miniaturized/multi-band filter applications. As a result of the literature review, the design approaches are identified.

Chapter 3 describes a new dual-T DGS for LPF spurious rejection. The DGS is proposed and etched on the ground plane of the transformed radial stub to form a high performance LPF with wide stopband rejection. The designed result shows an insertion loss of less than 0.5 dB from DC to 2.0 GHz, the

stopband rejection of better than 20 dB from 2.5 GHz to 35 GHz and a sharp skirt selectivity. The size of the proposed LPF is only 2.19 cm × 1.25 cm.

Chapter 4 proposes a new DGS co-designed with the SIR to form a new asynchronously tuned resonator. The resonator formed by mixed coupled stepped impedance resonator (SIR) and coplanar waveguide SIR (CPW-SIR) is proposed, analyzed, and applied to the 2.4-/5.2-GHz dual-band filter designs. The CPW-SIR is created using DGS on the ground plane. Fractional bandwidth (FBW) design graph is constructed for the dual-band filter synthesis. Two filter prototypes (first-order and fourth-order) are fabricated and measured, which validate our design theory. Both filters have good measured results in an agreement with our design target and simulated results. The fourth-order filter features an insertion loss of 1.7 dB at 2.42 GHz with a 3-dB FBW of 0.12 at 2.4-GHz band and an insertion loss of 2.95 dB at 5.26 GHz with a 3-dB FBW of 0.10 at 5.2-GHz band. The return losses are better than 10 dB for both passbands. The designed filter shows a sharp roll-off and high inter-band isolation better than 28 dB. The upper stopband achieves better than 15 dB rejection up to 10 GHz.

Chapter 5 presents new DGS structures that form resonators when loaded on SIW technology. A novel back-to-back E-shaped defected ground structure (DGS) and two-side loading scheme for miniaturized dual-band substrate integrated waveguide (SIW) bandpass filter designs is proposed. The SIW loaded by novel DGS supports evanescent-mode wave propagation below the

cut-off frequency of SIW, while achieves two transmission poles at the passband and two controllable transmission zero points. Furthermore, the novel loading scheme by loading different-sized DGS resonators on two sides of SIW is proposed for dual-band bandpass filter designs. To validate the design and analysis, a 2.4-/5.2-GHz filter prototype was designed. In good agreement with theoretical results, the measured results of the dual-band filter achieve insertion losses of 3.6 and 3.1 dB, and fractional bandwidths of 5.8% and 6.45% at 2.4 and 5.2 GHz respectively. The filter size is only 1.036cm × 1.06cm. Meanwhile, in the design of a 60-GHz filter, a balanced DGS is used to create electrical coupling between non-adjacent resonators for additional attenuation poles.

Chapter 6 introduces a 2.4-/5.2-/60-GHz tri-band bandpass filter (BPF) design using two-layer PCB technology for the future WLAN and mobile applications. The SIR, SIW, DGS, and CPW techniques are mixed-used in the design approach. To accommodate such large frequency ratio with common input/output, a 2.4-/5.2-GHz dual-band BPF and a 60-GHz BPF are separately designed and connected in parallel with auxiliary low-pass filters (LPFs) and BPFs for signal isolation and matching between the RF and mm-wave frequencies. The fabricated tri-band filter is measured, with results in a good agreement with simulation and theoretical analysis. It features insertion losses of 1.7/3.0/2.0 dB with FBW of 0.12/0.10/0.18 at 2.4-/5.2-/60-GHz bands respectively. The filter size is 1170 mils × 1010 mils.

Chapter 7 draws the conclusion and gives the area that merits future research work.

CHAPTER 2

Literature Review

The DGS, SIW, and SIR techniques are investigated based theoretical calculations, EM simulations, and literature study. Their applications for filter performance enhancement, size miniaturization, and multi-band design are studied. Based on that, we design several advanced filters in Chapter 3-6.

2.1 Defected Ground Structure (DGS)

As the name implies, the defected ground structure (DGS) is the artificial defected shape etched on the ground plane to alter the wave propagation characteristics in traditional transmission lines and other types of waveguides. It was first proposed in [43] and later extensively studied in [44]. DGS is originated from photonic bandgap (PBG) structures that have periodic etched defects on the ground plane which exhibit stopband and slow-wave characteristic in the optical fields. By properly scaling the dimension of the structures, PBG can be applied to a wide frequency range. When scaled down and used in microwave and millimeter-wave circuits, PBG is referred as electro-magnetic bandgap (EBG). However, it is difficult to use PBG or EBG structures to design microwave and millimeter-wave circuits due to design parameters overhead, such as the number of lattice (unit), lattice shapes, lattice

spacing where each of them can affect the bandgap property, therefore, the modeling extraction becomes very challenging.

Compared to PBG or EBG structures, the advantages of DGS are discussed as follows:

1) A smaller area occupied because unlike PBG or EBG structures, there is no large number of periodic patterns required.

2) It is difficult to define the unit element for both PBG and EBG structures while doing the modeling extraction. To the contrary, it is easy to extract equivalent-circuit models for the unit DGS element because the main design parameter is the shape of the unit element.

3) In the designing of microwave and millimeter-wave circuits, the DGS structure can be modeled by simple resonant circuits and the parameter extraction is rather simple.

Recently, DGS has become one of the hottest research topics that has found enormous applications in the microwave circuit designs, such as filters, power dividers, couplers, amplifiers, and so on [44-54]. With its resonant property and slow-wave effect, DGS is a very popular choice for compact filter designs. In addition, cascading DGS cells is sometimes necessary for better stopband rejection and sharper roll-off.

2.1.1 The Dumbbell-Shaped DGS

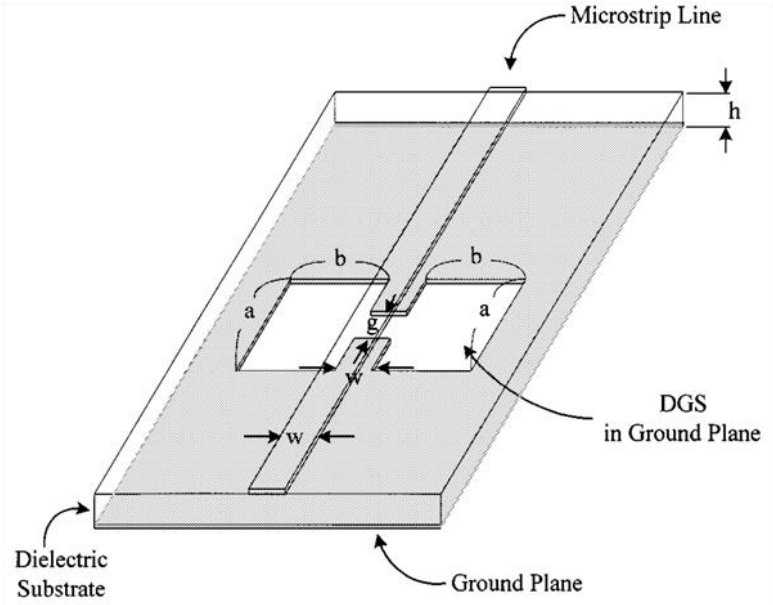

Figure 2.1 A 3-D view of the dumbbell-shaped DGS proposed in [43].

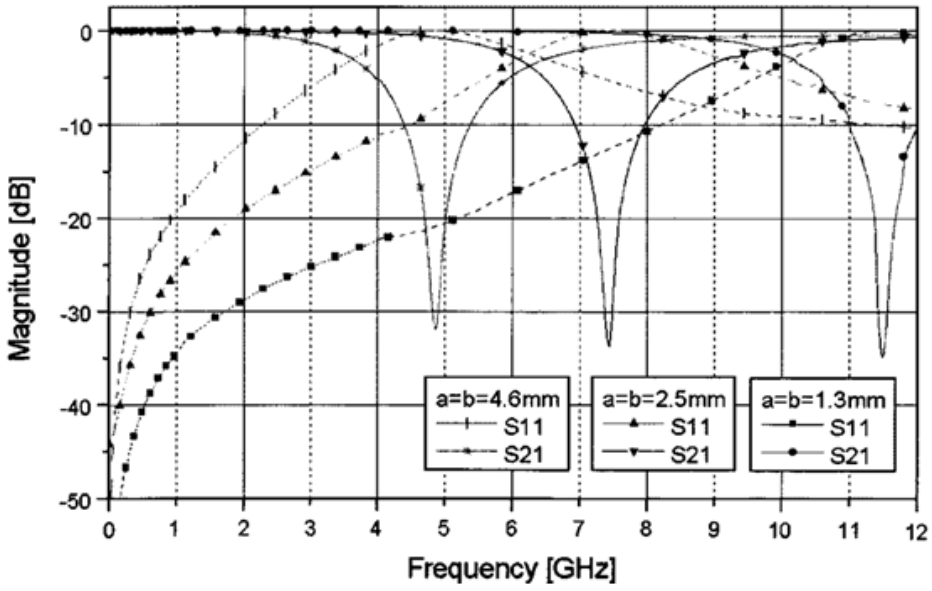

Figure 2.2 Simulation result of the dumbbell-shaped by changing the size of the square defects.

As in Figure 2.1, the dumbbell-shaped DGS [43] is the first-reported defected unit that provides a frequency response which is good enough to function as a bandstop resonator. For the dumbbell-shaped DGS, the slot under the transmission line causes an increase in the effective capacitance while the two rectangular defects on the two sides of the microstrip line cause an increase in the effective inductance seen by the transmission line.

The increase in the inductance and the capacitance introduce a cut-off response with attenuation pole in simulation result as shown in Figure 2.2. The cut-off frequency depends on the two square defects in ground plane; as the etched area of the unit structure is increased, the effective series inductance increases, thus gives rise to a lower cut-off frequency.

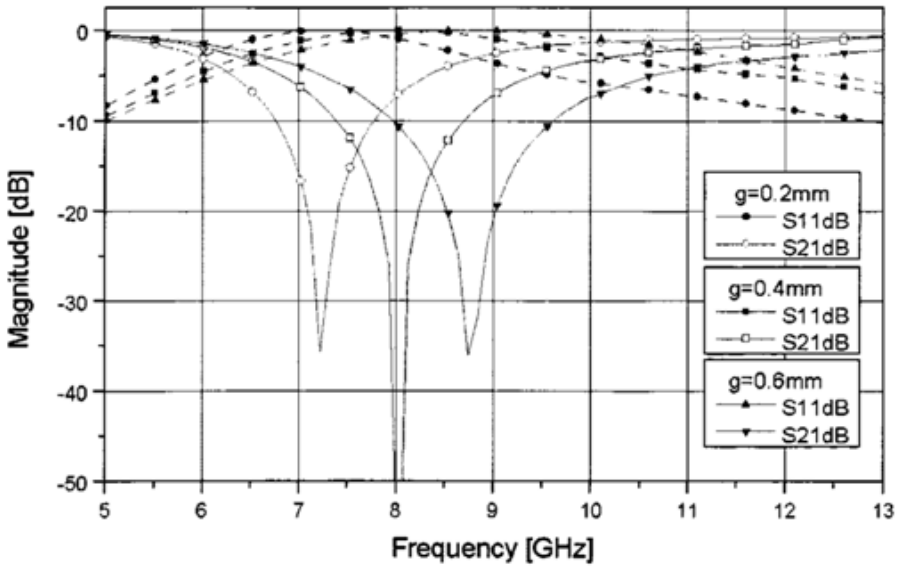

Figure 2.3 Simulation result of the dumbbell-shaped by changing the gap of the square defects.

However, an increase in the gap of the slot has no change in the cut-off frequency as in Figure 2.3, which means that the gap cannot affect the effective inductance. On the other hand, the attenuation pole location is dependent on the etched gap distance; as the etched gap distance increases, the effective capacitance decreases so that the attenuation pole location moves up to higher frequency.

In Figure 2.4(a), a parallel LC circuit is used as the equivalent circuit model and further investigate the characteristics of the DGS [44]. The equivalent circuit can be mapped into the *Butterworth-type* one-pole prototype low-pass filter circuit as in Figure 2.4(b).

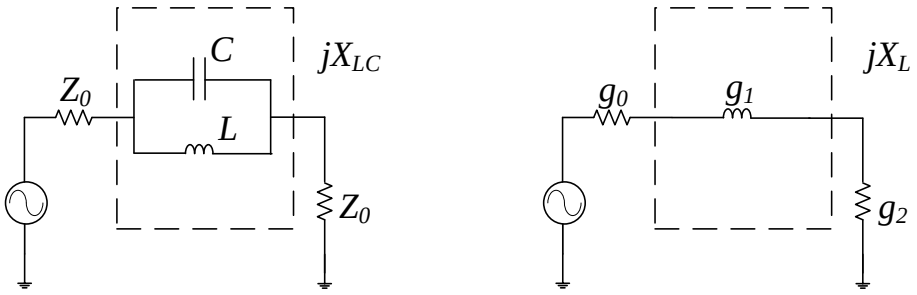

(a) (b)

Figure 2.4 (a) Equivalent circuit for dual-T DGS; (b) *Butterworth-type* one-pole prototype low-pass filter circuit

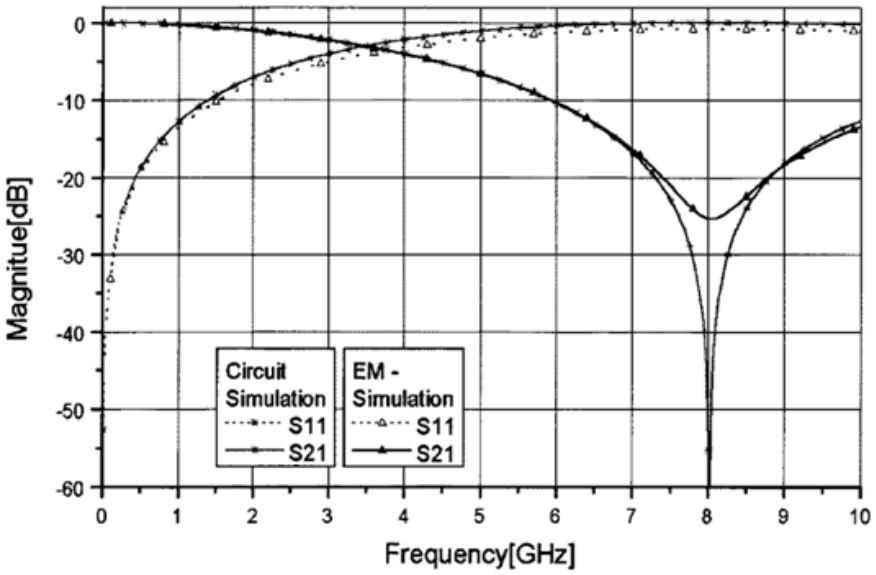

Figure 2.5 Simulation result and measurement result of dumbbell-shaped DGS.

The *L* and *C* values of the parallel LC circuit can be calculated as

$$X_{LC} = \frac{1}{\omega_0 C(\frac{\omega_0}{\omega} - \frac{\omega}{\omega_0})} \tag{2.1}$$

$$X_L = \omega' Z_0 g_1 \tag{2.2}$$

$$X_{LC}|_{\omega=\omega_{c,3dB}} = X_L|_{\omega'=1} \tag{2.3}$$

Where ω' (=1), g_1 (=2), and Z_0 (=50Ω) are the normalized 3-dB cut-off frequency, element value of one-pole *Butterworth* prototype LPF, and port impedance, respectively, and $\omega_0 = 1/\sqrt{LC}$ is the resonant frequency. The EM

simulation and the equivalent circuit simulation result are in a good agreement as in Figure 2.5.

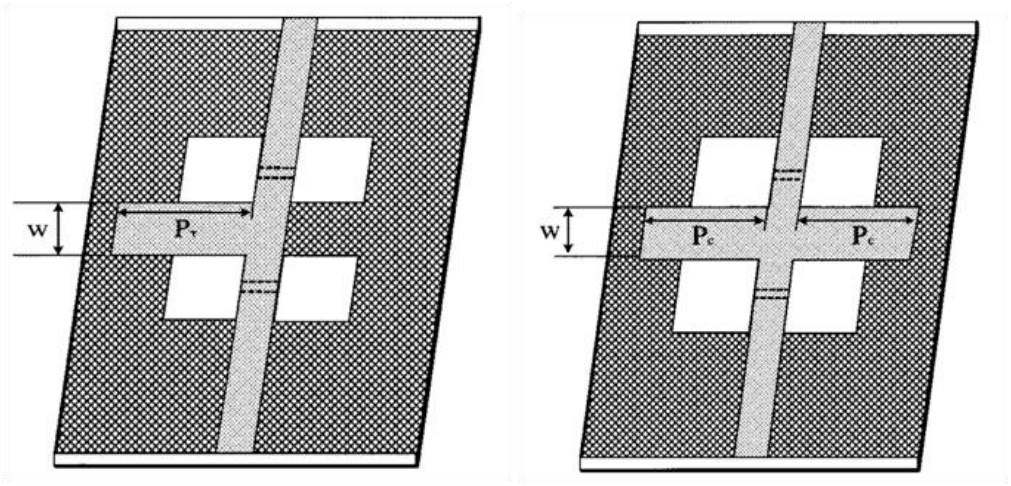

(a) (b)

Figure 2.6 The LPF designed in [44] using (a) T-junction structure, and (b) cross junction structure for the parallel open stub.

Based on the study of the dumbbell-shaped DGS, a three-pole LPF with attenuation at the cut-off frequency of 1.3 GHz with 0.01 dB ripple level was designed in [44] as shown in Figure 2.6. The parallel capacitance in the LPF is realized by using the parallel open stub with T-junction structure or cross junction structure as shown in Figure 2.6(a). The measurement result shows that the 3-pole LPF has an insertion loss of less than 0.15 dB, a return loss of more than 20 dB, and a rejection of 20 dB up to 8 GHz. One major drawback of this design is that the open stubs occupies too much area and has only a narrow-band performance. A five-pole *Chebyshev* LPF is designed in [55], which uses

different sizes of dumbbell-shaped DGS and a microstrip line in an abnormal width than the implementation in conventional LPFs. This design is free from open stubs, high impedance line, and tee- or cross-junction element. The increased line width of the LPF guarantees the capability of very high power handling. However, both of the LPFs are based on *Butterworth* or *Chebyshev* prototype, therefore, the passband to stopband transition is moderate.

Figure 2.7 shows the lumped LPF circuit with the equivalent circuit of the DGS unit structure.

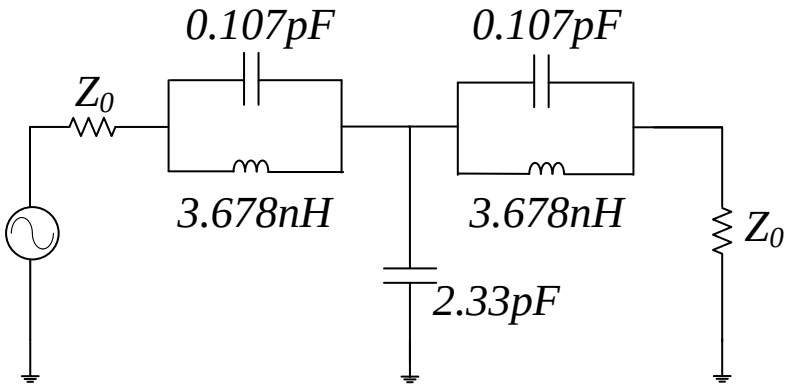

Figure 2.7 Equivalent circuit for the designed LPF.

2.1.2 Slot-shaped DGS

The rectangular defects in [43] can be replaced by circular-shaped defects or slot-shaped DGS. In [50], the response of four different head of the DGS

slots as in Figure 2.8(a) have been studied and compared. The equal area of the different heads only ensures equal equivalent inductance but not the identical response of each DGS unit although there all share the same equivalent circuit model as in Figure 2.8 (b). By changing the main parameters of each DGS shapes, a summary is drawn as follows:

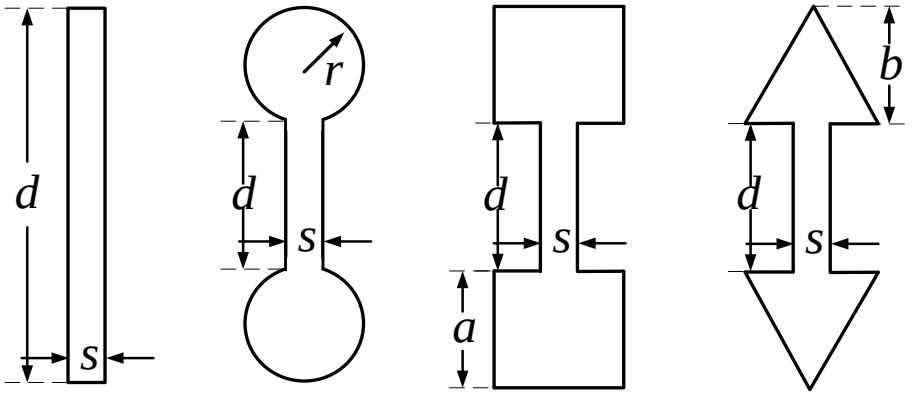

(a)

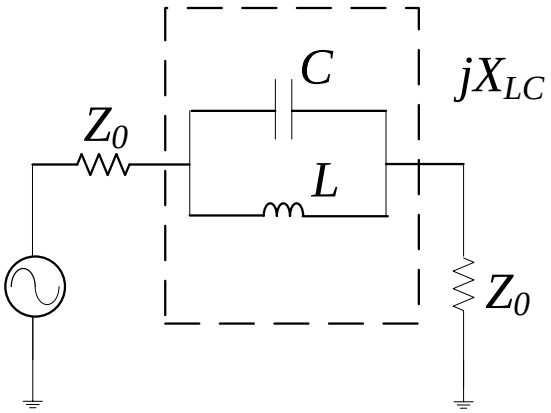

(b)

Figure 2.8 (a) Various slot-based DGS shapes; (b) Equivalent

Rectangular DGS: 1. The change in length (*d*) rather than in the slot width (*s*) is a more effective way to control f_c, f_0, and *L*; 2. For five times change in length or in width, both *C* and *L* changes at about the same magnitude. 3. The change in length has a little more influence on *L*, whereas the change in width has a little more influence on *C*.

Circular-head DGS: 1. The change in radius (*r*) has a stronger influence on *L* and the cut-off frequency f_c, as compared to its influence on *C* and f_0. Thus, the inductance can be changed without having much change in the attenuation pole frequency; 2. The slot-head separation (*d*) has an almost identical effect on *L* and *C*. It has a little more influence on *L* than *C*; 3. The increase in *d* brings f_c and f_0 closer, thereby improving sharpness of the transition.

Arrowhead DGS: 1. The side length (*b*) compared to radius (*r*) of circular-head DGS has less influence on f_c. Identical behaviour is obtained for f_0, *L*, and *C*; 2. The arrowhead separation (*d*) has more influence on *C* than the circular-head DGS; 3. The arrowhead slot provides better sharpness of cut-off with improved stopband response.

Square-head DGS: 1. Provide a maximum change in *L* for five times change in the side of a square arm; 2. A maximum change in *C* for five times change in the separation of the slot heads. However, to get large control of the inductance, we have to tolerate more variation in f_0 and f_c.

After comparison, it is concluded that with the same area of the head, the arrowhead-shaped DGS provides better sharpness of cut-off frequency response and with improved stopband response.

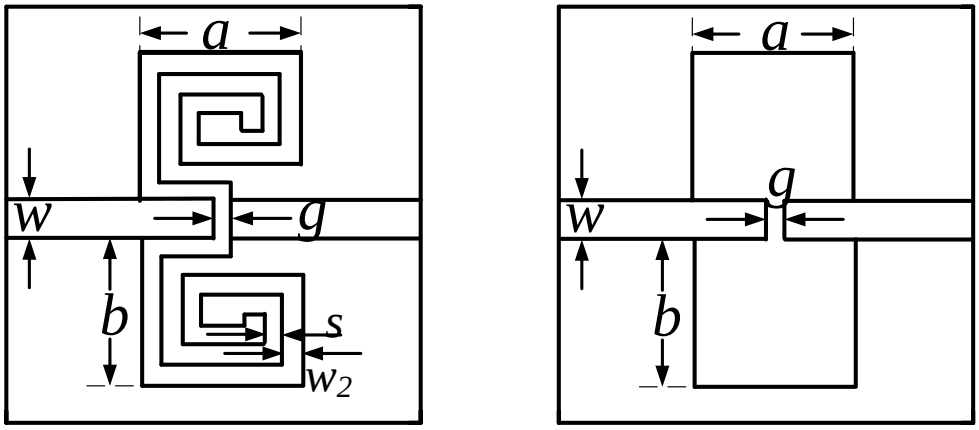

(a) (b)

Figure 2.9 (a) Spiral-shaped DGS. (b) Dumbbell-shaped DGS

2.1.3 Spiral-shaped DGS

Compared with the same dimensional dumbbell-shaped DGS, the spiral-shaped DGS as in Figure 2.9(a) [56] shows a large effective inductance and capacitance with the simulation result shown in Figure 2.10. Besides, the spiral-shaped DGS provides a narrow stopband with a much lower resonant frequency, therefore it has a great potential in the circuit size reduction. The model of the spiral-shaped DGS is shown in Figure 2.11 with a parallel inductor and a short stub to represent the periodical characteristic. The values of B_s and B_B can be calculated as follows:

$$B_s = -(Y_s cot\theta + \frac{1}{\omega L_s}) \tag{2.4}$$

$$B_B = \frac{-1}{\omega L_B} \tag{2.5}$$

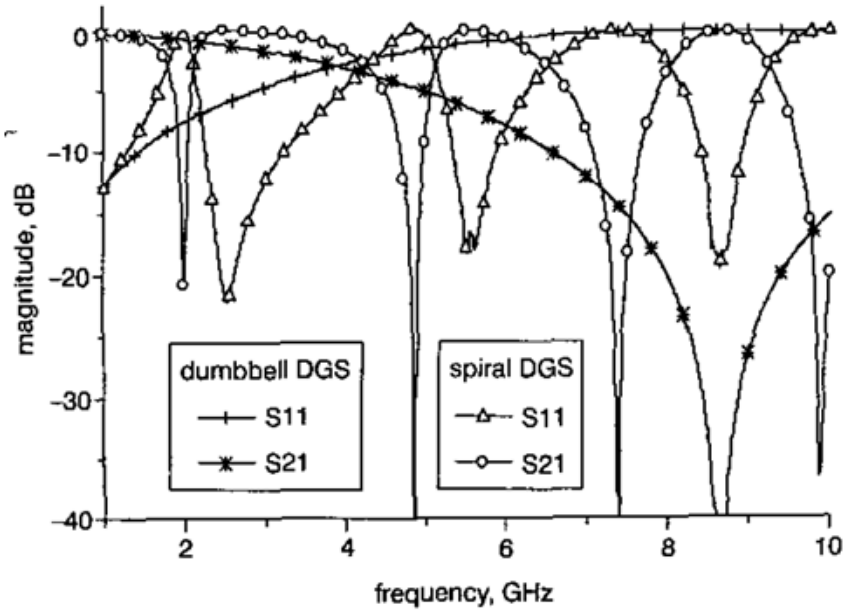

Figure 2.10 Simulated performance of the spiral and dumbbell DGSs.

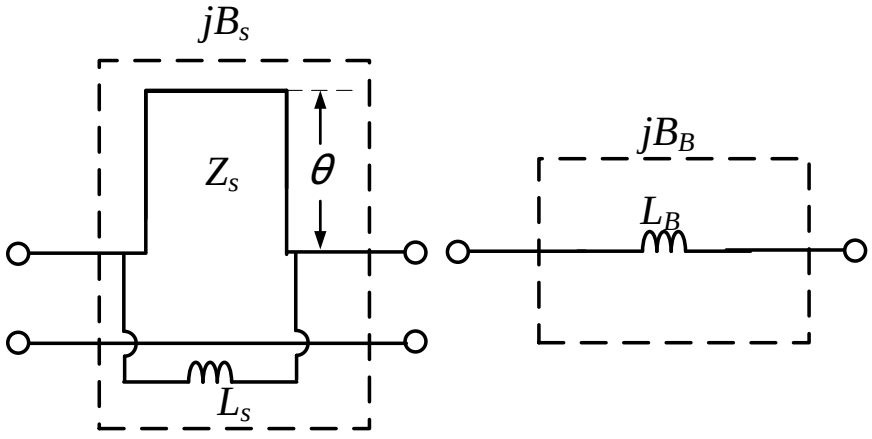

Figure 2.11 Equivalent circuit (a) spiral DGS (b) Butterworth-type one-pole LPF.

At frequencies where the first zero occurs and the first pole occurs, the values of susceptance and reactance of the equivalent circuit should be zero. Thus, the electrical length can be treated as 180 °. At f_c, the value of the two equivalent circuit should be the same. Based on the above analysis, we can substitute the values of the parameters in and get the values of Z_s and L_s.

In [57], the spiral-shaped DGS is applied to the standard CPW line to design a compact spiral-DGS CPW LPF. With the spiral-shaped DGS, the LPF shows a very compact size and a very sharp transition from passband to stopband even with only one or a few elements cascaded. Because of this excellent transition property, the spiral-shaped DGS is used in [54] to implement a multifunctional microstrip line with versatile circuit performance to filter out the signal which is close to the desired frequency band, thus to ensure the high port-isolation of the designed dual-band patch antenna. Besides this, a high performance five-pole elliptic functional LPF is designed in [58] by adopting both the spiral-shaped DGS and the dumbbell-shaped DGS, which benefit in sharp transition band and wide stopband respectively. The designed LPF is 23.9% smaller than the one in [55] and it completes the transition from 1 to 20 dB attenuation within only 0.45 GHz with an insertion loss of less than 0.3 dB and a 20 dB rejection stopband from 2.95 to 8.25 GHz.

2.1.4 U-slot and V-slot DGS

As shown in Figure 2.12, novel U-slot and V-slot DGS units were proposed in [59] and demonstrated to have higher Q-factor than those of dumbbell-

shaped and spiral-shaped DGS. Both of the U-slot DGS and the V-slot DGS can be modeled to the equivalent circuit as shown in Figure 2.12(c).

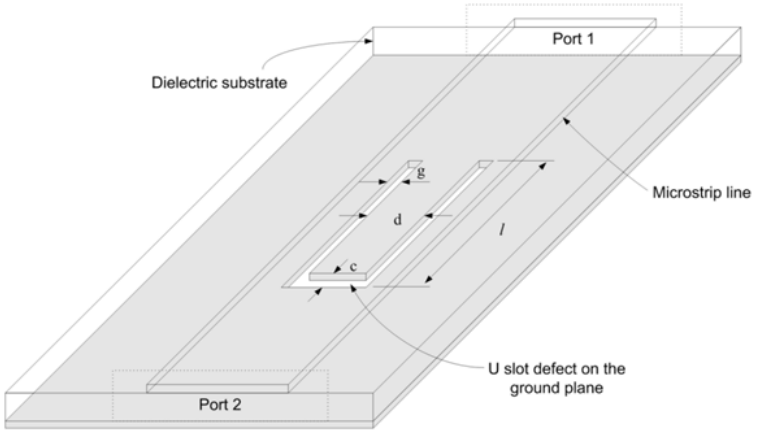

(a)

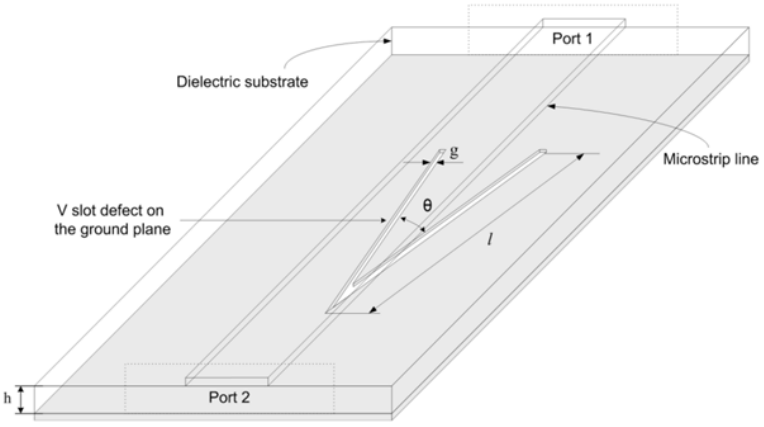

(b)

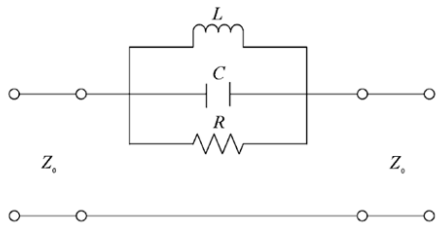

(c)

Figure 2.12 Structures for the (a) U sot DGS and (b) V-slot DGS. (c) Equivalent circuit for both U-slot and V-slot DGSs.

For the U-slot DGS, the increase in the slot length (*l*) would cause a decrease in the rejection bandwidth and resonant frequency which means an increase in the equivalent capacitance and equivalent inductance but has little effect on the *Q*-factor. The increase in the slot width (*g*) leads to a decrease in the equivalent capacitance but an increase in the inductance, thus there will be a decrease in the *Q*-factor. The key feature is the rapid increase in *Q*-factor with the decrease of the distance between two slots, which gives rise to rapid increase in the capacitance.

A high-*Q* bandstop filter with three cascaded U-slot DGSs is proposed and proved to have a high Q-factor of 26.7 and a suppression of 36 dB at the resonant frequency. In order to minimize the size of the designed filter, the V-slot DGS is proposed. The changes in resonant frequency and the *Q*-factor due to the slot width (*l*) and slot length (*g*) show similar behaviors as in the U-slot DGS. The key factor in increasing the *Q*-factor of the V-slot DGS is to decrease the interior angle which has no effect on the resonant frequency. The high *Q*-factor bandstop filter is designed by cascading three V-slot DGSs as the previous filter designed with U-slot DGSs. However, the V-slot filter can be designed by putting one V-slot into another V-slot to realize the circuit size minimization and it has a more than 20 dB rejection at frequencies from 3.5 to 4.3 GHz.

2.1.5 Cross-shaped DGS

For a high performance LPF, it should not only have high stopband rejection, low insertion loss, but also a wide stopband. In order to design a compact high performance LPF with the above performance, a cross-shaped DGS as in Figure 2.13 was proposed and analyzed in [52] which can be regarded as the superposition of the I- and H-shaped DGS cell as in Figure 2.13(a) and 2.13(b).

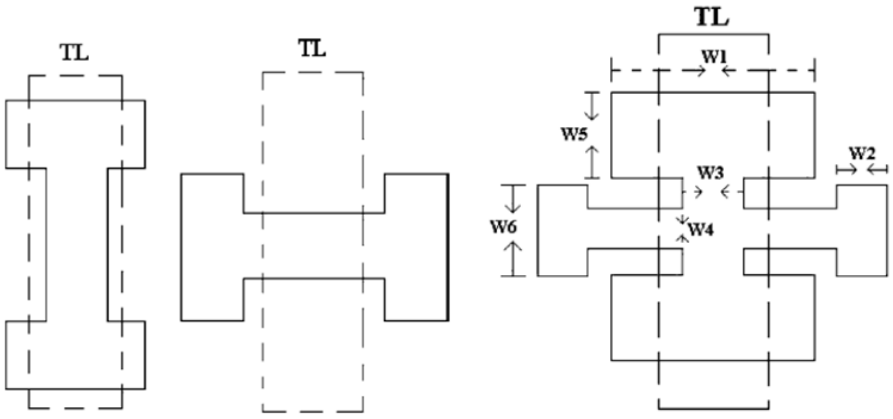

(a) (b) (c)

Figure 2.13 Structures for (a) I-shaped DGS, (b) H-shaped DGS, (c) cross-shaped DGS.

Figure 2.14(a) is the equivalent circuit of the proposed CS-DGS, in which the dash-line is the equivalent circuit of H-shape. The I-shaped part of CS-DGS is treated as aperture in the ground plane and analysed as hi-lo microstrip line which is modelled as a LPF prototype as in the equivalent circuit model. The

first spurious resonant frequency can be pushed away from the fundamental resonant frequency by tuning the size of the aperture to increase the ratio of the microstrip line with/without apertures, resulting in the widening of the upper rejection band.

The L_{p1} and L_{p2} are regarded as high impedance by apertures, C_{p1} and C_{p2} are ground capacitances without apertures in the ground plane. The simulated and the measured frequency responses of the proposed CS-DGS are shown in Figure 2.14(b). The CS-DGS with only one cell can achieve a 20 dB rejection from 4.25 to 15.9 GHz and a very sharp passband to stopband transition. However, the passband insertion loss is around 2.5 dB.

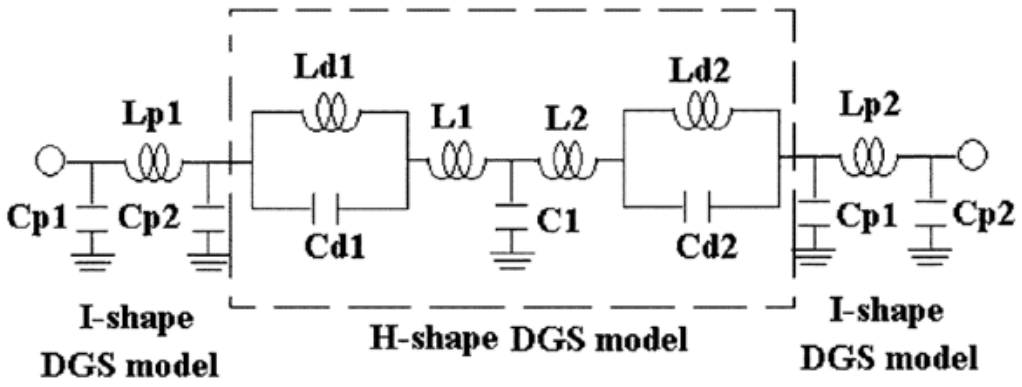

(a)

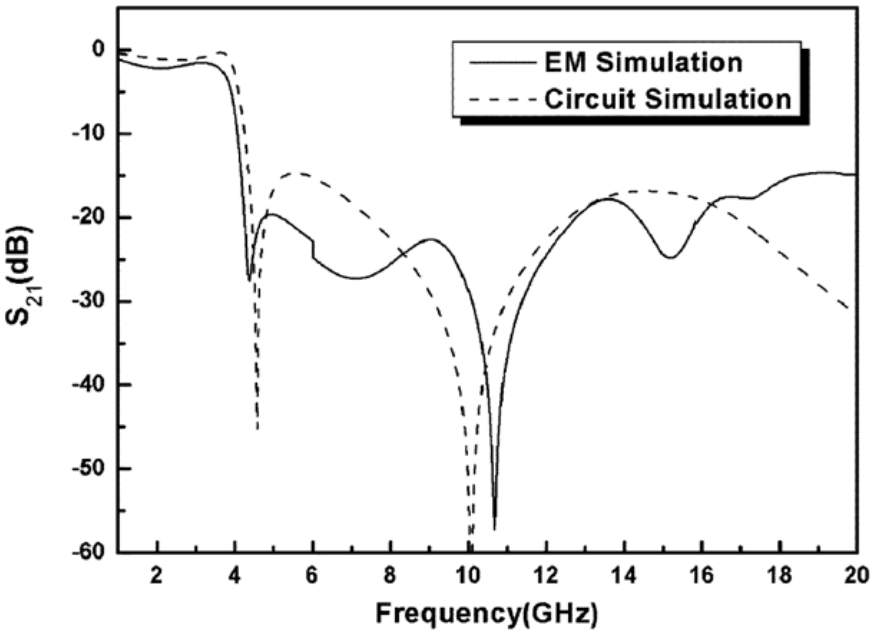

(b)

Figure 2.14 (a) Equivalent circuit for the cross-shaped DGS. (b) Simulation result for the cross-shaped DGS and its equivalent circuit.

2.2 Substrate Integrated Waveguide (SIW)

Substrate integrated waveguide (SIW) has attracted lots of research attentions after being proposed in [22]. In fact, a variety of applications have been recently proposed; namely wireless networks [60], automotive radars [61], imaging sensors [62] and biomedical devices [63].

Theoretically speaking, any lower frequency devices and circuits can be scaled up to their higher frequency counterparts. There is no exception for millimeter-wave techniques which could be constructed from existing and mature low-frequency design platforms. However, shorter wavelength at higher

frequency range may have exerted limitations in the fabrication procedures. In particular, the conventional low-cost planar structures such as microstrip lines and coplanar waveguide (CPW), which are popular candidates for designing filters and antennas, cannot be easily used for millimeter-wave (mm-Wave) and sub-millimeter wave (sub-mm Wave) applications. This is due to four drawbacks presented by conventional planar designs for mm-wave and sub-mm wave applications:

- Such semi-open planar structures generally exhibit high field/current singularities over open strip edges and high transmission loss because of conductor (surface roughness), dielectric, and radiation loss, thus low *Q*-factor.

- Power handling (more pronounce over mm-wave and sub-mm wave frequency ranges) and thermal management become a tedious issue because their transverse electromagnetic (TEM) mode operation requiring separated conductors.

- Design and implementation of planar structures are usually subject to packaging issue, crosstalk, direct current (DC) grounding, and mode conversion, leading to possible incompatible and excessive cost issues.

- Fabrication tolerance and impedance control are difficult to meet over mm-wave and sub-mm wave frequency range even by using advanced processing techniques.

Therefore, the components based on conventional planar technology (microstrip lines and CPWs) are no longer suitable for high performance, low cost and reliable system designs at mm-wave and sub-mm wave frequency range. On the other hand, the conventional nonplanar structures such as rectangular waveguide and coaxial lines have been widely explored for the development of mm-wave and sub-mm wave components even though they are expensive and bulky. The most attractive characteristics of nonplanar structures are their low-loss (high-*Q*), high power handling capability and completely shielded waveguide channel. Rectangular waveguides have much lower current densities, compared to conventional slot lines, CPS and CPW lines. Moreover, because the propagating fields are contained within an enclosed structure, there is no leakage of electromagnetic energy. As a result, this type of guided-wave structure enjoys the benefits of having a high *Q*-factor and excellent line-to-line isolation.

Thus, it is necessary to study SIW based on its configuration, operating principles, loss mechanisms, size, and bandwidth as a waveguide structure.

2.2.1 Configuration

Substrate integrated waveguide (SIWs), also known as laminated waveguide or post-wall waveguide, have been first mentioned back to 1994 [64]. Since that time, a vast range of SIW components, such as filters, antennas,

transitions, couplers, power dividers, and oscillators, have been proposed and studied [65-69].

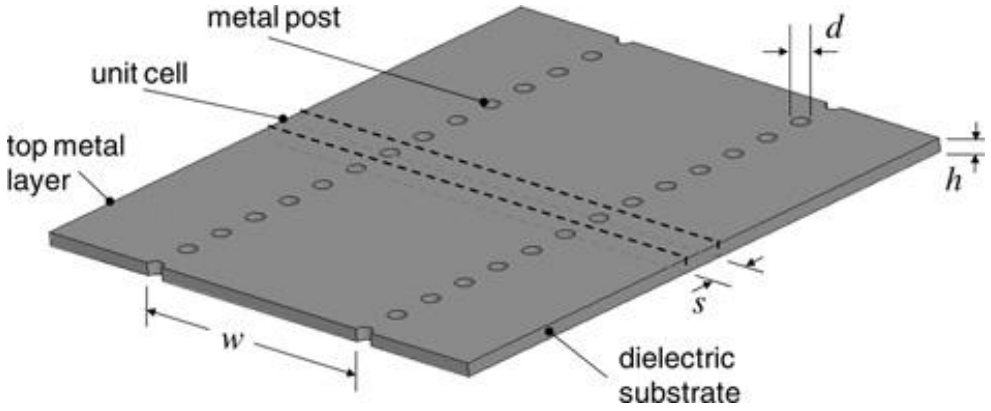

Figure 2.15 Configuration of a SIW

SIWs are integrated waveguide-like structures fabricated by using two rows of conducting cylinders or slots embedded in a dielectric substrate that electrically connect two parallel metal plates (Figure 2.15). In this way, the non-planar rectangular waveguide can be made in planar form, compatible with existing planar processing techniques (e.g. standard printed circuit board (PCB) or low-temperature co-fired ceramic (LTCC) technology). SIW structures exhibit propagation characteristics similar to the ones of classical rectangular waveguides, including the field pattern and the dispersion characteristics. Moreover, SIW structures preserve most of the advantages of conventional metallic waveguides, namely high *Q*-factor and high power handling capability with self-consistent electrical shielding. The most significant advantage of SIW

technology is the possibility to integrate all the components on the same substrate, including passive components, active elements and even antennas. Moreover, there is the possibility to mount one or more chip-sets on the same substrate. There is no need for transitions between elements fabricated with different technologies, thus reducing losses and parasitic. In this way, the concept of System-in-Package (SiP) can be extended to the system-on-substrate (SoS) [70]. SoS represents the ideal platform for developing cost-effective, easy-to-fabricate and high performance mm-wave systems.

First developed with the name of post-wall waveguide [65] or laminated waveguide [66], the SIW technology has been applied to several microwave components, including post and cavity filters [67, 71], directional couplers [72], oscillators [73, 74], power amplifiers [47, 75], slot array and leaky antennas [76, 77]. From the technical literature, it is seen that most of the classical waveguide components have been implemented in SIW technology. Nevertheless, most of these SIW components operate in the frequency range up to 30 GHz, with a few exceptions at higher frequency. This phenomenon is not due to physical limitations of SIW components, but to the increased technological difficulties encountered in designing and manufacturing SIW structures over the mm-wave range, namely, miniaturized dimensions, higher losses and the need to carefully select the material. Therefore current and future research activity aims to overcome these difficulties, in order to use SIW technology as an interconnection and integration platform for mm-wave systems.

2.2.2 Operating Principles

SIW structures exhibit propagation characteristics similar to those of rectangular metallic waveguides, provided that the metallic vias are closely spaced and radiation leakage can be neglected (Figure 2.16). More specifically, SIW modes practically coincide with a subset of the guided modes of the rectangular waveguide, namely with the TE modes.TM modes are not supported by SIW, due to the gaps between metal vias: in fact, transverse magnetic fields determine longitudinal surface currents, which are subjected to strong radiation due to the presence of the gaps [65]. In particular, the fundamental mode is similar to the TE_{10} mode of a rectangular waveguide, with vertical electric current density on the side walls.

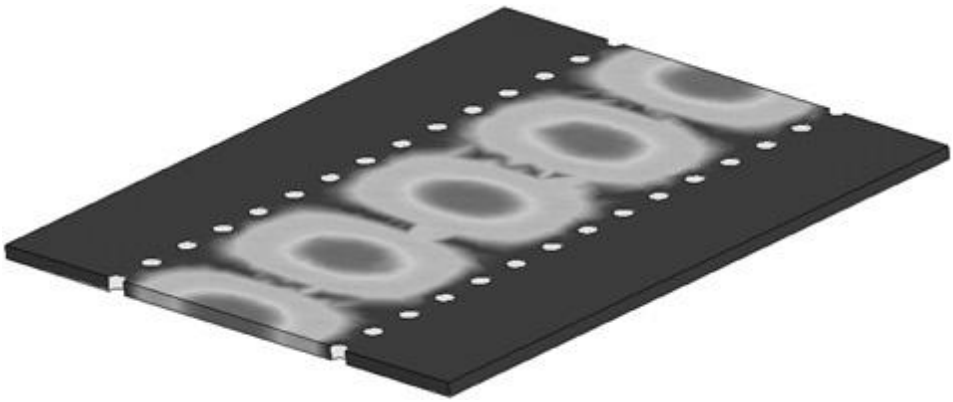

Figure 2.16 Plot of the amplitude of the electric modal vector of the fundamental SIW mode.

Owing to this similarity between SIW and rectangular waveguide, the cut-off frequency of the SIW can be calculated as:

$$f_c = \frac{c}{2w_{eff}\sqrt{\varepsilon_r}} \tag{2.6}$$

where c is the speed of light, ε_r is the dielectric constant of the SIW, and w_{eff} is the width of the rectangular waveguide. Empirical relations have been obtained between the geometrical dimensions of the SIW and the effective width w_{eff} of the rectangular waveguide with the same propagation characteristics. These relations allow for a preliminary dimensioning and design of SIW components, without any need of full-wave analysis tools. One of the most popular relations was derived in [78]

$$w_{eff} = w - \frac{d^2}{0.95s} \tag{2.7}$$

where d is the diameter of the metal vias, w represents their transverse spacing and s is their longitudinal spacing in Figure 2.15.

Relation (2.7) was subsequently refined in [14]

$$w_{eff} = w - 1.08\frac{d^2}{s} + 0.1\frac{d^2}{w} \tag{2.8}$$

A more rigorous determination of the propagation characteristics of SIW structures can be based on full-wave analysis tools, either commercial software (e.g. ANSYS high frequency structural simulator (HFSS) or CST Microwave Studio (MWS)) or in-house developed electromagnetic simulators: among them,

the most common techniques are based on the finite-difference time domain method or the finite-difference frequency domain [79], the boundary integral-resonant mode expansion (BI-RME) method [78], the method of lines [80] and the transverse resonant method [69]. In all cases, the determination of the propagation and attenuation constants of SIW structures is based on the analysis of the single unit cell (Figure 2.16), thus significantly reducing the computational effort.

2.2.3 Loss Mechanism

A key issue in the design of SIW structures is related to loss minimization, which is particularly critical when operating at mm-wave frequencies. Three major mechanisms of loss need to be considered in the design of SIW structures [81, 82]: they are conductor losses (due to the finite conductivity of metal walls), dielectric losses (due to the lossy dielectric material) and possibly radiation losses (due to the energy leakage through the gaps).

The behavior of conductor and dielectric losses is similar to the corresponding losses in rectangular waveguides filled with a dielectric medium, and the classical equations can be effectively applied. It transpires that conductor losses can be significantly reduced by increasing the substrate thickness, being the corresponding attenuation constant almost proportional to the inverse of substrate thickness h. The other geometrical dimensions of the SIW exhibit a negligible effect on conductor losses. Conversely, dielectric loss

depends only on the dielectric material and not on the geometry of the SIW structure, and therefore they can be reduced only by using a better dielectric substrate. Finally, radiation losses can be kept reasonably small if $s/d < 2.5$, with $s/d = 2$ being the recommended value. In fact, when the spacing s is small and the diameter d of the metal vias is large, the gap between the metal vias is small, thus approaching the condition of continuous metal wall and minimizing the radiation leakage. Generally speaking, the contribution of dielectric losses is predominant at mm-wave frequencies, when using typical substrate thickness and commercial dielectric material [82].

The insertion loss calculated for SIW structure, which accounts for conductor, dielectric and radiation losses, can be significantly increased by the effect of surface roughness in conductors. Analytical models of losses due to the surface roughness have been developed for classical waveguides, and are incorporated in commercial electromagnetic simulators. Recently, this issue has been carefully investigated through numerical and experimental studies in the case of microstrip transmission lines [83], whereas no publications have been reported yet in the case of SIW structures.

It is also particularly relevant to compare losses in SIW structures and in other traditional planar structures, for example, microstrip or coplanar lines. A systematic comparison of SIW and microstrip components is not easy, because SIW circuits are usually implemented on a thick substrate with low dielectric constant (which is not suitable for the implementation of microstrip circuits),

with the aim of minimizing conductor losses. In principle, microstrip component losses could also be mitigated by increasing the substrate thickness; in practice, however, this cannot be exploited due to the unacceptable increase in radiation loss and excitation of surface waves. A detailed comparison of losses in SIW structures, microstrip lines and coplanar waveguides is reported in [81]: it is seen that SIW structures can achieve comparable or lower losses, compared to traditional planar transmission lines.

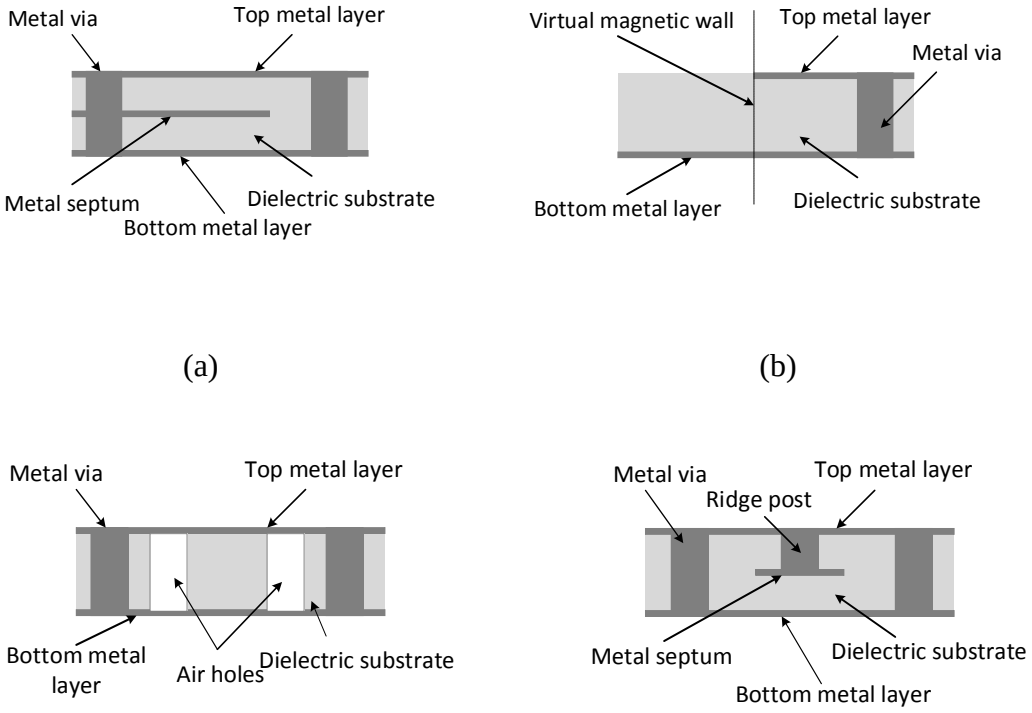

Figure 2.17 Different topologies of SIWs: (a) Substrate-integrated folded waveguide; (b) Half-mode SIW; (c) Substrate-integrated slab waveguide; (d) Ridge SIW.

2.2.4 Size and Bandwidth

Another important topic to be accounted for in the design of SIW structures is the performance in terms of size and operation bandwidth. In fact, similar to rectangular waveguides, SIW structures are limited in compactness and bandwidth. The width of the SIW determines the cut-off frequency of the fundamental mode (with a reduction of factor $\varepsilon_r^{-1/2}$ over hollow rectangular waveguides). The operation bandwidth is limited to one octave (from the cut-off frequency f_1 of the TE_{10} mode to cut-off frequency $f_2 = 2f_1$ of the TE_{20} mode), corresponding to the mono-mode bandwidth of the waveguide.

Different waveguide topologies have recently been proposed to improve the compactness of SIW structures (Figure 2.17).

The substrate-integrated folded waveguide (SIFW) was proposed in [84] (Figure 2.17(a)): a metal septum permits folding of the waveguide, thus reducing the size by a factor of more than two at the cost of slightly larger losses.

The half-mode substrate-integrated waveguide (HMSIW) was introduced in [85] (Figure 2.17(b)): based on the approximation of the vertical cut of the waveguide as a virtual magnetic wall, it permits a size reduction of nearly 50%. A combination of the two techniques was also proposed [86], resulting in the folded half-mode substrate-integrated waveguide (FHMSIW), which leads to a further size reduction.

To improve the bandwidth performance, some modified waveguide configurations have been developed. The substrate-integrated slab waveguide (SISW) was proposed in [87] (Figure 2.17(c)): it consists of an SIW where the dielectric medium is periodically perforated with air-filled holes at the lateral portion of the waveguide. This approach enables the design of a waveguide with a mono-modal band from 7.5 to 18 GHz (with 40% bandwidth enhancement). The implementation of a ridge waveguide in SIW technology was proposed in [88], where the ridge was implemented through a row of thin, partial-height metal posts located in the centre of the longer side of the waveguide. This structure allows coverage of the mono-modal band from 4.9 to 13.39 GHz, thus achieves a 73% bandwidth enhancement.

A significant improvement in the performance of the ridge SIW was introduced in [89] (Figure 2.17(d)): the modified ridge SIW is based on a row of partial height metal cylinders located in the broad side of an SIW and connected at their bottom with a metal strip. A modified ridge SIW covering the frequency band 6.8 to 25 GHz was designed and fabricated (with 168% bandwidth enhancement). A further improvement has been obtained with the ridge SISW, where air-filled holes were added. In this case, a ridge SISW covering the entire frequency band 7.1 to 30.7 GHz was designed and fabricated (with 232% bandwidth enhancement). This last configuration allows obtaining compact and broadband interconnects, which are 40% smaller than a

conventional SIW and exhibits three times broader bandwidth, and is suitable to fabrication by using standard PCB or LTCC technology.

2.3 Stepped Impedance Resonator (SIR)

Typical transmission-line type resonators with attractive features of simple structure, small size, and easy integrated with active circuits making it remain the most common choice for filters design in wireless communication. The applicable frequency range starts from 100MHz to around 100GHz [90].

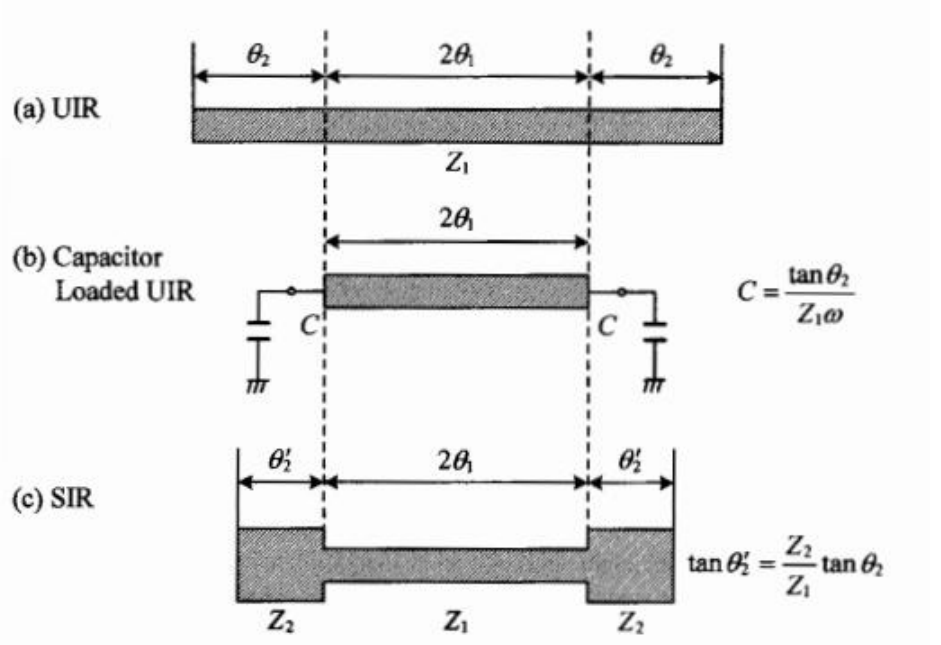

Figure 2.18 Structural variations of a half-wavelength type resonator. (a) Uniform impedance resonator (UIR); (b) Capacitor loaded UIR; (c) Stepped impedance resonator (SIR).

As shown in Figure 2.18(a), the micro-stripline half-wavelength resonator with two open-circuited ends is the typical transmission line type resonator and is most commonly used in the microwave region. This structure is expressed in electrical parameters as a transmission line possessing uniform characteristic impedance with an electrical length of 180 °, thus it is called uniform impedance resonator (UIR). With the advantages of simple structure and easy to design features, UIRs have been widely applied for conventional filters design with perfected design methods. However, in practical design, UIRs have the intrinsic disadvantages such as limited design parameters due to the simple structure, and spurious responses at nf_0 (f_0 is the fundamental resonance frequency and n >=2).

Loading capacitors at both open-ends of the resonator as shown in Figure 2.18(b) is a common way to overcome the problems. The value of the capacitance *C* can be calculated as follows:

$$C = Y_1 \tan\theta_2 / \omega_0 \tag{2.9}$$

where $Y_1 = 1/Z_1$, $\theta_2 = \pi/4-\theta_1$. The resonator length is shortened so that the spurious resonance frequencies are pushed to higher frequencies. However, this method is not suit for applications over 1 GHz, because the circuit-loss of the lumped-element capacitor *C* increases dramatically as does the variance of resonance frequency.

An open-circuited transmission line is used to replace the loaded capacitance *C* as in Figure 2.18(c) shows. The parameters of the transmission line should satisfy the following equations:

$$Y_1' \tan\theta_2' = Y_1 \tan\theta_2 \tag{2.10}$$

Under this condition, the three resonators in Figure 2.18 will resonant at same resonant frequency. From the equation, we can see, there is not necessary to design the characteristic impedance of the open-circuit transmission line as Z_1. A smaller resonator can be designed if the designed characteristic impedance (Z_1') is smaller than Z_1. This explains that the transmission line resonator can be realized by non-uniform characteristic impedance resonator which is stepped impedance resonator (SIR).

As the name stands, SIR represents the resonator of series connecting more than two transmission lines with different characteristic impedance. Figure 2.9 shows the basic examples of different types of SIRs, which are $\lambda_g/4$, $\lambda_g/2$, and λ_g type. For the $\lambda_g/2$ type resonator as in Figure 2.9(b) where open-ended structures are used, short-ended structures are also available.

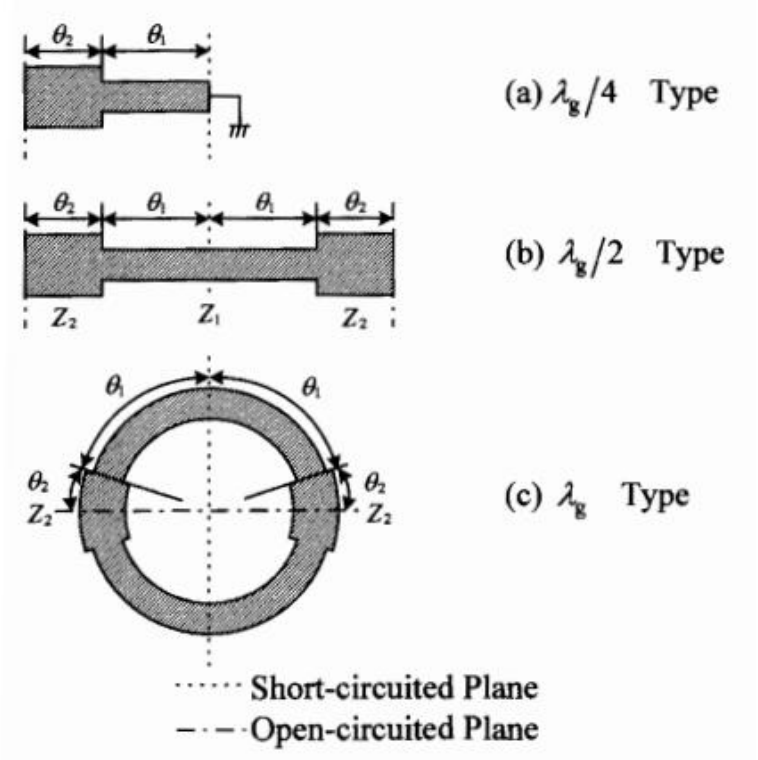

Figure 2.19 Basic structures of SIR. (a) Quarter-wave type; (b) Half-wavelength type; (c) One-wavelength type.

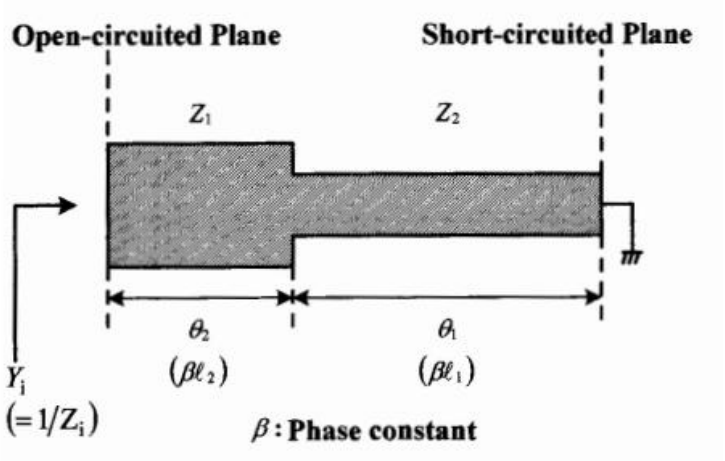

Figure 2.20 Electrical parameters of elementary SIR.

Figure 2.20 shows the fundamental element of $\lambda_g/4$-type resonator. It is configured by connecting two transmission lines with different characteristic impedance in series, while one end of the transmission line kept open and one end of the transmission line shorted to ground.

The resonance condition of the above $\lambda_g/4$-type resonator can be calculated as follows:

$$Z_i = jZ_2 \frac{Z_1 \tan\theta_1 + Z_2 \tan\theta_2}{Z_1 \tan\theta_1 - Z_2 \tan\theta_2} \tag{2.11}$$

The resonance condition happens when $Y_i = 0$, thus

$$Z_2 - Z_1 \tan\theta_1 \tan\theta_2 = 0 \tag{2.12}$$

which is

$$\tan\theta_1 \tan\theta_2 = Z_2 / Z_1 = R_z \tag{2.13}$$

where R_z is the impedance ratio of Z_2/Z_1. Therefore, the resonance condition of SIR is determined by θ_1, θ_2 and impedance ratio R_z, which gives SIR more freedom compared to UIR.

From the above discussion, we can see SIR has the merits of a wide degree freedom, a wide range of applicable frequency. It is a promising resonator structure capable of overcoming the essential drawbacks of the conventional

transmission-line resonator, which is commonly applied to filters in the RF/microwave region.

The resonance conditions of all three types of SIR as in Figure 2.19 can be expressed using the same equation as in formula (2.13). In addition, the overall resonator length attains a minimum values when R_z <1 and $\theta_1 = \theta_2$.

CHAPTER 3

DGS Assisted Low-Pass Filter Design

Low Pass Filters (LPF) play an important role in microwave and millimeter wave circuits to suppress harmonics and spurious. The characteristics of high attenuation, wide stopband, low passband insertion loss and compact size [33] are important for LPF applications. Recently, numerous research works have been published for designing high performance LPFs using defected ground structure (DGS) [33, 43, 51, 52, 54, 56-59, 91, 92]. In general, there are two effects of DGS; the bandgap effect, which can prevent the wave propagation at center frequency range [44], and the slow-wave effect, which contributes to the size reduction of microwave circuits, make DGS an attractive solution to realize high performance LPFs with reduced size. In [53], periodical tapered circles satisfying brag reflection conditions were etched on the ground plane to realize LPF with stopband up to $4.8f_c$ (f_c is the cut-off frequency) and rejection better than 20dB. However, periodical structures resulted in large size. In [51], an elliptic-function LPF with low loss and sharp roll-off was achieved by using spiral and dumbbell DGS structures. But the skirt selectivity is not good and the stopband bandwidth covers only to $3.03f_c$. Recently, a transformed radial stub (TRS) LPF [34, 39] was introduced for planar high performance

lumped-element-free LPF design. It is proven that good skirt selectivity, deep stopband rejection and wide stopband can be achieved by using TRS cells.

In this chapter, a novel DGS is proposed and implemented to further improve the performance of TRS LPF with low insertion loss and wide stopband. The top and bottom views of proposed DGS assisted TRS LPF are shown in Figure 3.1. The novel dual-T DGS cells and circular-shape DGS are defected under the input and output transmission lines and the coupled lines respectively to generate additional transmission zeros. By changing the dimensions of TRS cell and DGSs, the locations of the transmission zeros can be controlled. The 3D Electromagnetic simulator ANSYS HFSS is used in the following design and investigation based on the Rogers RT/Duriod 5880 substrate with a relative permittivity of 2.2 and substrate thickness of 10 mils are used.

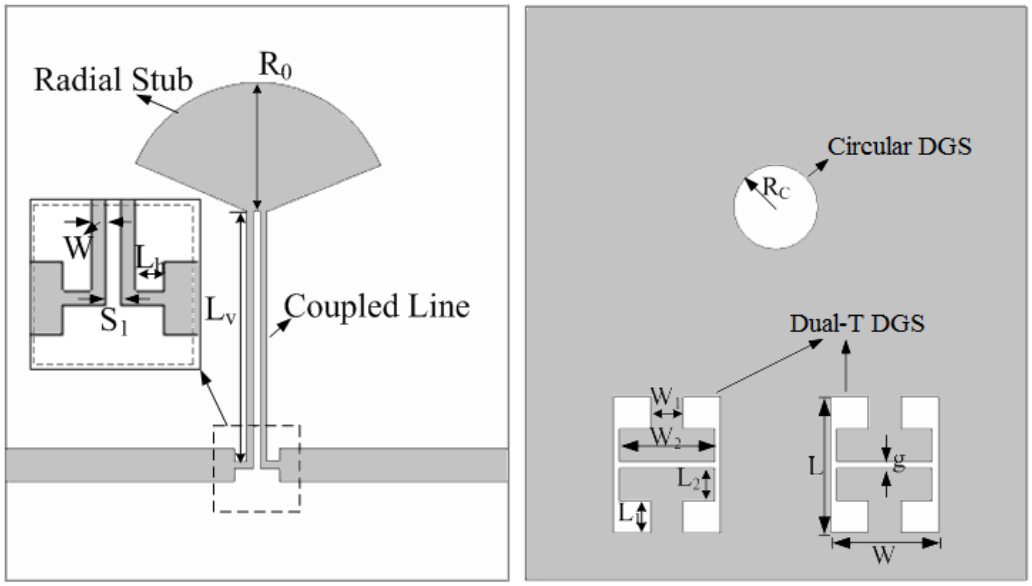

Figure 3.1 Schematic of the designed DGS assisted TRS LPF cell from (a) top view; (b) bottom view.

3.1 Dual-T DGS Cell Investigation

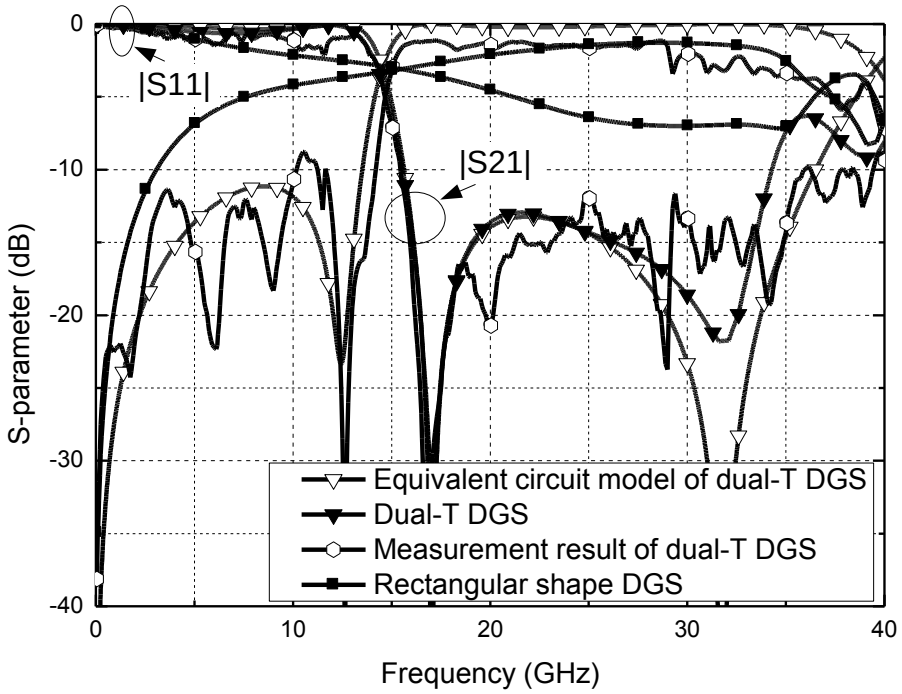

Figure 3.2 Simulation result of the rectangular DGS, dual-T DGS and the equivalent circuit model for dual-T DGS. Measurement result for the dual-T DGS. The parameter values for dual-T DGS are: L=126mil, L_1=30mil, L_2=30mil, g=6mil, S_2=6mil, W_1=6mil and W_2=76mil. The electric values for the equivalent circuit are: Lr=Ls=0.38nH, Cr=0.23pF, Cs=0.21pF, Lm=0.32nH, Lc=0.05nH, Cc=0.08pF.

Conventional DGSs like dumbbell shape [44] and circular shape [53] can only generate one transmission zero in their bandgap frequency range. It is not enough to control a wide stopband range. A dual-T shape DGS is proposed as shown in Figure 3.1(b). As a contrast to the proposed dual-T DGS, a

rectangular shape slot with the same width W = 88 mils and length L = 126 mils as dual-T DGS cell is analyzed and simulated as a reference. Both the dual-T DGS and rectangular DGS are defected on the ground of same microstrip transmission lines. For the rectangular DGS, it is a large aperture on the ground plane which reduces capacitance from the top trace to the bottom ground while increases effective inductance. Therefore, stopband rejection is expected. It is verified in EM simulation as shown in Figure 3.2, however, the stopband rejection is less than 6dB up to 35 GHz.

Compared to rectangular DGS, the dual-T DGS occupied the same area demonstrates better stopband rejection by introducing two transmission zeros. It attributes to the two back to back quarter-wavelength stepped impedance resonator (SIR) structures formed by the dual-T DGS, which is symmetrical about the horizontal transmission line (TL) in Figure 3.1. For each part of the dual-T DGS cell, two step sections with widths W_1 and W_2 with characteristic impedances Z_1 and Z_2 respectively are connected in series, and thus form SIR structure. In addition, the high impedance section is grounded while the low impedance section is open. The resonant condition for conventional SIR is as in [93]:

$$\tan(\theta_1) \cdot \tan(\theta_2) = R_z \tag{3.1}$$

where R_Z represents the impedance ratio Z_2/Z_1, θ_1 and θ_2 denote the electrical length of two impedance sections. In this design, the lengths of two stepped

impedance are equal, thus θ_1 and θ_2 are nearly the same. However, the overlap of signal line and low impedance stub in the dual-T DGS results in a large loading capacitance (C_L), which increases the effective electrical length of low impedance section. Therefore, the resonant condition is revised as:

$$\tan(\theta_1 + \Delta\theta) \cdot \tan(\theta_1) = R_z \tag{3.2}$$

where $\Delta\theta$ represents electrical length variation caused by C_L. The value of C_L is calculated as the plate capacitance between signal line and low impedance stub:

$$C_L = \frac{\varepsilon A}{d} = \frac{\varepsilon_r \varepsilon_0 A}{d} = \frac{\varepsilon_r \varepsilon_0 W_2 (W_T - g)/2}{d} \tag{3.3}$$

where ε_r is the relative permittivity, ε_0 is the vacuum permittivity, A is the overlap area, W_T is the width of the 50-Ω transmission line which is 30 mils, and d is the substrate thickness. By equating C_L to the impedance of open stub, the variation of electrical length can be calculated as below:

$$1/\ j\omega C_L = Z_{oc} = -jZ_2 \cot(\Delta\theta) \tag{3.4}$$

$$\Delta\theta = \tan^{-1}(\omega C_L Z_2) \tag{3.5}$$

In this design, Z_1, Z_2, and R_Z are calculated as 211.92 Ω, 63.96 Ω and 0.302 respectively with physical parameters as in the caption of Figure 3.2. After substituting all the parameter values to equation (3.2), (3.3), (3.5), the

fundamental and second resonant frequencies are deduced as 16.24 GHz and 86.78 GHz.

In Figure 3.2, EM simulation shows that the fundamental resonant frequency of dual-T DGS is 17.1 GHz, which is quite aligned with theoretical prediction. The small difference is caused by omitting other parasitic capacitances like fringing capacitances. The second resonant frequency at 32.1 GHz, which is far from the first spurious frequency 86.78 GHz, should be slot resonant mode of the DGS structure.

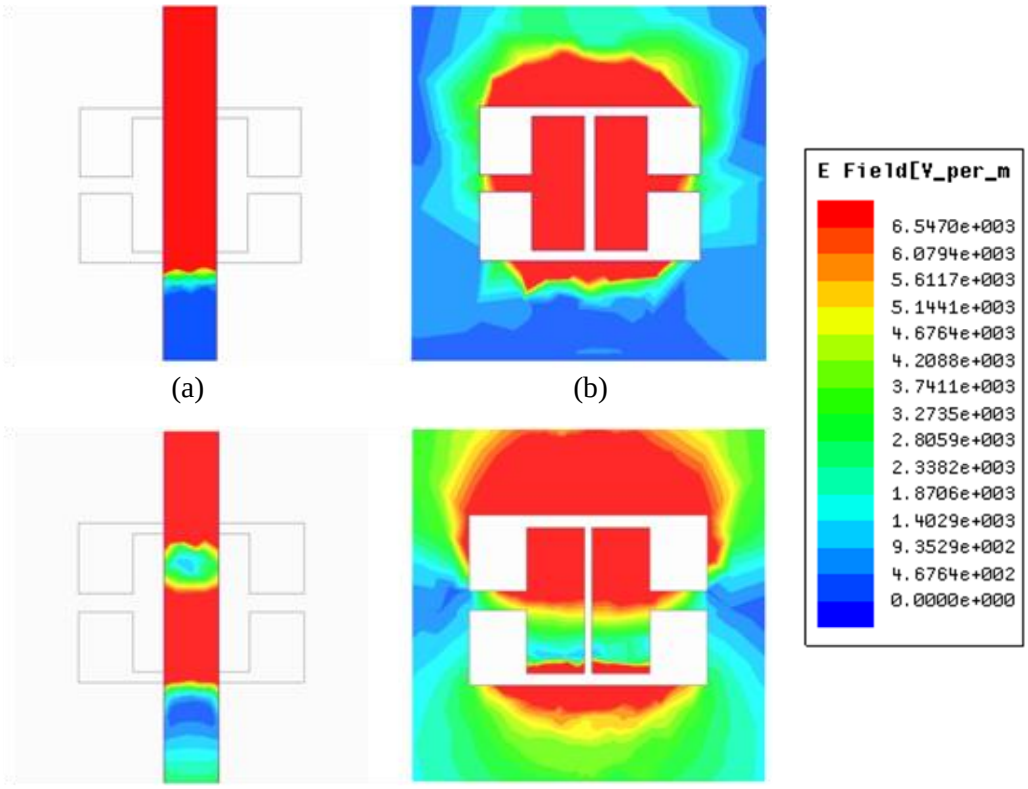

(a) (b)

(c) (d)

Figure 3.3 The electric field distribution of DGS at 17.1 GHz: (a) the transmission line and (b) the ground plane; the electric field distribution at 32.1 GHz: (c) the transmission line and (d) the ground plane.

The electric field distributions at two resonant frequencies on the ground plane and the microstrip line is plotted in Figure 3.3. It clearly shows that the electric field on transmission line is coupled to ground and different field distribution patterns appear at the two resonant frequencies: the one in Figure 3.3(a) and 3.3(b) correspond to the SIR formed by the dual-T DGS and the second one in Figure 3.3(c) and 3.3(d) correspond to the slot resonator with electric field concentrating along the slot.

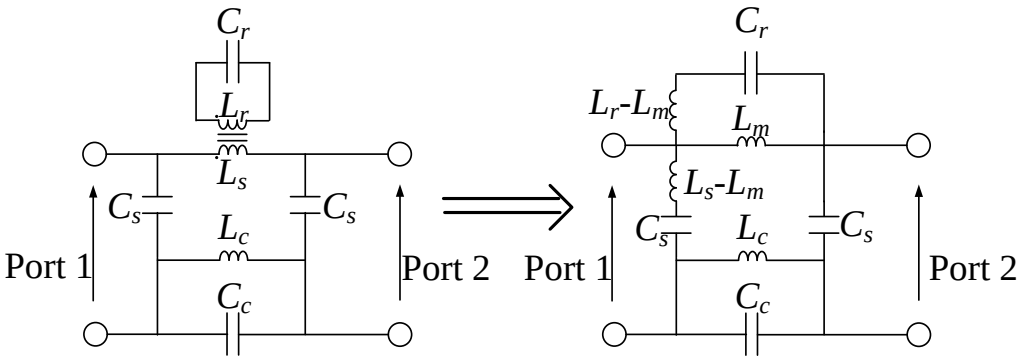

Figure 3.4 Equivalent circuit for the dual-T DGS under microstrip transmission line.

Based on the above analysis, the equivalent circuit for the dual-T DGS under the microstrip line is developed and shown in Figure 3.4. For the dual-T DGS, SIR is modeled as a parallel resonator formed by C_r and L_r with inductive

coupling coupled to the inductive microstrip line. The slot resonator is formed by a parallel C_c and L_C circuit which is connected to the microstrip to ground capacitor (C_S) and then connected to the inductive microstrip line. The simulation results of the equivalent circuit and the dual-T DGS under microstrip line are compared in Figure 3.2. The above two results are agreed well with each other.

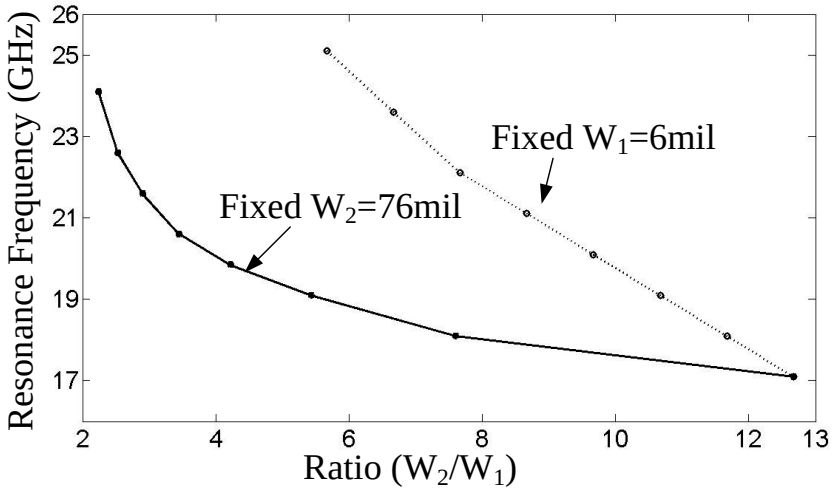

Figure 3.5 The relationship between the resonant frequency and the ratio of W_2/W_1 by varying W_2 from 76mil to 34mil with step of 6mil while keeping W_1 as 6mil and by varying W_1 from 6mil to 34mil with step of 4mil while keeping W_2 as 76mil.

The value of impedance ratio R_Z can be controlled by changing the values of W_1 and W_2 if other parameters are fixed. In this way, the electrical length to fulfill the resonant condition in (3.1) can also be controlled. Therefore, the resonant frequency where locates the transmission zero can be adjusted. This effect is studied by gradually changing W_1 with W_2 fixed and vice versa. Both

cases are shown in Figure 3.5. It is noted that the resonant frequency is more sensitive to W_2 than W_1 for lower resonant frequencies from 16 to 22 GHz. Thus, the values of W_1 and W_2 can be tuned to achieve better LPF performance when implementing dual-T DGS to TRS cell while maintaining the size unchanged. The measurement result of dual-T DGS is shown in Figure 3.2 and it is well aligned with the simulation result. It exhibits better than 10 dB return loss and a wide stopband spanning from 16.5 to 35 GHz with a better than 12 dB rejection.

3.2 DGS Embedded TRS LPF Designs

The TRS cell in Figure 3.1 can generate three transmission zeros: the lowest frequency one contributes to the sharp roll-off and the other two zeros help to achieve wide stopband. In this design, the dimensions of TRS cell are set to fit the design frequency: L_v = 231.07 mils, R_0 = 112.2 mils, W = 6mils, S_1 = 6.12 mils and L_h = 11.59 mils. With this dimension, the TRS cell shows a passband return loss better than 20 dB, a stopband from 3.1 to 18 GHz with three transmission zeros located at 5.4 GHz, 8 GHz and 16.5 GHz as in Figure 3.6. The DGS cells introduced in Figure 3.1 can be used to further extend the stopband.

Two dual-T DGS are defected under the ground plane of the TRS as shown in Figure 3.1. By changing the ratio of W_2/W_1 of dual-T DGS, the

stopband performance of proposed LPF varies as predicted since the transmission zero created by the dual-T DGS varies. With W_1 and W_2 of the dual-T DGS cell set to be 30 mils and 88 mils respectively, the simulation results of the single LPF cell are shown in Figure 3.6 with satisfied wide stopband from around 17 GHz up to 35 GHz.

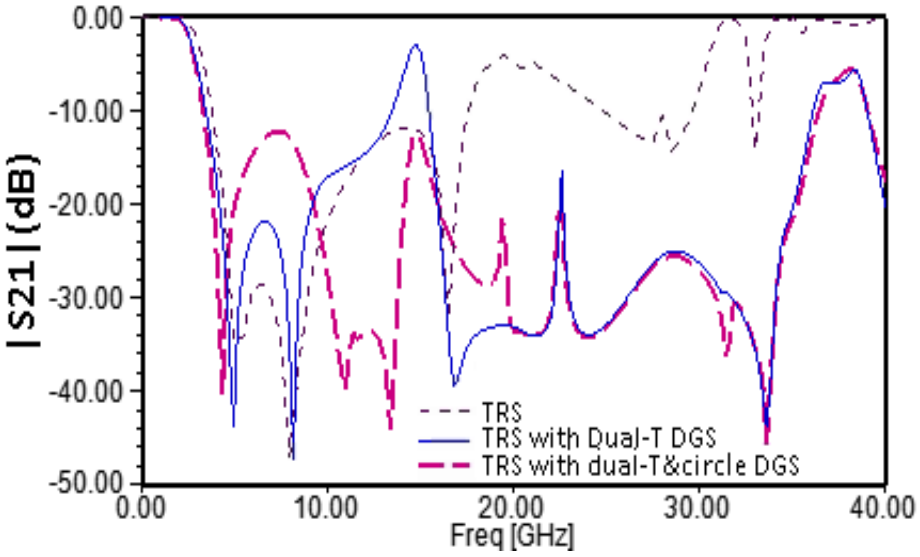

Figure 3.6 Simulation results of the TRS unit cell, TRS with dual-T DGS unit cell and TRS with both dual-T & circle shape DGS.

However, there is a transmission pole at around 17 GHz which deteriorate the performance of the stopband. In order to achieve wider stopband characteristic, a circular-shape DGS in Figure 3.1(b) is introduced under the radial stub to change the effective inductance and capacitance of the radial stub. The radius for the circle of 39.25 mils is chosen after investigation. The simulation results in Figure 3.6 show that the proposed LPF cell has a band-stop

rejection of more than 12 dB from 3.5 to 35 GHz. It can be seen that circular-shape DGS has the capability to remove parasitic passband located at 17 GHz.

Figure 3.7 (a) Top view and bottom views of one-cell TRS LPF; (b) Top and bottom views of two-cell TRS LPF.

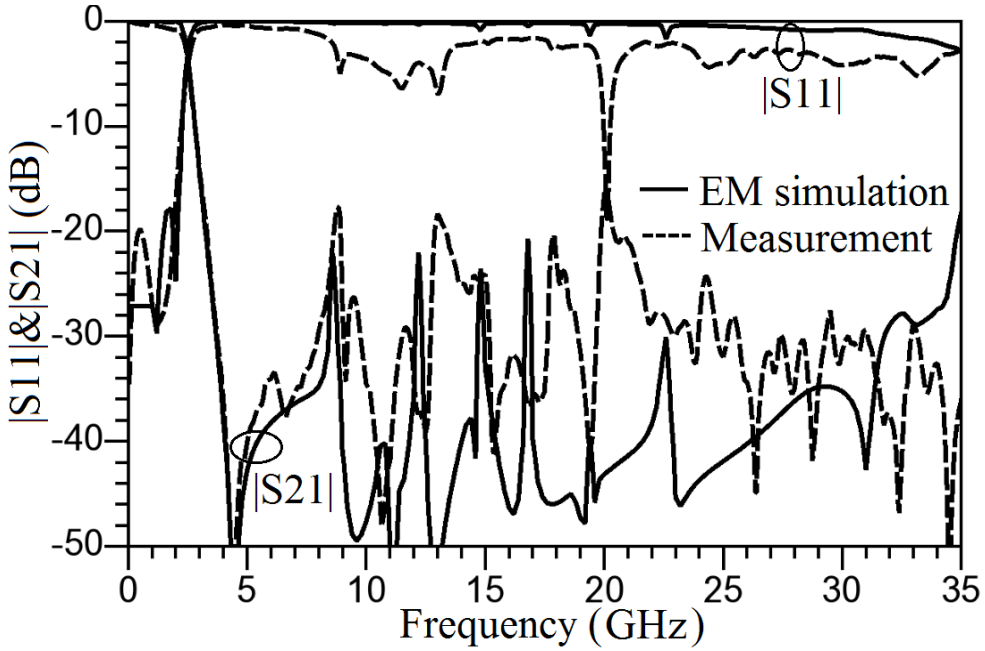

Figure 3.8 Simulation and measurement results of the two-cell DGS embedded TRS LPF.

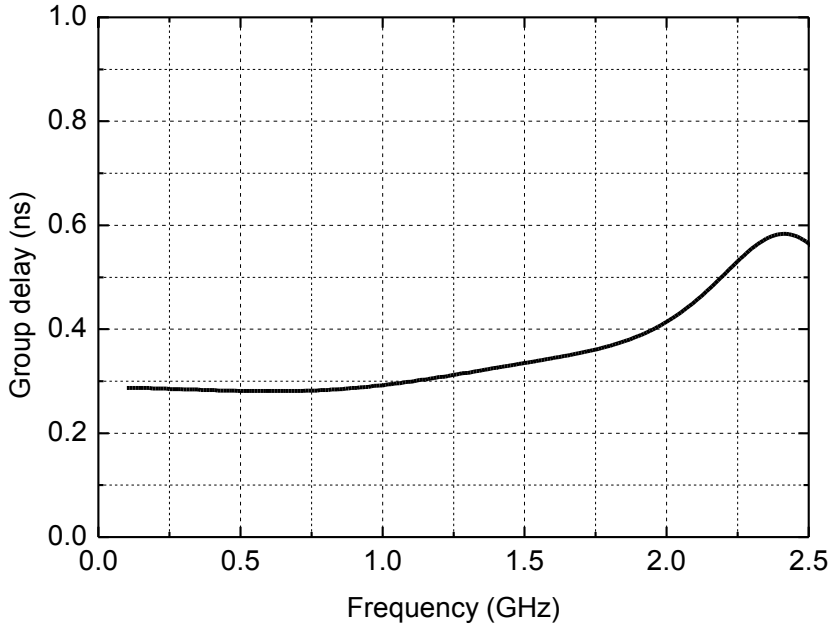

Figure 3.9 Simulation result of the group delay of the designed LPF

To achieve higher stopband rejection and sharper roll-off, two-cell DGS assisted TRS LPF is designed by cascading two LPF cells as shown in Figure 3.7. Via-holes are inserted between the cells to minimize the mutual coupling between two LPF cells.

The simulation and measurement results are quite aligned as shown in Figure 3.8. The measured result shows that the two-cell LPF can achieve stopband up to 35 GHz with better than 16 dB rejection and the passband return loss of better than 18 dB.

Figure 3.9 shows the simulation result of the group delay of the designed LPF. The one-cell and two-cell LPFs have the size of 0.14 $\lambda_g \times 0.167\ \lambda_g$ and 0.26$\lambda_g \times 0.167\ \lambda_g$ respectively (λ_g is the guided wavelength).

3.3 Summary

A novel LPF implemented by using the proposed DGSs together with TRS cell is demonstrated in this chapter. The proposed dual-T DGS is investigated and verified by experiment. The TRS LPF with proposed dual-T DGS can achieve stopband up to 35 GHz with better than 16 dB rejection and the passband return loss of better than 18 dB in a compact size of 0.26 $\lambda_g \times 0.167\ \lambda_g$.

CHAPTER 4

New DGS Co-Designed Resonator and Its Application for Bandpass Filter Designs

In literature, a multiband bandpass filter (BPF) is intuitively implemented with separate filtering paths [1, 23, 40, 41]. In [23], two different-sized complementary split-ring resonators (CSRR) were parallel loaded on surface of the substrate integrated waveguide (SIW) to obtain a dual-band frequency response. Later in [1], defected ground structure (DGS) resonators were loaded on both sides of SIW for dual-band filter miniaturization. In [41], a dual-band filter was designed utilizing multilayer ceramic technology by combining two separate BPFs with matching networks. However, these filters take advantages of waveguide structures and multilayer technology. Indeed if transmission line (TL) based implementations is adopted, this parallel filtering paths topology leads to area overhead [4, 42].

In general, TL-based multiband filters utilize multimode resonators [3, 4, 6, 9, 31, 32]. In [31], a generalized single-band to multiband frequency mapping technique was developed. Several multiband filters were synthesized by loading the hairpin and the meandered resonators to the conventional single-band parallel-coupled half-wavelength resonator filters. In [3], a series of multiple

stubs loaded ring resonators were reported for dual-, tri-, and quint-band BPF designs. In the past, due to its design flexibility, stepped impedance resonator (SIR) is widely deployed for multiband filter applications [4, 6, 9, 32]. In [32], several dual-band filters were realized with magnetic coupling between the adjacent SIRs. In [6] and [9], the coupled three-section SIRs were theoretically investigated and experimentally verified for dual-band BPF designs.

In this Chapter, we present a new dual-band BPF solution for the future WLAN and mobile applications, with three passbands at 2.4- and 5.2-GHz bands. The 2.4-/5.2-GHz filter utilizes a new asynchronous tuned mixed coupled resonator, which is formed by overlapping a quarter-wave SIR on the top plane of PCB and a quarter-wave coplanar waveguide SIR (CPW-SIR) etched by DGS on the ground plane of PCB. The synthesis method is investigated, which is validated in the first-order and fourth-order dual-band filter design.

The design and analysis in the Chapter are based two-layer PCB technology using the substrate Rogers 5880 (ε_r = 2.2, h = 10 mils, tan δ = 0.0009). The full-wave electromagnetic simulation is performed with *ANSYS HFSS* v.15.

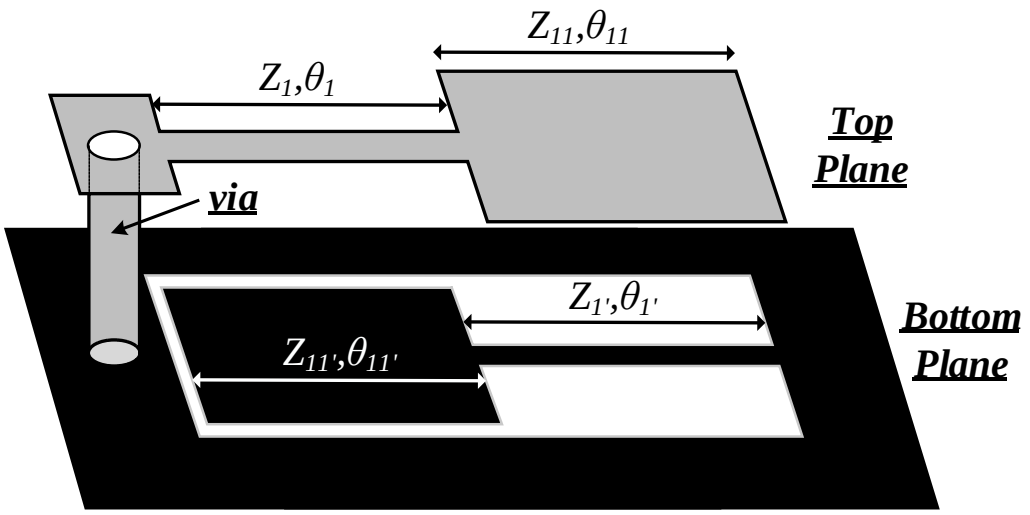

Figure 4.1 Three-dimensional view of the proposed mixed coupled SIR/CPW-SIR resonator.

4.1 Resonator Configuration

Figure 4.1 shows the three-dimensional view of the proposed resonator. On the top plane of two-layer PCB, a quarter-wave SIR structure is formed with two sections of transmission lines with characteristic impedance and equivalent electrical length of (Z_1, θ_1) and (Z_{11}, θ_{11}). The resonator is short to ground through a metallic via at the end of high impedance section. On the bottom plane, a quarter-wave CPW-SIR structure is formed by etching defects on the metal surface, with high impedance section ($Z_{1'}$, $\theta_{1'}$) and low impedance section ($Z_{11'}$, $\theta_{11'}$).

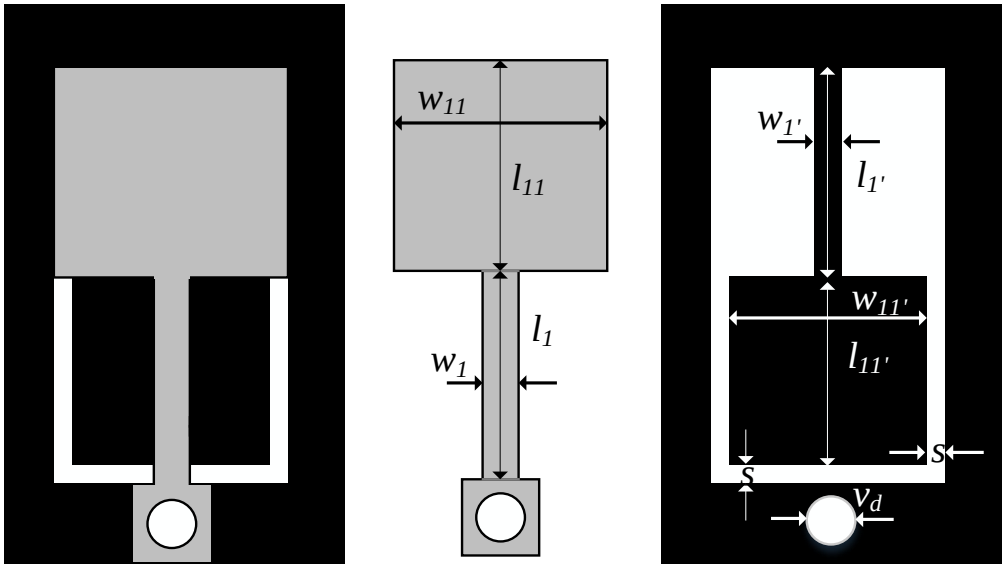

Figure 4.2 Top view and dimensions of the resonator in Figure 4.1.

4.2 Resonator Characteristics

According to resonance properties of SIR [94], the top and bottom resonators have their intrinsic resonance conditions fulfilled at:

$$Z_{11} / Z_1 = \tan\theta_1 \tan\theta_{11} \tag{4.1}$$

$$Z_{11'} / Z_{1'} = \tan\theta_{1'} \tan\theta_{11'} \tag{4.2}$$

The resonant frequencies are controllable and tunable by varying the corresponding physical parameters in Figure 4.2. The mutual coupling mechanism between SIRs was well studied and experimentally verified in [32].

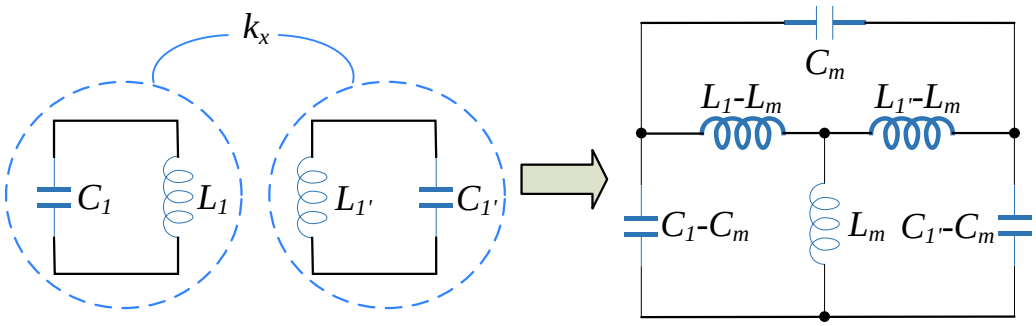

Figure 4.3 Asynchronous tuned mixed coupled circuit model of the proposed resonator.

Based on [90], SIR/CPW-SIR can be modeled as parallel *LC* circuit at the fundamental resonant frequency. As the SIR and CPW-SIR are directly overlapped through a substrate with thickness of 10 mils only, their mutual coupling ($k_x = k_e - k_m$) is formed by both magnetic (k_m) and electric coupling (k_e) mechanism [3] [95], i.e. the mixed coupling mechanism. Thus, the proposed resonator is modeled as an asynchronously tuned coupled-resonator circuit as shown in the modified circuit in Figure 4.3 [96]. An impedance inverter $K = \omega L_m$ and an admittance inverter $J = \omega C_m$ are used to denote the magnetic coupling (k_m) and the electric coupling (k_e) respectively, defined as

$$k_m = \frac{L_m}{\sqrt{L_1 L_{1'}}},\ k_e = \frac{C_m}{\sqrt{C_1 C_{1'}}}. \tag{4.3}$$

Using nodal analysis, the Eigen-equation of the circuit is derived as

$$\omega^4(L_1C_1L_{1'}C_{1'} - L_m^2C_1C_{1'} - L_1L_{1'}C_m^2 + L_m^2C_m^2) \\ -\omega^2(L_1C_1 - L_{1'}C_{1'} - 2L_mC_m) + 1 = 0 \tag{4.4}$$

The two positive solutions to this biquadratic equation can be calculated as

$$\omega_1 = \sqrt{\frac{\Re_B - \Re_C}{\Re_A}}\ ,\ \omega_2 = \sqrt{\frac{\Re_B + \Re_C}{\Re_A}}\ . \tag{4.5}$$

with

$$\Re_A = 2(L_1C_1L_{1'}C_{1'} - L_m^2C_1C_{1'} - L_1L_{1'}C_m^2 + L_m^2C_m^2)$$

$$\Re_B = (L_1C_1 + L_{1'}C_{1'} - 2L_mC_m) \tag{4.6}$$

$$\Re_C = \sqrt{\Re_B^2 - 2\Re_A}$$

Its mixed coupling coefficient k_x can be extracted as

$$k_x = \pm\frac{1}{2}\left(\frac{\omega_{02}}{\omega_{01}} + \frac{\omega_{01}}{\omega_{02}}\right)\sqrt{\left(\frac{\omega_2^2 - \omega_1^2}{\omega_2^2 + \omega_1^2}\right)^2 - \left(\frac{\omega_{02}^2 - \omega_{01}^2}{\omega_{02}^2 + \omega_{01}^2}\right)^2} \tag{4.7}$$

with ω_{01} and ω_{02} denoting the fundamental resonant frequencies of the SIR and CPW-SIR

$$\omega_{01} = \frac{1}{\sqrt{L_1C_1}}\ ,\ \omega_{02} = \frac{1}{\sqrt{L_{1'}C_{1'}}}\ . \tag{4.8}$$

To validate the analysis, in Figure 4.4, the resonator is studied using Eigen-mode simulation by varying the resonator length. To simplify the analysis, the lengths of four impedance sections have equal value $l_1 = l_{11} = l_{1'} = l_{11'}$. Two resonant frequencies f_1 and f_2 are observed as predicted by (4.5). Similar to other types of resonators, the resonant frequencies get lower with increased resonator size.

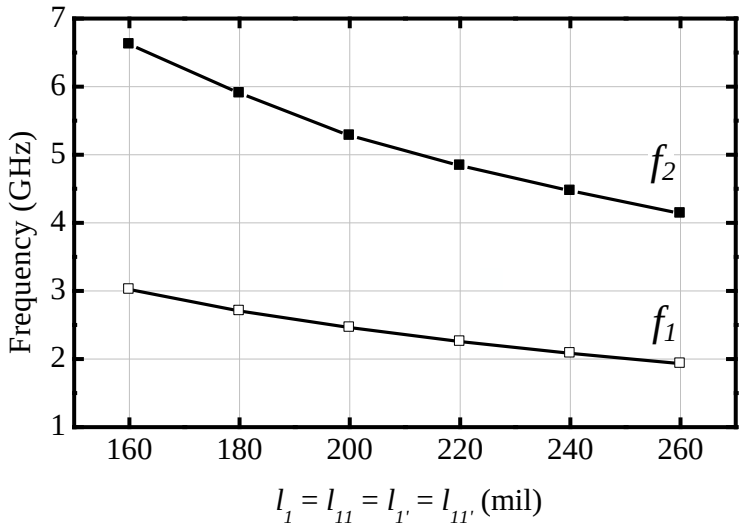

Figure 4.4 Resonant frequencies investigation using Eigen-mode simulation. (w_1 = 12, w_{11} = 88, $w_{1'}$ = 12, $w_{11'}$ = 65, s = 12, v_d = 50, unit: mil)

Figure 4.5 shows more Eigen-mode simulation results by changing the width of each impedance section of the resonator. It is noticed that the resonant frequency is more sensitivity to parameter w_1, w_{11}, $w_{1'}$ compared to parameter $w_{11'}$. It is due to the fact that the characteristic impedance of the low impedance section in CPW-SIR ($Z_{11'}$) is less sensitive to the change of $w_{11'}$ since $w_{11'} \gg 2s$

[97]. As both resonant frequencies are tuneable and controllable, the proposed resonator can be bridled for dual-band filter designs for 2.4- and 5.2-GHz bands.

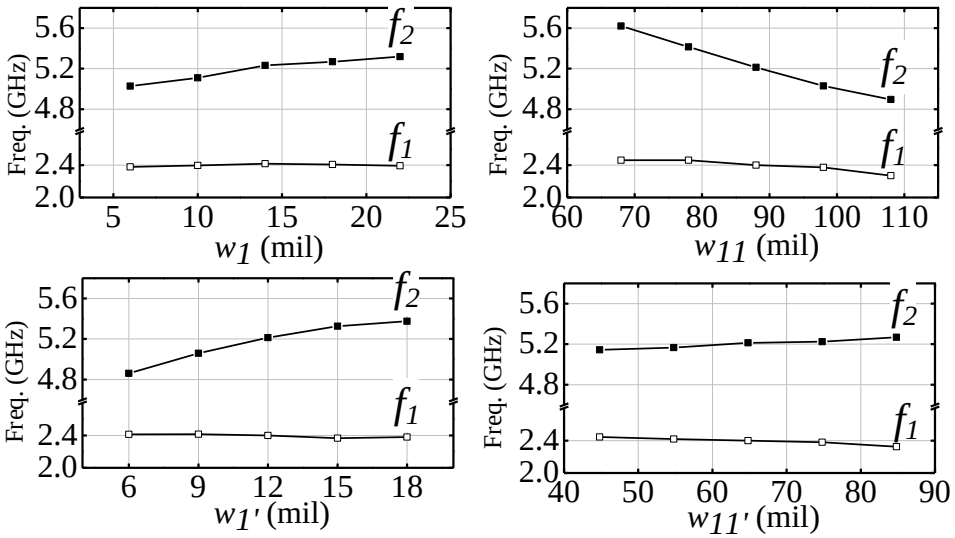

Figure 4.5 Parametric resonant frequencies investigation using Eigen-mode simulation. (w_1 = 12, l_1 = 200, w_{11} = 88, l_{11} = 200, $w_{1'}$ = 12, $l_{1'}$ = 200, $w_{11'}$ = 65, $l_{11'}$ = 200, s = 12, v_d = 50, unit: mil)

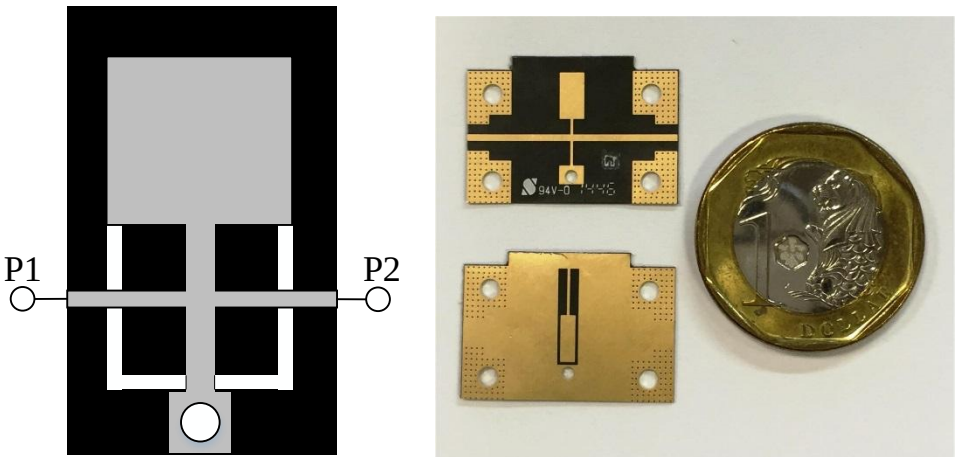

(a) (b)

Figure 4.6 The first-order dual-band BPF: (a) configuration (w_1 = 12, l_1 = 200, w_{11} = 108, l_{11} = 200, $w_{1'}$ = 12, $l_{1'}$ = 200, $w_{11'}$ = 65, $l_{11'}$ = 200, s = 12, v_d = 50, t = 120, unit: mil); (b) photograph of the fabricated filter.

4.3 First-order Dual-band BPF

As in Figure 4.6, the first-order filter is designed for 2.4-/5.2-GHz frequencies based on previous analysis and optimization using EM tools. The tapped-lines are attached at the high-impedance section of SIR as input/output. The scattering parameters are measured after short, open, load, thru (SOLT) calibration. Figure 4.7 shows the filter performance with two passbands at 2.4 GHz and 5.2 GHz range. Well agreed with EM simulation, the measured results has an insertion loss of 0.4 dB at 2.4 GHz with a 3-dB fractional bandwidth (FBW) of 0.38 at 2.4-GHz band, and an insertion loss of 0.8 dB at 5.3 GHz with a 3-dB FBW of 0.19 at 5.2-GHz band. The return losses are better than 10 dB at both passbands.

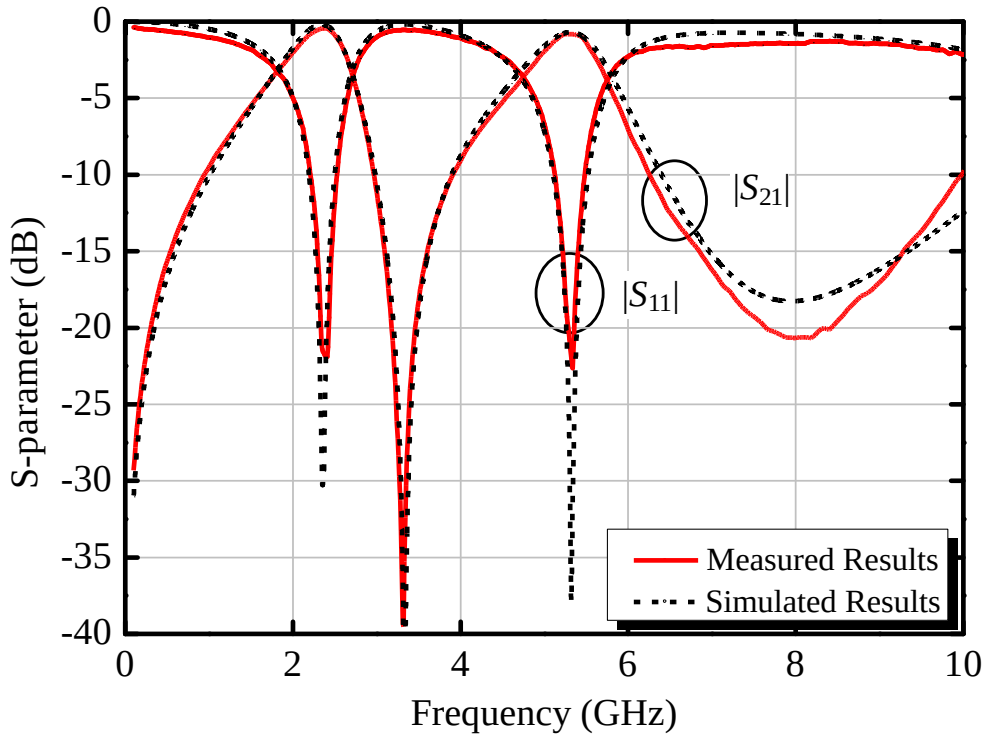

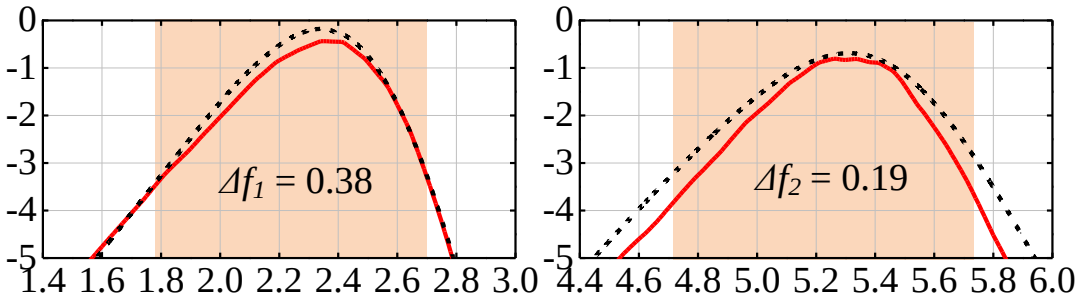

Figure 4.7 Transmission responses of the first-order dual-band BPF.

4.4 Fourth-order Dual-band BPF

To design higher-order dual-band filters, proper coupling scheme is required meet the required coupling coefficients (k) for two respective bands. It is known from [96] that when two resonators are placed in close proximity, their coupling coefficient k at each designed band are related to the resonant frequencies as

$$k_i = \frac{f_{H,i}^2 - f_{L,i}^2}{f_{H,i}^2 + f_{L,i}^2} \tag{4.9}$$

where i = 1 or 2 denotes the first and second passband, and $f_{H,i}$ and $f_{L,i}$ can be obtained by using Eigen-mode simulation on its 3-D structure. For each of the passbands, there are N resonators in an N-order filter. In our filter design, the coupling coefficients between the nth and (n+1)th resonators are determined by the Chebyshev low-pass filter prototype, with the element values $g_{n,i}$ and $g_{n+1,i}$, and fractional bandwidth (FBW) Δf_i related as

$$\Delta f_i = k_i \sqrt{g_{n,i} g_{n+1,i}} \tag{4.10}$$

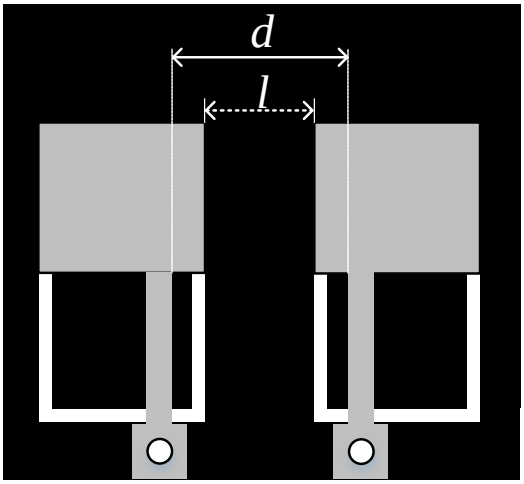

Figure 4.8 Parallel coupling scheme for higher-order dual-band filters.

The parallel coupling scheme in Figure 4.8 is adopted. The main parameter is the distance between two resonator cells *l*, which measures the distance between two resonators. To provide another degree-of-freedom, the high-impedance section of SIR is shifted, which leads to the second parameter *d* that measures the distance between the adjacent high-impedance sections. It should be noted that this dual-band resonator maintains the same resonant characteristic as the proposed resonator. The only purpose of this minor modification here is to meet the dual-band coupling requirements.

In the following, we elaborate the design of fourth-order 2.4-/5.2-GHz filter. For 0.2-dB ripple levels at both bands, $g_{0,i}$ = 1.0, $g_{1,i}$ = 1.3028, $g_{2,i}$ =

1.2844, $g_{3,i}$ = 1.9761. Due to the symmetry, only two coupling coefficients are to be determined, i.e. the $(k_{12})_i = (k_{34})_i$ that denotes the coupling between the 1st and 2nd (or 3rd and 4th) resonators, and the $(k_{23})_i$ that denotes the coupling between 2nd and 3rd resonators. Assuming l (mil) = 8, 10, 12, 14, 16, 18 and d (mil) = 44, 64, 84, 104, 124, 144, 164, the coupling coefficients are extracted using Eigen-mode simulation with (4.9). Using (4.10), an FBW design graph is constructed as in Figure 4.9. It is noted that the bottom axis and left axis are used to determine the physical parameters l and d between 1st and 2nd (or 3rd and 4th) resonators, while the top axis and right axis are for 2nd and 3rd resonators.

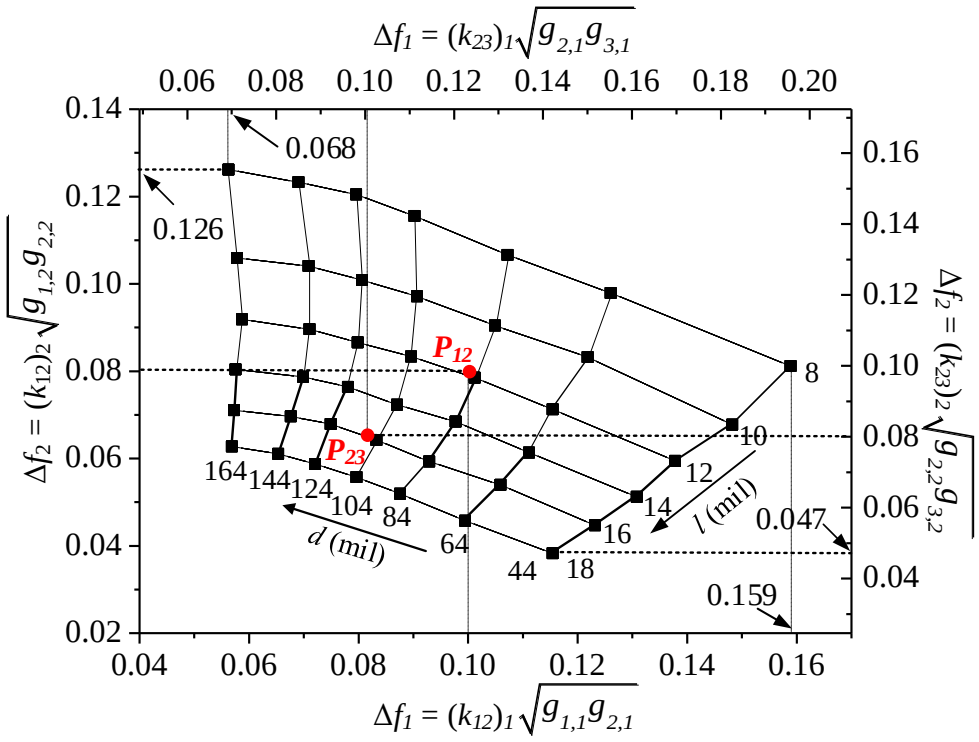

Figure 4.9 FBW design graph based on Chebyshev low-pass filter prototype with 0.2-dB ripple levels for f_1 = 2.4 GHz and f_2 = 5.2 GHz. (Resonator dimensions in Figure 4.8 for k extraction: w_1 = 10, l_1 = 200, w_{11} = 96, l_{11} = 200, $w_{1'}$ = 10, $l_{1'}$ = 200, $w_{11'}$ = 74, $l_{11'}$ = 200, s = 10, v_d = 50, unit: mil)

It is noted that any feasible set of l and d values have to meet $(k_{12})_i$ and $(k_{23})_i$ requirements for specified FBW requirements at two bands simultaneously. For the parametric l and d values in Figure 4.9, possible Δf_1 is from 0.068 to 0.159 and Δf_2 is from 0.047 to 0.126. The targeted FBW is Δf_1 = 0.10 and Δf_2 = 0.08. Thus, we locate a point P_{12} with l_{12} = 12 mils and d_{12} = 87 mils to achieve the required $(k_{12})_i$, and locate another point P_{23} with l_{23} = 16 mils and d_{23} = 110 mils to achieve the required $(k_{23})_i$.

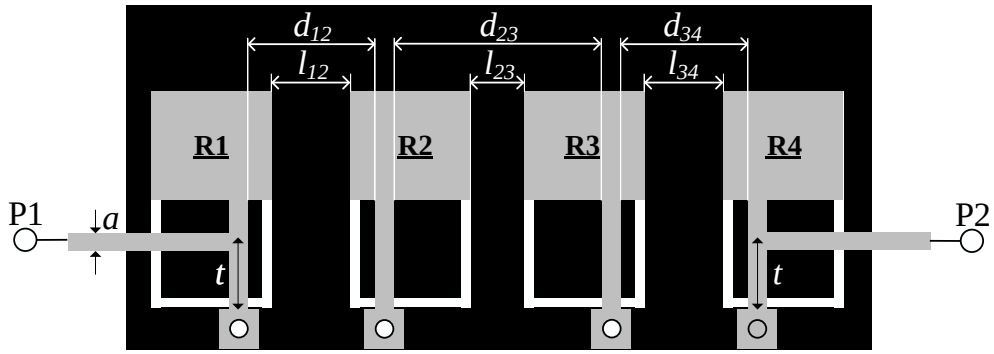

Figure 4.10 Fourth-order dual-band BPF.

The fourth-order filter is constructed as shown in Figure 4.10. Now, it is important to determine feeding structure based on the external quality factor (Q_e) of the filter. The required Q_e at each band can be calculated by following the method [96]

$$Q_{e,i} = \frac{g_{0,i} \cdot g_{1,i}}{\Delta f_i} \tag{4.11}$$

By simulating a singly loaded resonator using tapped line structure feedings, the external quality factor is extracted by

$$Q_{e,i} = \frac{\omega_i \cdot \tau_{S_{11}}(\omega_i)}{4} \tag{4.12}$$

where ω_i is the resonant angular frequency at each band, $\tau_{S11}(\omega_i)$ is the group delay of S_{11} at the resonant frequency. Based on the discussed in [98], two parameters are used here to provide the required Q_e for two bands, i.e. the port location t and the port width a. From equalizing (4.11) to (4.12) and EM extractions, t = 110 mils and a = 15 mils are selected for input/output coupling.

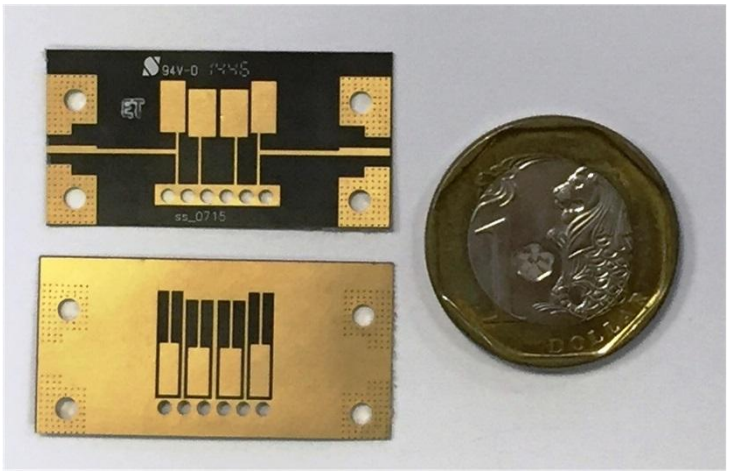

Figure 4.11 Photograph of the fabricated fourth-order dual-band BPF. (Resonator 1 and 4: w_1 = 10, l_1 = 198, w_{11} = 96, l_{11} = 198, $w_{1'}$ = 10, $l_{1'}$ = 198, $w_{11'}$ = 74, $l_{11'}$ = 198, s = 12; Resonator 2 and 3: w_1 = 10, l_1 = 182, w_{11} = 108, l_{11} = 182, $w_{1'}$ = 10, $l_{1'}$ = 182, $w_{11'}$ = 82, $l_{11'}$ = 182, s = 12; and l_{12} = l_{34} =12, d_{12} = d_{34} = 87, l_{23} = 16, d_{23} = 128, v_d = 50, t = 124, a = 19.5, unit: mil)

Considering the loading effects from the input/output ports, the final dimensions are slightly tuned from initial settings, and optimized using EM simulations. Figure 4.11 shows the fabricated fourth-order bandpass filter with its dimensions in the figure caption.

Figure 4.12 shows the measured results in a good agreement with our design target and simulated results. The filter features an insertion loss of 1.7 dB at 2.42 GHz with a 3-dB FBW of 0.12 at 2.4-GHz band and an insertion loss of 2.95 dB at 5.26 GHz with a 3-dB FBW of 0.10 at 5.2-GHz band. The return losses are better than 10 dB for both passbands. The designed filter shows a sharp roll-off and high inter-band isolation better than 28 dB. The upper stopband achieves better than 15 dB rejection up to 10 GHz.

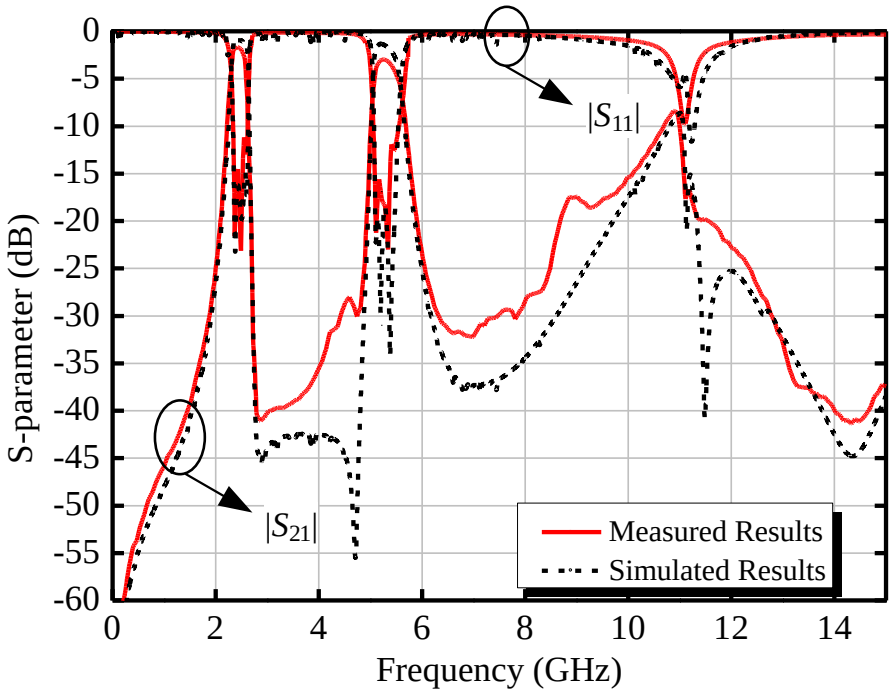

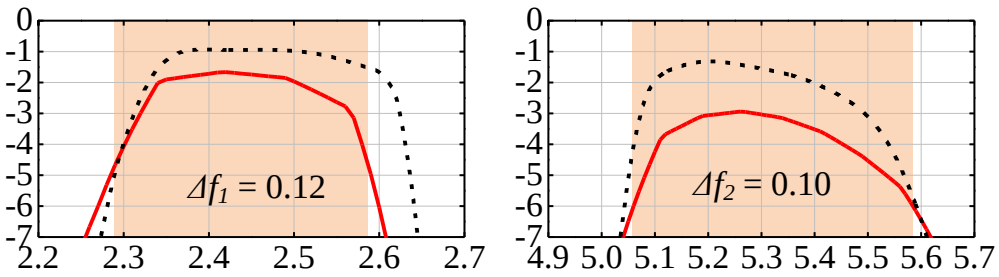

Figure 4.12 Transmission responses of the fourth-order dual-band BPF.

Table I Comparison with similar BPFs.

BPF	Size (λg x λg)	FBW (%) 1st, 2nd Bands	IL (dB) 1st, 2nd Bands	Freq. ratio	Tech.	Type of Operation	Independency of two bands
[105]	0.67 x 0.3	8.6, 6.1	0.8, 1	1.44	SIW	TE10	N-Given
[106]	0.7 x 0.3	16, 8.6	1.78, 2.53	1.43	Planar	TEM	N-Given
[107]	0.17 x 0.07	6.2, 5.2	1.4, 1.6	1.39	4-Layer SIW	TE10-TE30	No
[108]	0.93 x 0.88	4.5, 4.1	4.8, 4.8	1.53	10-Layer LTCC	TE10-TE20	No
[109]	2.1 x 1.3	3, 2.9	1.37, 1.1	1.2	SIW	TE10	No
[110]	2.7 x 1.27	2.8, 5.57	2.9, 2.7	1.14	SIW	TE10-TE20	Yes
[111]	0.64 x 0.18	8, 5	2.8, 4.5	1.35	Planar	TEM	Yes
[112]	0.2 x 0.19	4.59, 3.58	2.25, 2.25	1.37	CSRR	Evanescent	Yes
[23]	0.42 x 0.12	19.3, 13	1, 1	1.4	CSRR	Evanescent	Yes
[1]	0.16 x 0.15	5.8, 6.45	3.6, 3.1	2	DGS	Evanescent	Yes
This Work	**0.135 × 0.135**	**12, 10**	**1.7, 2.9**	**2**	**Planar**	**TEM**	**Yes**

4.5 Summary

The 2.4-/5.2-GHz filter was designed based on the proposed mixed coupled SIR/CPW-SIR resonator structure. The fabricated fourth-order filter shows a 3-dB FBW of 0.12 at 2.4-GHz band and a 3-dB FBW of 0.10 at 5.2-GHz band. The insertion loss is 1.7 dB and 2.9 dB at each passband. The filter is applicable for future WLAN and mobile systems, with features of low insertion loss, compact size, sharp roll off, and high rejection.

CHAPTER 5

New DGS Resonators for Advanced Bandpass Filter Designs

Substrate integrated waveguide (SIW), synthesized on planar substrate using periodic arrays of metalized vias, has been widely used as the platform for implementing low-cost and integrated waveguide filters [5]. With the merits of low-loss and high power handling capability, filters based on SIW technology still suffer from bulky sizes compared to their microstrip counterparts [99].

To circumvent with this issue, the bandpass filters (BPFs) with forward-wave or evanescent-mode wave which can propagate below SIW cut-off frequency (f_c) by loading DGS on SIW sides, were demonstrated in [25, 30, 100, 101] for filter miniaturization. In these works, the primary investigation was leveraged on complementary split ring resonator (CSRR) [102] and complementary open-loop resonator (COLR) as in Figure 5.1(a). The dual-mode and dual-band operations were demonstrated in [101] and [23], by means of loading two same- or different-sized CSRRs on the top side of SIW. To obtain lower resonant frequencies, same-sized CSRRs/COLRs were loaded on two sides of SIW in [100] and [25].

This Chapter presents two filter designs based on novel DGSs on SIW technology.

In the first design, a novel DGS shape named as back-to-back E-shaped DGS is proposed. By loading the back-to-back E-shaped DGS on either top or bottom sides of SIW, a dual-mode frequency response with two transmission zero points (ZPs) is obtained. To obtain dual-band response, a new two-side loading scheme with different-sized resonators on top and bottom sides is also proposed and analyzed. To validate the concept, a dual-band (2.4-/5.2-GHz) BPF is designed using Rogers RO4003 (ε_r = 3.38, tanδ = 0.0027) with thickness of 8 mil. The fabricated filter achieves good skirt selectivity, high inter-band isolation, good spurious response, and compact size.

In the second design, a fourth-order 60-GHz filter with quasi-elliptic frequency response is designed using SIW technology. A balanced DGSs shape is created to provide electrical coupling that leads to two additional attenuation poles. The mutual coupling between adjacent and non-adjacent TE_{101} mode SIW resonators are extracted, and used for filter synthesis.

5.1 Back-to-back E-shaped DGS for Miniaturized Dual-band SIW Bandpass Filter Designs

In the part, a novel DGS shape named as back-to-back E-shaped DGS is proposed. By loading the back-to-back E-shaped DGS on either top or bottom

sides of SIW, a dual-mode frequency response with two transmission zero points (ZPs) is obtained. To obtain dual-band response, a new two-side loading scheme with different-sized resonators on top and bottom sides is also proposed and analyzed.

5.1.1 Back-to-back E-shaped DGS

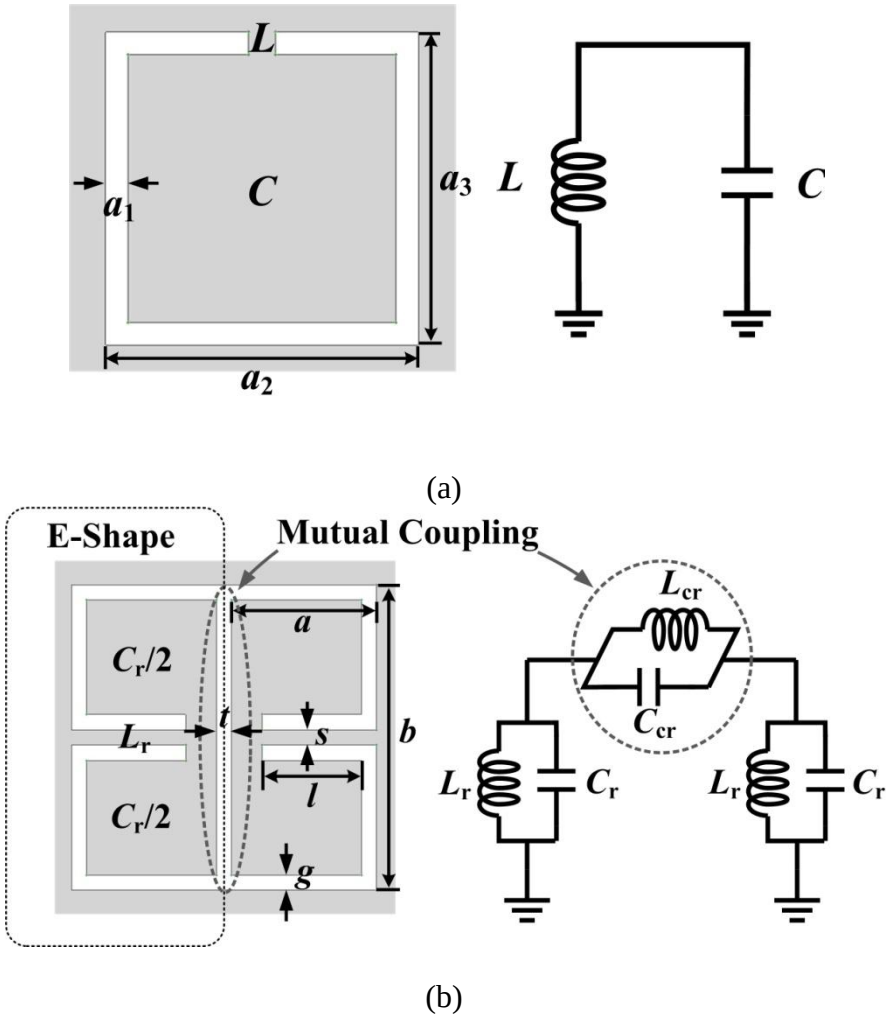

Figure 5.1 Configuration and equivalent circuit of (a) the complementary open-loop resonator [10] and (b) the proposed back-to-back E-shaped DGS unit. (Grey zone: metallization; White zone: defected area)

As shown in Figure 5.1(b), the back-to-back E-shaped DGS is formed by two E-shapes in back-to-back orientation. From its physical configuration, the E-shaped DGSs can be modeled as *LC* resonators (L_r and C_r) with L_{cr} and C_{cr} denoting their mutual magnetic and electric couplings. The resonant frequencies of each E-shaped DGS are determined by *a*, *b*, *g*, *l*, and *s*.

The transmission responses are investigated by using ANSYS's HFSS V14 software packages. As shown in Figure 5.2(a), the unloaded SIW has a high-pass frequency response with f_c at 9.5 GHz.

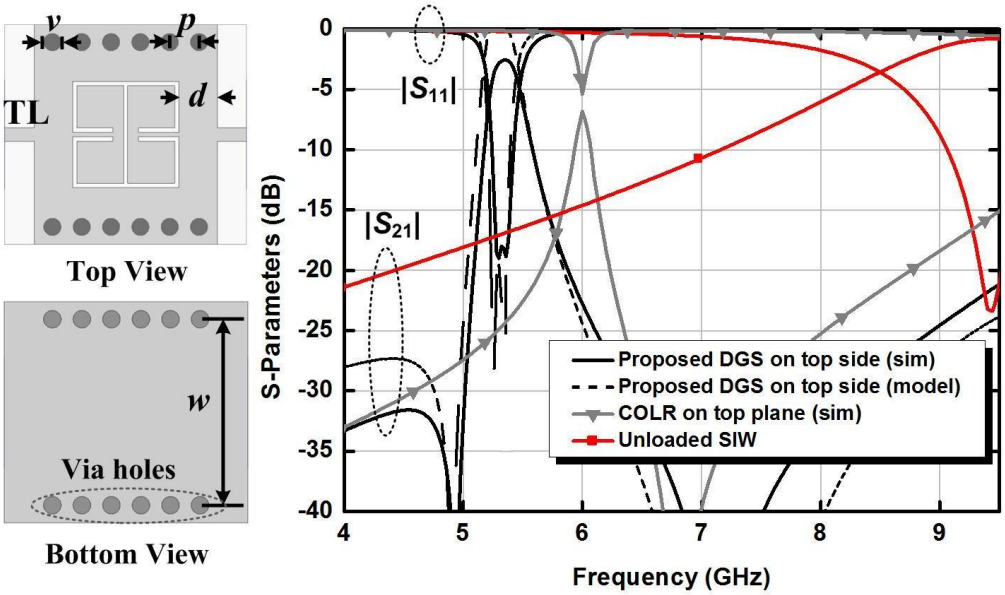

(a)

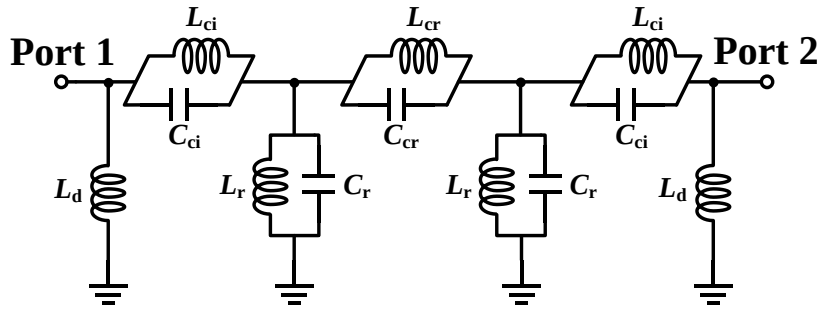

(b)

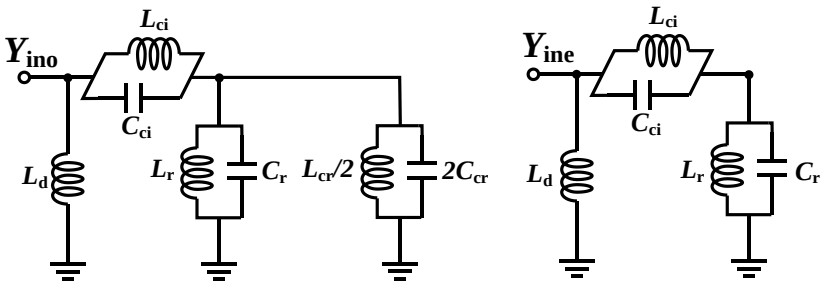

(c)

Figure 5.2 Investigation of SIW loaded by back-to-back E-shaped DGS and COLR on the top side: (a) configurations and transmission responses; (b) equivalent circuit model of SIW loaded by unit back-to-back E-shaped DGS; (c) even- and odd-mode circuits. (Grey zone: metallization; White zone: defected area; Physical parameters: for SIW d = 50, v = 24, p = 40, w = 372, for single ring CSRR a_1 = 6, a_2 = 145, a_3 = 145, for back-to-back E-shaped DGS: a = 70, b = 145, s = 6, l = 49, g = 6, t = 5 with unit in mil; Circuit elements: L_{ci} = 0.696 nH, C_{ci} = 0.692 pF, L_r = 0.685 nH, C_r = 1.68 pF, L_{cr} = 1.48 nH, C_{cr} = 0.711 pF, and L_d = 1.03 nH)

Firstly, the SIW is loaded by COLR unit as the reference. It is observed that a transmission pole is created at 6 GHz, with one ZP at 6.9 GHz.

Secondly, the SIW is loaded by the proposed DGS in the same size. Compared to COLR, the proposed DGS achieves two transmission poles at 5.3 and 5.35 GHz as shown in Figure 5.2(a), that potential benefits circuit

miniaturization, enhances frequency selectivity by generating two transmission ZPs, and extends upper stopband attenuation of 20 dB to 9.5 GHz.

As shown in Figure 5.2(b), the equivalent circuit models are developed for the proposed filter. The two sides of SIW are treated as a two-wire transmission lines while the via arrays are modeled as inductors L_d [101]. The input coupling comprises of both magnetic and electric couplings that are represented as L_{ci} and C_{ci}. In Figure 5.2(a), the simulation results of the circuit model are well agreed with EM simulation results. Even- and odd-mode analysis is adopted to study the resonant properties. Using circuits in Figure 5.2(c), the odd-/even-mode input admittances are derived as in (5.1) and (5.2):

$$Y_{ino} = -\frac{j}{\omega L_d} + \frac{\left(-\frac{j}{\omega L_{ci}} + j\omega C_{ci}\right)\left[-\frac{j}{\omega}\left(\frac{1}{L_r} + \frac{2}{L_{cr}}\right) + j\omega\left(C_r + 2C_{cr}\right)\right]}{-\frac{j}{\omega}\left(\frac{1}{L_{ci}} + \frac{1}{L_r} + \frac{2}{L_{cr}}\right) + j\omega\left(C_{ci} + C_r + 2C_{cr}\right)} \tag{5.1}$$

$$Y_{ine} = -\frac{j}{\omega L_d} + \frac{\left(-\frac{j}{\omega L_{ci}} + j\omega C_{ci}\right)\left(-\frac{j}{\omega L_r} + j\omega C_r\right)}{-\frac{j}{\omega}\left(\frac{1}{L_{ci}} + \frac{1}{L_r}\right) + j\omega\left(C_{ci} + C_r\right)} \tag{5.2}$$

The odd- and even-mode transmission poles are located when Y_{ino} and Y_{ine} approaches infinity:

$$f_{\text{odd}} = \frac{\sqrt{L_r L_{cr} + L_{ci} L_{cr} + 2L_{ci} L_r}}{2\pi\sqrt{L_{ci} L_r L_{cr} (C_{ci} + C_r + 2C_{cr})}} \tag{5.3}$$

$$f_{\text{even}} = \frac{\sqrt{L_r + L_{ci}}}{2\pi\sqrt{L_{ci} L_r (C_{ci} + C_r)}} \tag{5.4}$$

where only odd-mode resonant frequency f_{odd} is influenced by the mutual coupling elements L_{cr} and C_{cr}. It is investigated by using EM simulation as the results given in Figure 5.3 by varying parameter t and extracting the coupling coefficients M as:

$$M = \frac{|\, f_{\text{odd}}{}^2 - f_{\text{even}}{}^2 \,|}{f_{\text{odd}}{}^2 + f_{\text{even}}{}^2} \tag{5.5}$$

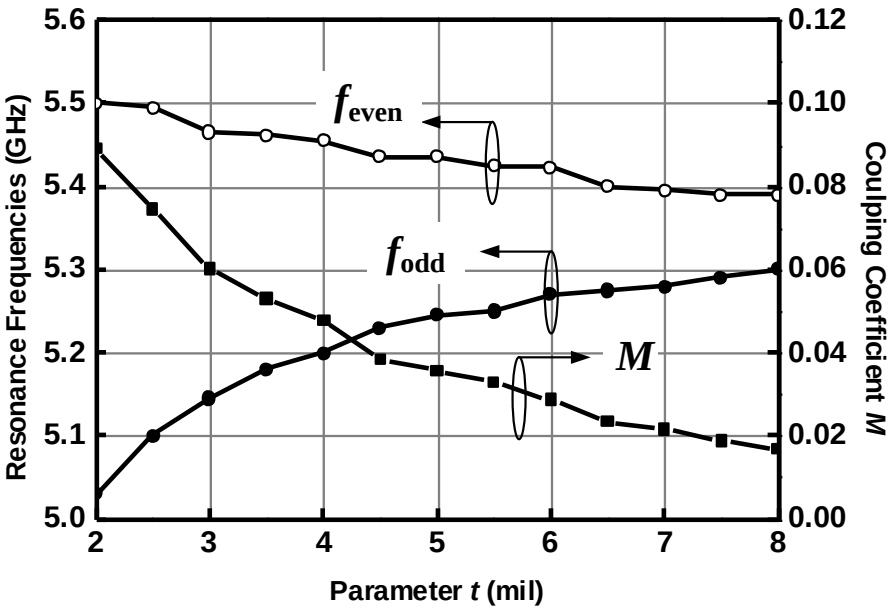

Figure 5.3 EM investigation of even, odd frequencies and coupling coefficient versus parameter *t*. (Parameters of structure in Figure 5.1 given in caption of Figure 5.2)

It is verified that f_{odd} is much more sensitive to the variation of k while f_{even} has negligible frequency shift. On the other hand, the transmission ZPs are determined using $Y_{ine} = Y_{ino}$ [96]:

$$f_{ZP1} = \frac{1}{2\pi\sqrt{L_{ci}C_{ci}}},\ f_{ZP2} = \frac{1}{2\pi\sqrt{L_{cr}C_{cr}}}. \tag{5.6}$$

which are controlled by the input and mutual couplings.

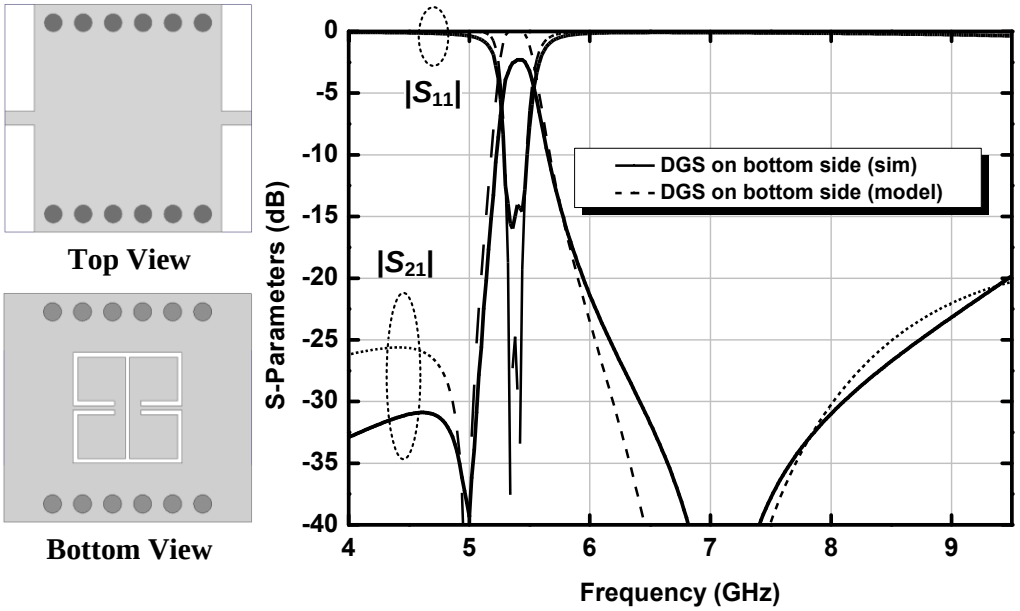

Figure 5.4 A 2nd-order bandpass filter design based on SIW loaded by back-to-back E-shaped DGS unit on the bottom side. (Physical parameters: same as the caption of Figure 5.2 with d = 52.5 mil; Circuit elements: L_{ci} = 0.686 nH, C_{ci} = 0.772 pF, L_r = 0.665 nH, C_r = 1.58 pF, L_{cr} = 1.48 nH, C_{cr} = 0.691 pF, and L_d =1.33 nH)

Based on the EM extraction parameters, the single band 2nd-order filter is designed. With a targeted FBW, the external quality factor (Q_e) and the

coupling coefficient (M_{12}) between two DGS resonators are determined through the circuit element of the Chebyshev low-pass filter prototype [96]. The example DGS filter operated in 5.2-GHz loaded on the bottom side of SIW is given in Figure 5.4.

5.1.2 Dual-band Bandpass Filter Design

As shown in Figure 5.5, a dual-band BPF is designed by loading DGS resonators on both top and bottom sides. A back-to-back E-shaped DGS filter on top side for the 5.2-GHz band and a DGS on bottom side for the 2.4-GHz band are proposed. The 2.4-GHz filter is designed first with fractional bandwidth (FBW) of 5.8%. The coupling coefficient is calculated as $Q_e = 12.97$ and $M_{12} = 0.089$. With 2.4-GHz resonator loaded on the bottom side, the 5.2-GHz passband is designed on the top side with FBW of 6.5%, the coupling matrix is generated as $Q_e = 14.54$ and $M_{12} = 0.079$. Since the frequency 5.2-GHz is 2.17 times of that of the 2.4-GHz band, the size of the 5.2-GHz BB-E-shaped DGS is much smaller than that of the 2.4-GHz one. As a result, 5.2-GHz filter has relatively less effect on the 2.4-GHz filter. The dual-band filter can be designed by EM optimization of the stacked 5.2-GHz filter on top and 2.4-GHz on bottom. Thus, compared to parallel loading two different-sized resonators on the same side [23], the size of proposed dual-band filter can be reduced by half.

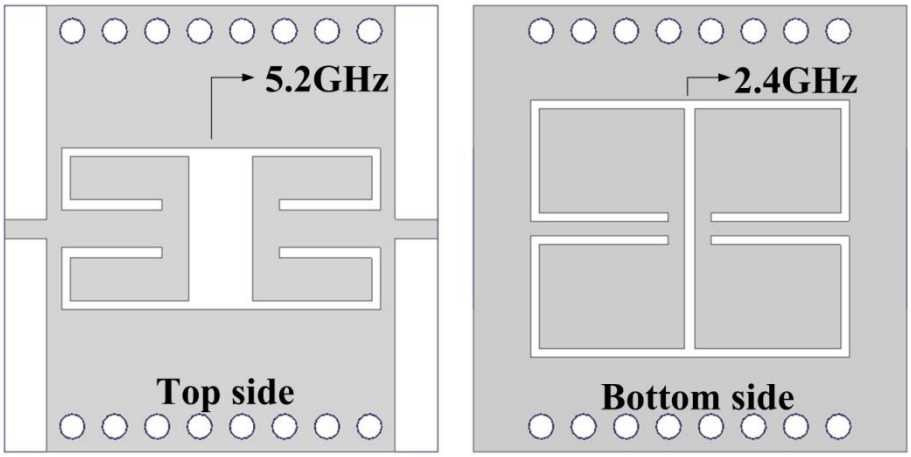

Figure 5.5 The 2.4-/5.2-GHz dual-band SIW BPF. (Physical parameters: Top side *s* = 35, *t* = 60, *a* = 120, *b* = 152, *g* = 8, *l* = 87, and *d* = 14; Bottom side *s* = 14, *t* = 10, *a* = 145, *b* = 242, *g* = 8, and *l* = 122)

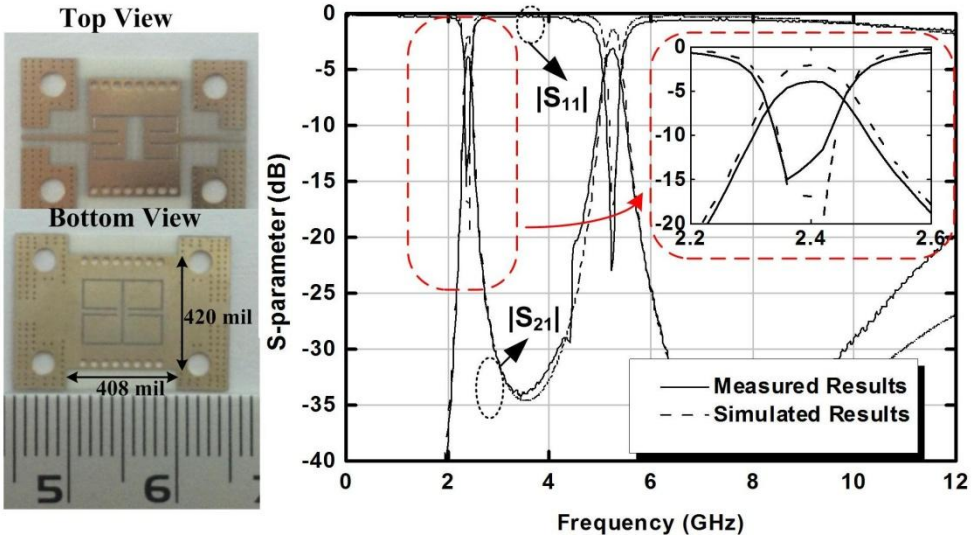

Figure 5.6 Photographs, simulated and measured S-parameters of the proposed filter.

Figure 5.6 shows the fabricated dual-band filter with a compact size of 408 mil × 420 mil (i.e. 0.152 λ_g × 0.156 λ_g, λ_g is the 2.4 GHz guided wavelength).

The measured results agree with the EM simulation result. For the 2.4-GHz band, the insertion loss is 3.6 dB with a 3-dB FBW of 5.8%. For the 5.2-GHz band, the insertion loss is 3.1 dB with FBW of 6.45%. The return losses are better than 15 dB in both passbands. The designed dual-band filter shows a sharp roll-off and high inter-band isolation better than 34 dB due to the generation of two transmission ZPs. The upper stopband with more than 20 dB attenuation extends to 12 GHz.

Table II Comparison with similar BPFs.

BPF	Size (λg x λg)	FBW (%) 1st, 2nd Bands	IL (dB) 1st, 2nd Bands	Freq. ratio	Tech.	Type of Operation	Independency of two bands
[105]	0.67 x 0.3	8.6, 6.1	0.8, 1	1.44	SIW	TE10	N-Given
[106]	0.7 x 0.3	16, 8.6	1.78, 2.53	1.43	Planar	TEM	N-Given
[107]	0.17 x 0.07	6.2, 5.2	1.4, 1.6	1.39	4-Layer SIW	TE10-TE30	No
[108]	0.93 x 0.88	4.5, 4.1	4.8, 4.8	1.53	10-Layer LTCC	TE10-TE20	No
[109]	2.1 x 1.3	3, 2.9	1.37, 1.1	1.2	SIW	TE10	No
[110]	2.7 x 1.27	2.8, 5.57	2.9, 2.7	1.14	SIW	TE10-TE20	Yes
[111]	0.64 x 0.18	8, 5	2.8, 4.5	1.35	Planar	TEM	Yes
[112]	0.2 x 0.19	4.59, 3.58	2.25, 2.25	1.37	CSRR	Evanescent	Yes
[23]	0.42 x 0.12	19.3, 13	1, 1	1.4	CSRR	Evanescent	Yes
This Work	**0.16 x 0.15**	**5.8, 6.45**	**3.6, 3.1**	**2**	**DGS**	**Evanescent**	**Yes**

5.2 Balanced DGSs for mm-Wave Bandpass Filter Design

A fourth-order 60-GHz filter with quasi-elliptic frequency response is designed using SIW technology. Two attenuation poles are created by introducing cross coupling between non-adjacent resonators. The mutual coupling between adjacent and non-adjacent TE_{101} mode SIW resonators are extracted, and used for filter synthesis.

5.2.1 Filter Configuration

In Figure 5.7, the proposed 60-GHz BPF is based on TE_{101} mode SIW cavity resonators. Its overall coupling structure is consists of both magnetic and electric coupling mechanism. The magnetic couplings are realized by magnetic post-wall irises, while electric coupling is achieved with balanced DGSs and two metallic via holes. This electric cross coupling of non-adjacent resonators (R1 and R4) is used to generate two additional attenuation poles at both sides of the passband for shape roll-off. A 50-Ω transmission line with coupling slots are directly connected to the resonators as the input/output ports.

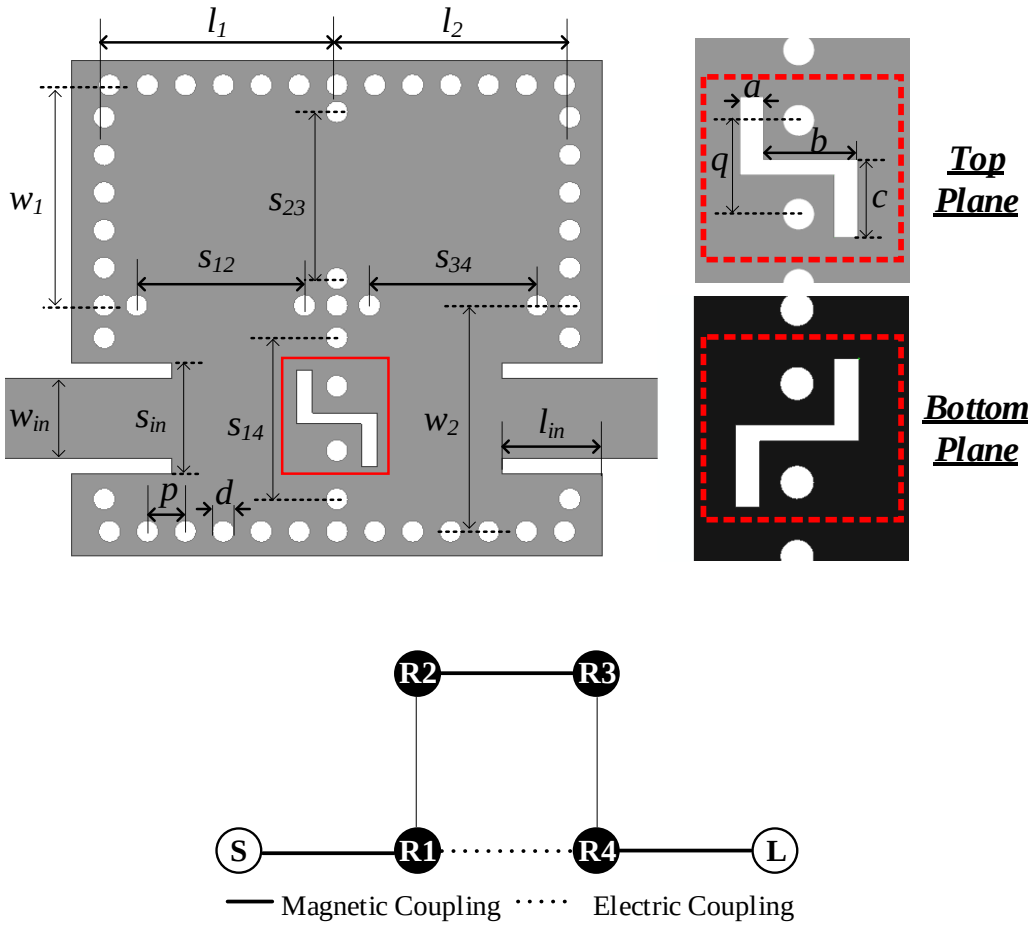

Figure 5.7 Top plane configuration of the 60-GHz SIW filter (bottom plane is fully metalized except the marked balanced DGSs area) and its coupling diagram.

The initial size of the -mode-based SIW cavity is determined by setting the resonant frequency at 60 GHz by using [103]

$$f_o = \frac{c_0}{2\sqrt{\varepsilon_r}}\sqrt{\frac{1}{w_{eff}^2}+\frac{1}{l_{eff}^2}} \tag{5.7}$$

$$w_{eff} = w - \frac{d^2}{0.95p}, l_{eff} = l - \frac{d^2}{0.95p}.$$

where w and l are the width and length of the TE_{101} SIW cavity, d and p are diameter and pitch of the metalized via holes, c_0 is the speed of light in free space, and ε_r is the dielectric constant of the substrate. In this design, due to the feature size limitation during fabrication (minimum length = 6 mils), d = 8 mils is chosen with p = 14 mils to satisfy the SIW cavity requirement of $p <= 2d$ [104].

5.2.2 Coupling Investigation

Figure 5.8 shows the configurations for coupling investigation and coefficient extractions between the TE_{101} mode resonators. The input/output ports are weakly coupled to the structures. The E-field distributions and calculated coefficients are plotted in Figure 5.9. Two split resonant frequencies are observed in both cases. By comparing the E-field distributions in Figure 5.9(a) and 5.9(b), it is noted that the E-field vector directions are reversed in the low-and high-mode of the two cases. It is the evidence that the coupling coefficients of two cases are of opposite types.

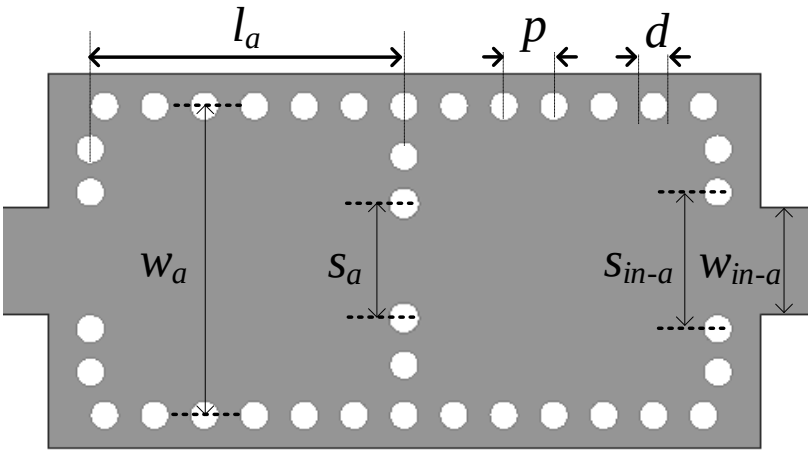

(a)

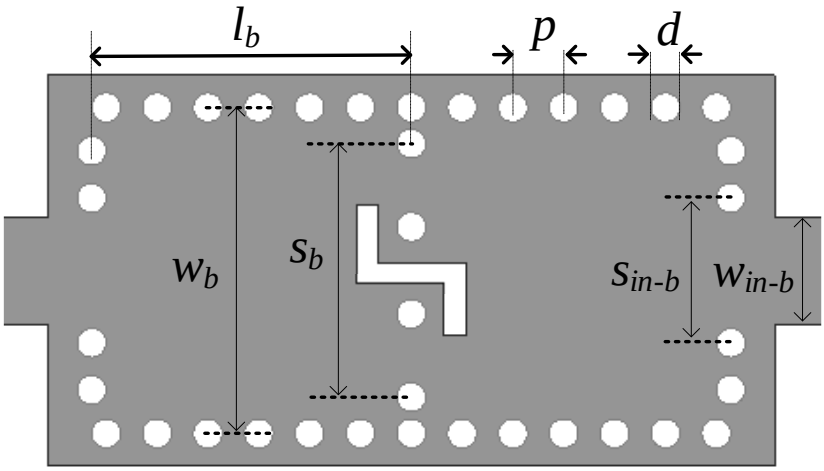

(b)

Figure 5.8 Circuit diagrams of (a) Magnetic coupling schematic, and (b) Electric coupling schematic.

In Figure 5.9(a), the via space s_a is used to tune the coupling strength, which is then extracted using EM simulation and

$$k_i = \frac{f_{H,i}^2 - f_{L,i}^2}{f_{H,i}^2 + f_{L,i}^2} \tag{5.8}$$

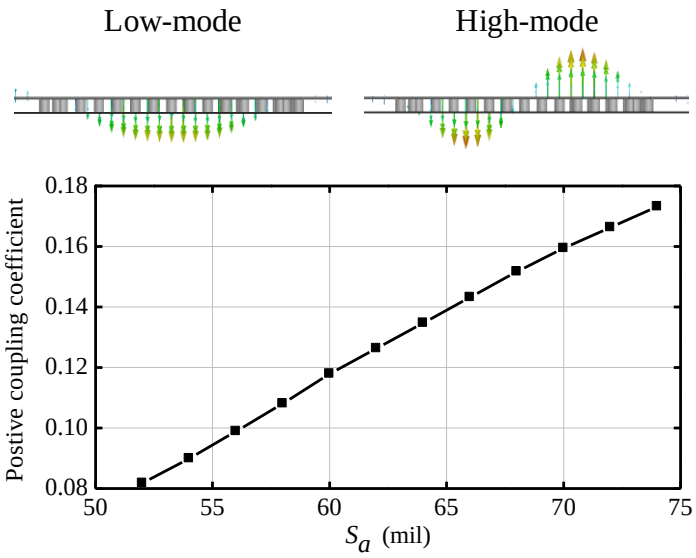

(a)

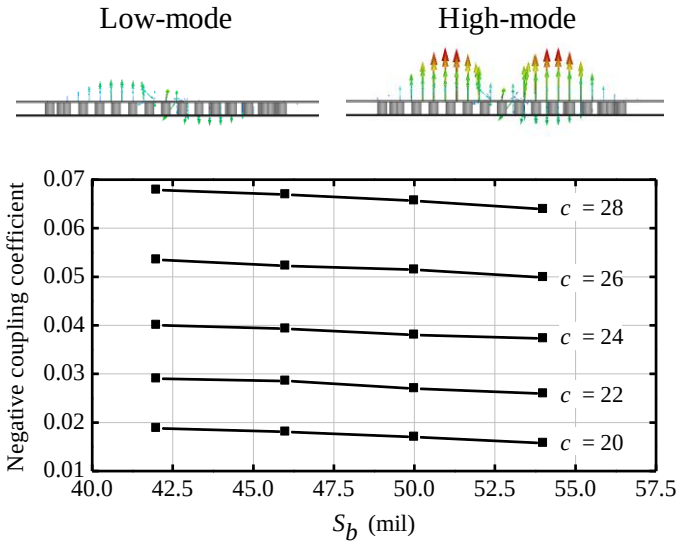

(b)

Figure 5.9 E-field distributions and extracted coupling coefficients of: (a) Magnetic coupling; (b) Electric coupling.

In the Figure 5.9(b), the via space s_b and the size of balanced DGSs (c) are both used to control the coupling strength. The coupling coefficient increases dramatically with DGS length c, while it slightly decreases with s_b. It is because the magnetic coupling created by post via walls increase with s_b, and cancels part of the dominant electric coupling created by DGSs.

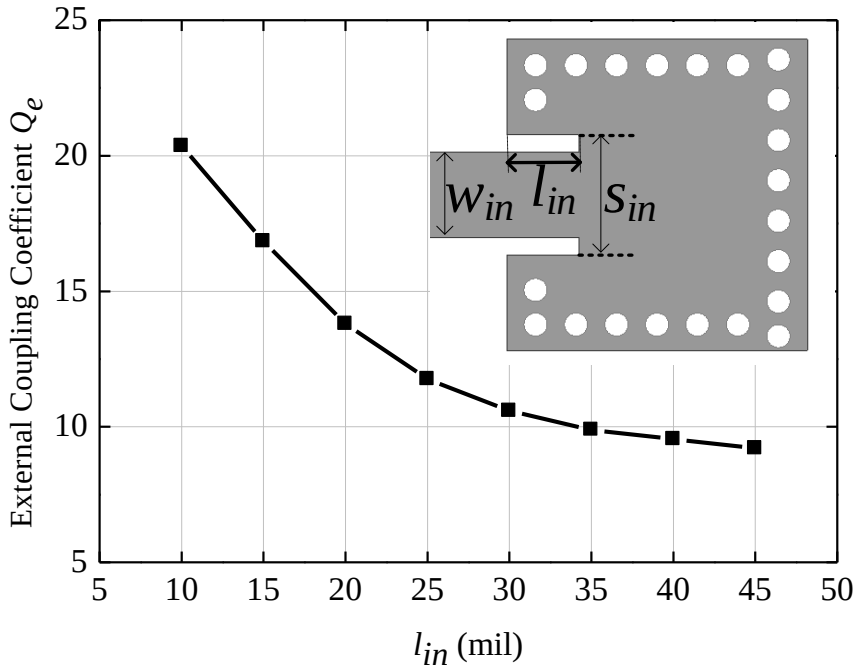

Figure 5.10 External coupling coefficient extraction using a singly loaded SIW cavity resonator.

In Figure 5.10, the external coupling (Q_e) is extracted using a singly loaded SIW cavity resonator. By varying the slot length of input/output ports, Q_e is calculated using

$$Q_{e,i} = \frac{\omega_i \cdot \tau_{S_{11}}(\omega_i)}{4}. \tag{5.9}$$

5.2.3 The Fourth-order 60-GHz Bandpass Filter

To achieve the design target listed in Table I, the filter parameters are calculated as: g_1 = 0.95974, g_2 = 1.42192, J_1 = -0.21083, J_2 = 1.11769, based on the four-degree quasi-elliptic filter prototype [96]. Thus, its coupling matrix is obtained as

$$[\mathrm{M}] = \begin{bmatrix} & S & 1 & 2 & 3 & 4 & L \\ S & 0 & 4.879 & 0 & 0 & 0 & 0 \\ 1 & 4.879 & 0 & 0.168 & 0 & -0.043 & 0 \\ 2 & 0 & 0.168 & 0 & 0.155 & 0 & 0 \\ 3 & 0 & 0 & 0.155 & 0 & 0.168 & 0 \\ 4 & 0 & -0.043 & 0 & 0.168 & 0 & 4.879 \\ L & 0 & 0 & 0 & 0 & 4.879 & 0 \end{bmatrix}. \tag{5.10}$$

Table III Design Targets of the 60-GHz BPF

Center frequency	61 GHz
Bandwidth	55-67 GHz / 0.197
In-band return loss	-20 dB
Attenuation pole locations	$\Omega_a = \pm 1.8$

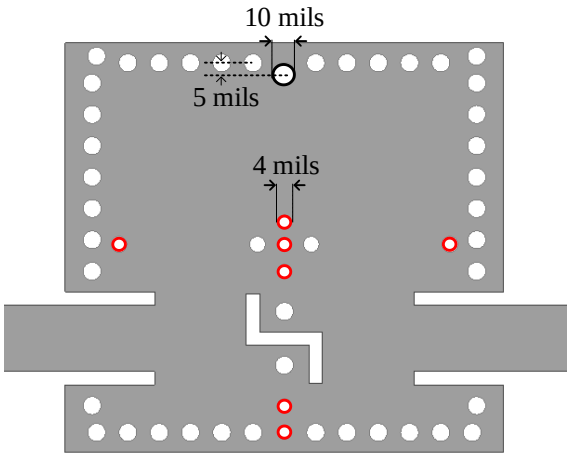

Figure 5.11 Top plane configuration of the finalized 60-GHz filter design. (l_1 = 86, w_1 = 81, w_2 = 82, s_{12} = 62, s_{23} = 66, s_{14} = 60, l_{in} = 40, w_{in} = 29.5, s_{in} = 41.5, p = 14, d = 8, a = 6, b = 28, c = 23, q = 24, unit: mil)

The initial design parameters are estimated based on Figure 5.9 and 5.10. Then, an EM-tuning process is performed to optimize the performance with the finalized dimensions shown in Figure 5.11. To cater for fabrication feasibility, the top two adjacent vias are merged into one via with diameter of 10 mils, while the vias marked in red circles have their diameter reduced to 4 mils.

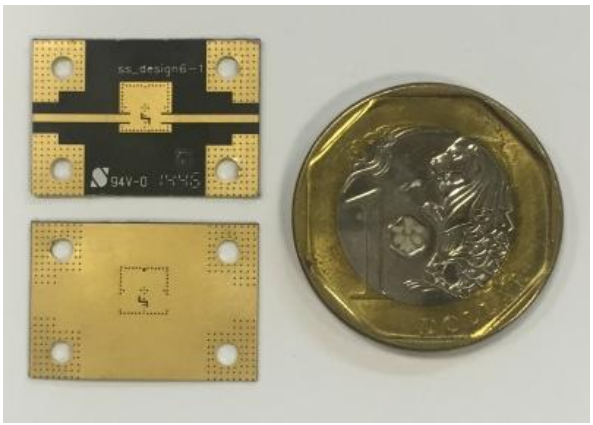

Figure 5.12 Photograph of the fabricated 60-GHz BPF.

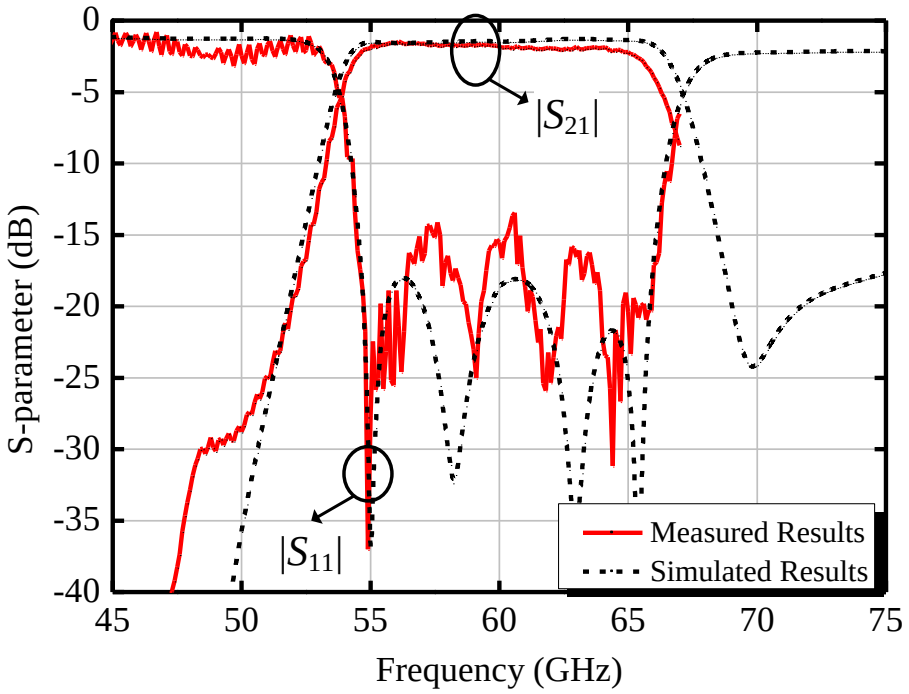

Figure 5.13 Transmission responses of the 60-GHz BPF.

Figure 5.12 shows the fabricated 60-GHz BPF. In good agreement with our design target and simulated results, the measurement shows a 3-dB FBW from 53.5 to 66.5 GHz (FBW = 0.217), insertion loss of 1.8 dB, return loss of better than 13 dB in the passband (as shown in Figure 5.13).

5.3 Summary

Novel DGS structures were designed, analysed, and applied to advanced filter designs. Firstly, the back-to-back E-shaped DGS and the two-side loading scheme of different-sized DGSs on top and bottom sides of SIW are proposed for miniaturized dual-band filter designs. Based on the analysis and

investigations, a 2.4-/5.2-GHz BPF was designed and verified experimentally. It is noted that the proposed back-to-back E-shaped DGS for SIW and loading scheme can be extended for miniaturized multi-band components. Secondly, the 60-GHz filter was designed based on SIW resonators and DGS. The fabricated filter has insertion loss of 2.0 dB and FBW from 53.5 to 66.5 GHz.

CHAPTER 6

A 2.4-/5.2-/60-GHz Tri-band Bandpass Filter for Future WLAN and Mobile Applications

The 802.11 WLAN standard has been continuously updated to permit higher transmission throughput. The relevant standard enhancements are 11a,b,g,n,ac and these cover two bands in the 2.4-GHz and the 5.2-GHz frequency ranges. Recently, the amendment of 11ad to WLAN standard defines the MAC and PHY layers for very high throughput in the 60-GHz range. In addition, the Federal Communications Commission (FCC) officially voted to pave the path in 2016, for 5G advancements to mobilize the millimeter-wave (mm-wave) frequencies. Thus, future wireless systems will have to feature both radio-frequency (1-6 GHz) and mm-wave transmissions. To build these systems with merits of low-cost and compact size, the associate filter solution is required to be developed properly.

Based on the theoretical study in Chapter 2-5, an application-oriented filter is designed and presented in this Chapter. To accommodate such large frequency ratio, a 2.4-/5.2-GHz dual-band BPF and a 60-GHz BPF are separately designed and connected in parallel with auxiliary low-pass filters (LPFs) and BPFs for signal isolation between the RF and mm-wave frequencies.

The 2.4-/5.2-GHz dual-band filter in Chapter 4, the 60-GHz filter in Chapter 5, and the DGS techniques in Chapter 2 are co-designed for the tri-band application.

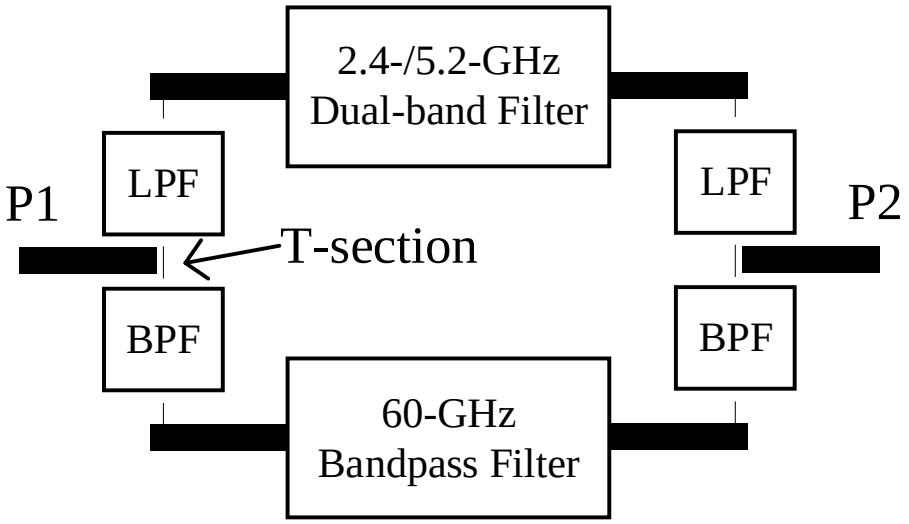

Figure 6.1 Architecture of the 2.4-/5.2-/60-GHz tri-band BPF.

Figure 6.1 shows the architecture of the tri-band filter. It comprises the 2.4-/5.2-GHz filter, the 60-GHz filter, and four auxiliary LPFs and BPFs. The design targets of these auxiliary filters are: 1) To ensure that all the 2.4 and 5.2 GHz signals transmit through the 2.4-/5.2-GHz filter, the LPFs need to have low insertion loss and good matching at 2.4- and 5.2-GHz bands, while the BPFs need to have high rejection at these bands. 2) Similarly, to ensure that all the 60 GHz signal transmit through the 60-GHz filter, the BPFs need to have low insertion loss and good matching at 60-GHz band, while the LPFs need to

have high rejection at this frequency. 3) In addition, the auxiliary LPFs and BPFs must be placed closely to the T-section.

6.1 Auxiliary Low-pass Filter

In Figure 6.2, the auxiliary LPF is designed by two cascaded stepped impedance LPFs with square open-stubs. It can be approximated to a classic *LC* ladder low-pass filtering circuit [96]. The open-stub is modelled as lump capacitor (*C*), while the short narrow sections and inter-connect TLs are lumped as inductors (*L*, L_1). Thus, the operating frequency and filter performance can be tuned and optimized by adjusting the physical parameters in the figure.

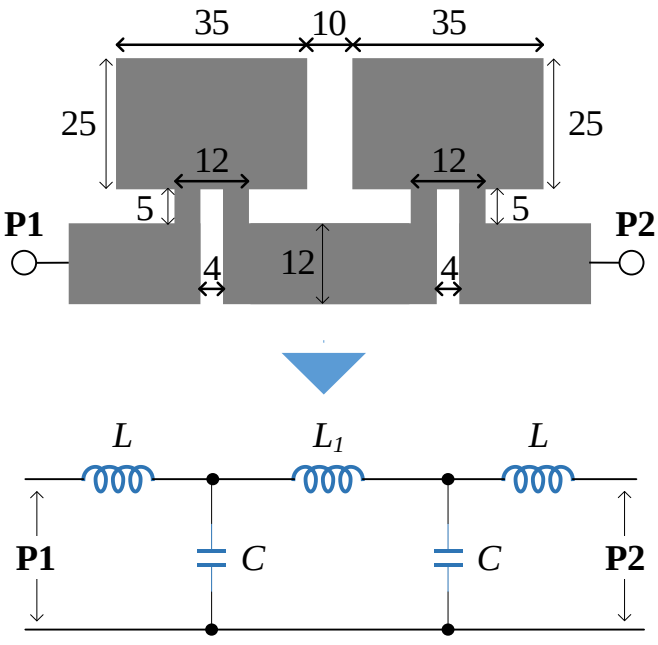

Figure 6.2 Top plane configuration of the auxiliary LPF (bottom plane is neglected; unit: mil), and its equivalent circuit model.

Figure 6.3 shows the simulated results of the filter in Figure 6.2. The 1-dB cut-off frequency is at 33 GHz. From 0 to 6 GHz, the insertion loss is less than 0.05 dB and return loss is better than 17.5 dB. At 60-GHz band, the rejection is better than 20 dB from 50 to 67 GHz. It is noted that we could reduce the cut-off frequency to around 8 GHz, which improves spurious rejection from 8 to 33 GHz. However, it also leads to poor rejection at 60-GHz band which does not fulfil our design target.

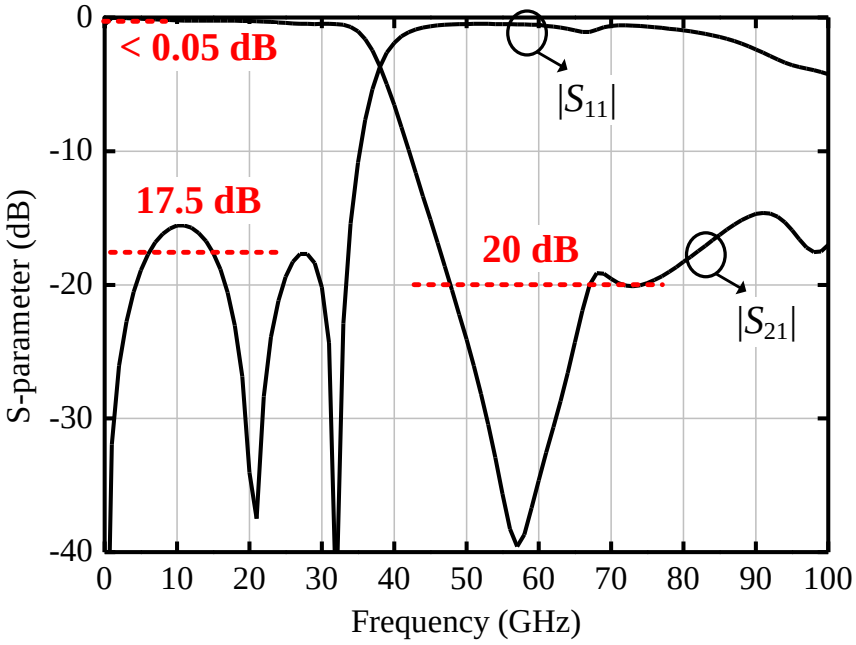

Figure 6.3 Simulated transmission responses of the auxiliary LPF.

6.2 Auxiliary Bandpass Filter

To meet the isolation requirement, either a high-pass filter (HPF) or a BPF at 60-GHz is adoptable. In the initial design, we intend to build an inter-digital

capacitor on the 50-ohm TL to form a HPF as shown in Figure 6.4. However, as the limited feature size of the fabrication technology, the number of fingers of the inter-digital capacitor is 1 or 2. Thus, to guarantee a large enough capacitance, the length of each finger has to be extended. Therefore, the series inductance of this capacitor becomes dominant as well, which leads to a series *LC* resonator and a bandpass response [97].

To further enhance the series inductance and capacitance, the square-shaped DGS is etched beneath the capacitor structure, in a size of 40 mils × 32 mils. In Figure 6.5, the simulated results show a rejection better than 20 dB below 6 GHz, an insertion loss less than 0.6 dB with minimum loss of 0.35 dB, and return loss better than 20 dB at 60-GHz band.

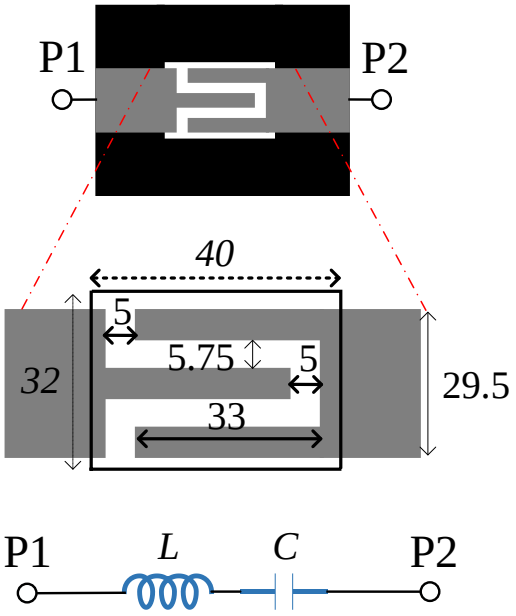

Figure 6.4 Top plane configuration of the auxiliary BPF (bottom plane is neglected; unit: mil), and its equivalent circuit model.

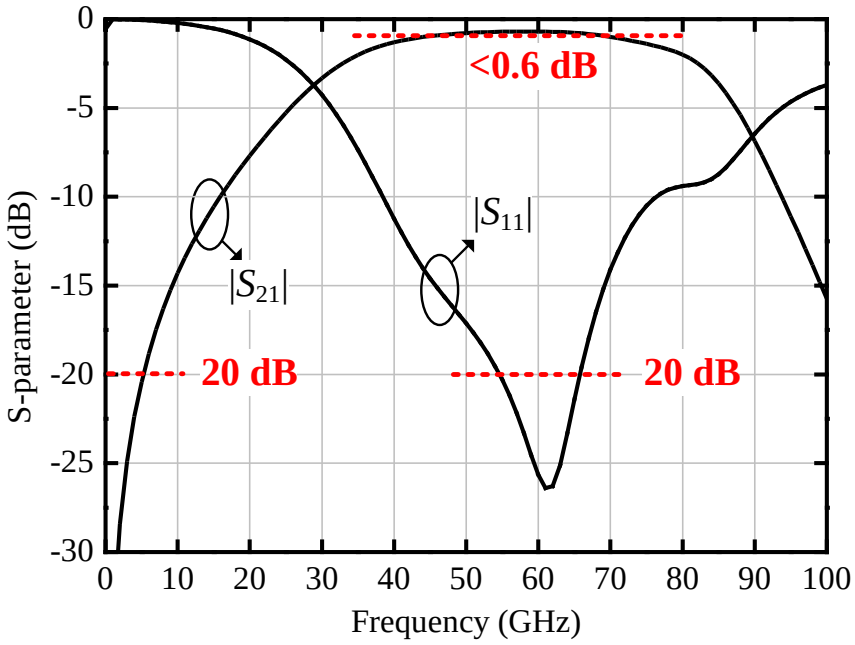

Figure 6.5 Simulated transmission responses of the auxiliary BPF.

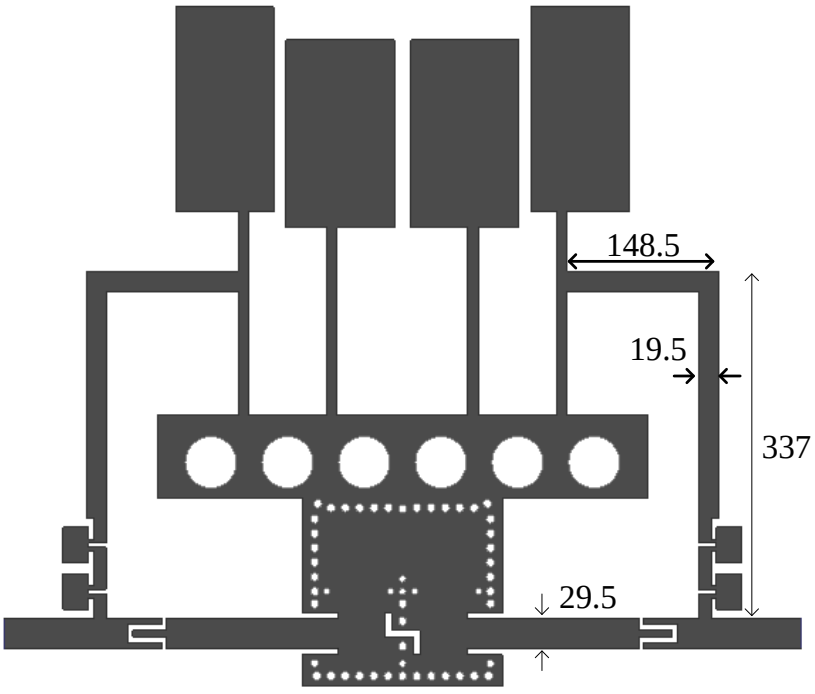

(a)

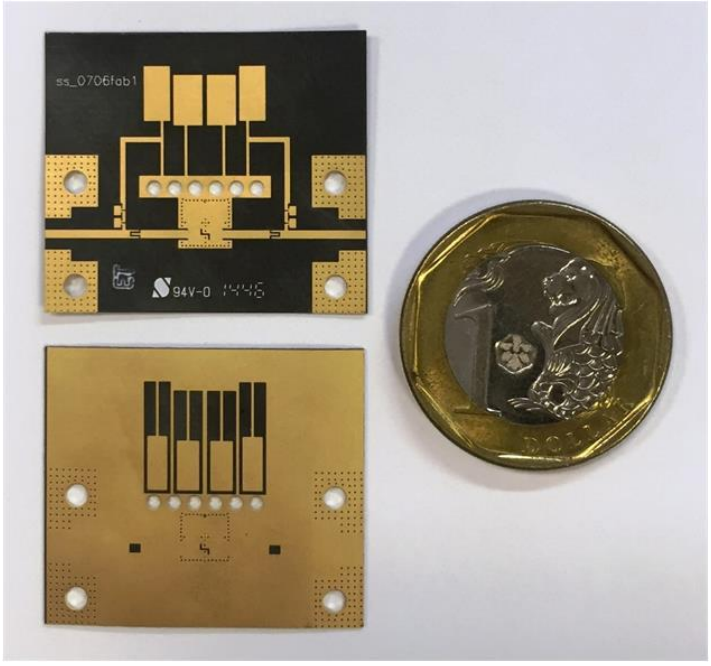

(b)

Figure 6.6 Top plane configuration of the auxiliary LPF. (Bottom plane is neglected; unit: mil)

6.3 Tri-band Filter Design

As shown in Figure 6.6(a), the 2.4-/5.2-/60-GHz tri-band filter is implemented with the filters discussed in previous. All the filter dimensions remain unchanged. In Figure 6.6(b), the fabricated filter including the area occupied by the input/output testing structures is 1170 mils × 1010 mils.

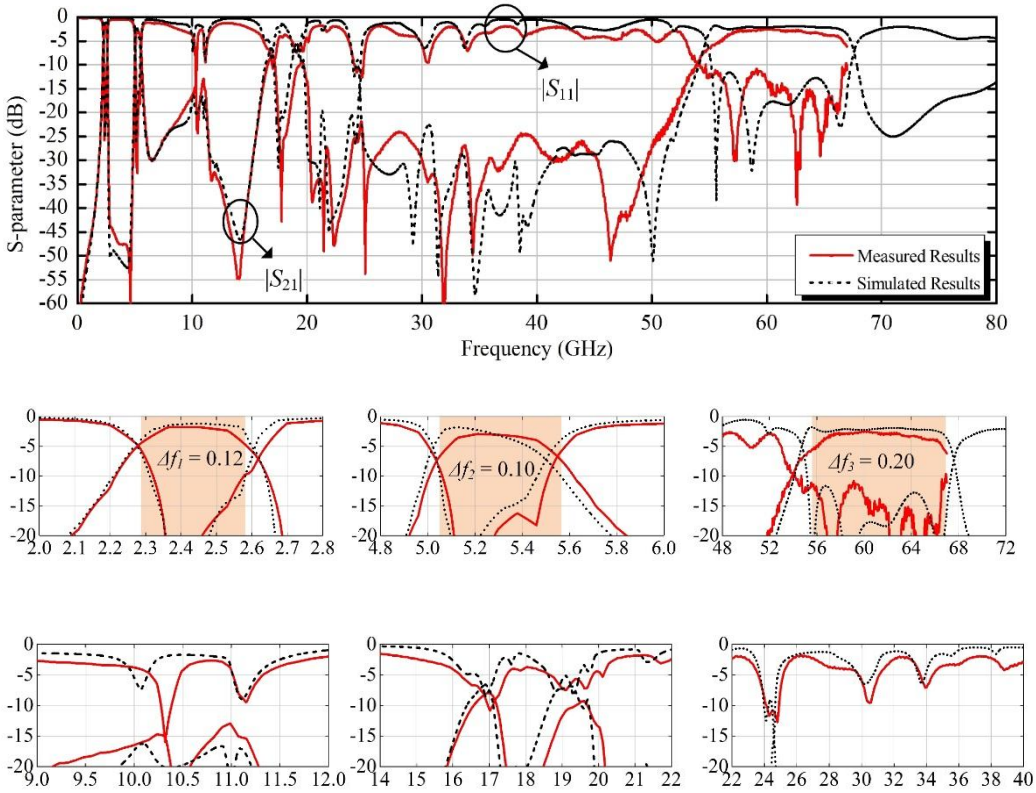

Figure 6.7 Transmission responses of the tri-band filter, with its passbands and spurious responses depicted in details.

In Figure 6.7, the filter is measured from DC to 67 GHz. First of all, three passbands are observed at 2.4-GHz, 5.2-GHz, and 60-GHz bands. At 2.4-GHz band, the insertion loss is 1.7 dB at 2.45 GHz with 3-dB FBW of 0.12. At 5.2-GHz band, the insertion loss is 3.0 dB at 5.3 GHz with 3-dB FBW of 0.10. At 60-GHz band, the insertion loss is 2.8 dB at 60 GHz with 3-dB FBW of 0.20.

The inter-band isolation is better than 25 dB, except the spurious frequencies at 10-11 GHz, 16-20 GHz, and 24 GHz. The spurious responses are resulted from high-order mode resonance of the SIR/CPW-SIR resonators. It

can be removed by adding some DGS resonators below the TLs of the 2.4-/5.2-GHz paths as done in [18].

6.4 Summary

In this Chapter, the tri-band filter was implemented. At 2.4-GHz band, the insertion loss is 1.7 dB at 2.45 GHz with 3-dB FBW of 0.12. At 5.2-GHz band, the insertion loss is 3.0 dB at 5.3 GHz with 3-dB FBW of 0.10. At 60-GHz band, the insertion loss is 2.8 dB at 60 GHz with 3-dB FBW of 0.20. The filter has advantages of low cost, low insertion loss, compact size, sharp roll off, and high isolation. It is applicable for future WLAN systems with 802.11ac and 11ad compliance, and 5G mobile communications.

CHAPTER 7

Conclusion and Future Work

7.1 Conclusion

This work mainly focuses on the fundamental theory and study of DGS, and its applications to conventional microstrip and SIW filter designs. Several novel DGS structures are proposed and used for high performance miniaturized filter designs.

Firstly, a new dual-T DGS is proposed to extend LPF spurious rejection. The DGS is proposed and etched on the ground plane of the transformed radial stub to form a high performance LPF with wide stopband rejection. The designed result shows an insertion loss of less than 0.5 dB from DC to 2.0 GHz, the stopband rejection of better than 20 dB from 2.5 GHz to 35 GHz and a sharp skirt selectivity. The size of the proposed LPF is only 2.19 cm × 1.25 cm.

Secondly, a new DGS is co-designed with SIR to form a new asynchronously tuned resonator. It is formed by mixed coupled stepped impedance resonator (SIR) and coplanar waveguide SIR (CPW-SIR) is proposed, analyzed, and applied to the 2.4-/5.2-GHz dual-band filter designs. The CPW-SIR is created using DGS on the ground plane. Fractional bandwidth

(FBW) design graph is constructed for the dual-band filter synthesis. Two filter prototypes (first-order and fourth-order) are fabricated and measured, which validate our design theory. Both filters have good measured results in an agreement with our design target and simulated results. The fourth-order filter features an insertion loss of 1.7 dB at 2.42 GHz with a 3-dB FBW of 0.12 at 2.4-GHz band and an insertion loss of 2.95 dB at 5.26 GHz with a 3-dB FBW of 0.10 at 5.2-GHz band. The return losses are better than 10 dB for both passbands. The designed filter shows a sharp roll-off and high inter-band isolation better than 28 dB. The upper stopband achieves better than 15 dB rejection up to 10 GHz.

Thirdly, new DGS structures are developed that form resonators when loaded on SIW technology. A novel back-to-back E-shaped defected ground structure (DGS) and two-side loading scheme for miniaturized dual-band substrate integrated waveguide (SIW) bandpass filter designs is proposed. The SIW loaded by novel DGS supports evanescent-mode wave propagation below the cut-off frequency of SIW, while achieves two transmission poles at the passband and two controllable transmission zero points. Furthermore, the novel loading scheme by loading different-sized DGS resonators on two sides of SIW is proposed for dual-band bandpass filter designs. To validate the design and analysis, a 2.4-/5.2-GHz filter prototype was designed. In good agreement with theoretical results, the measured results of the dual-band filter achieve insertion losses of 3.6 and 3.1 dB, and fractional bandwidths of 5.8% and 6.45% at 2.4

and 5.2 GHz respectively. The filter size is only 1.036cm × 1.06cm. Meanwhile, in the design of a 60-GHz filter, a balanced DGS is used to create electrical coupling between non-adjacent resonators for additional attenuation poles.

Lastly, a 2.4-/5.2-/60-GHz tri-band bandpass filter (BPF) is designed using two-layer PCB technology for the future WLAN and mobile applications. SIR, SIW, DGS, and CPW techniques are mixed-used in the design approach. To accommodate such large frequency ratio with common input/output, a 2.4-/5.2-GHz dual-band BPF and a 60-GHz BPF are separately designed and connected in parallel with auxiliary low-pass filters (LPFs) and BPFs for signal isolation and matching between the RF and mm-wave frequencies. The fabricated tri-band filter is measured, with results in a good agreement with simulation and theoretical analysis. It features insertion losses of 1.7/3.0/2.0 dB with FBW of 0.12/0.10/0.18 at 2.4-/5.2-/60-GHz bands respectively. The filter size is 1170 mils × 1010 mils.

7.2 Recommendations for Future Work

In this research work, several novel DGS structures are presented with their applications for advanced miniaturized/multi-band filter designs. The theoretical analysis and experimental results were obtained and compared to validate our design theory. Several filter prototypes were designed for modern RF systems.

In the future, the area that merits future works are listed below:

- Multiband filters with more than four bands: In this work, the bands generated from single resonator is only two. However, with the proposed multi-mode resonators, there are rooms to increase the number of bands. The theoretical analysis in the work is still valid and transformable for filter design cases with more bands.
- Designs of other RF components: In this work, only filter designs are explored using the proposed resonators. However, the same resonators are also applicable for other types of RF components, like antennas, duplexers, switches, and etc. Performance enhancement is expected from the new designs.
- Design for commercial products: In this work, even the filter design targets are for commercial applications, like the WLAN systems and 802.11ad. But none of the filters are fully packaged and verified with the most stringent industrial standards. Therefore, packaging solutions should be explored and co-designed with the filters presented in this work.

Author's Publications

[1] **S. Xu**, F. Meng, K. Ma, and K. S. Yeo, "A 2.4-/5.2-/60-GHz Tri-band Bandpass Filter," submitted to *IEEE Trans. Microw. Theory Tech*.

[2] **S. Xu**, K. Ma, F. Meng, and K. S. Yeo, "Novel defected ground structure and two-si*de loading scheme for miniaturized* dual-band SIW bandpass filter designs," *IEEE Microw. Wireless Compon. Lett.*, vol.25, no.4, pp.217-219, Apr. 2015.

[3] **S. Xu**, K. Ma, F. Meng, and K. S. Yeo, "DGS embedded transformed radial stub for ultra-wide stopband lowpass filter," *IET Electronic Lett.*, vol. 48, pp. 1473-1475, Nov. 2012.

[4] F. Meng, K. Ma, K. S. Yeo, C. C. Boon, W. M. Lim, and **S. Xu**, "A 220-285 GHz SPDT switch in 65-nm CMOS using switchable resonator concept," *IEEE Trans. THz Sci. Technol.*, vol. 5, pp. 649-651, Jul. 2015.

[5] F. Meng, K. Ma, K. S. Yeo, **S. Xu**, C. C. Boon, and W. M. Lim, "A 57-to-64 GHz 0.094-mm^2 5-bit passive phase shifter in 65-nm CMOS," *IEEE Trans. Very Large Scale Integr. (VLSI) Syst.*, vol. 24, pp. 1917-1925, May 2016.

[6] F. Meng, K. Ma, K. S. Yeo, **S. Xu**, C. C. Boon, and W. M. Lim, "Miniaturized 3-bit phase shifter for 60 GHz phased-array in 65 nm

CMOS technology," *IEEE Microw. Wireless Compon. Lett.*, vol. 24, pp. 50-52, Jan. 2014.

[7] **S. Xu**, K. Ma, and K. S. Yeo, "A transformed radial stub low-pass filter using defected ground structure for stopband extension (invited)," in *Int. SoC Design Conf. (ISOCC)*, pp. 82-83, Jeju Korea, 3-6 Nov. 2014.

[8] **S. Xu**, K. Ma, K. S. Yeo, and S. Mou, "A High Performance Low Pass Filter Design using Transformed Radial Stub and Defected ground Structures (invited)," in *The 26th Int. Techn. Conf. Circuits/Systems, Computers and Communications*, pp. 1166-1169, Gyeongju, Korea, 19-22 June 2011.

Bibliography

[1] S. Xu, K. Ma, F. Meng, and K. S. Yeo, "Novel Defected Ground Structure and Two-Side Loading Scheme for Miniaturized Dual-Band SIW Bandpass Filter Designs," *IEEE Microw. Wireless Compon. Lett.*, vol. 25, pp. 217-219, Feb. 2015.

[2] L. Gao, X. Y. Zhang, and Q. Xue, "Compact Tri-Band Bandpass Filter Using Novel Eight-Mode Resonator for 5G WiFi Application," *IEEE Microw. Wireless Compon. Lett.*, pp. 1-1, 2015.

[3] J. Xu, W. Wu, and G. Wei, "Compact Multi-Band Bandpass Filters With Mixed Electric and Magnetic Coupling Using Multiple-Mode Resonator," *IEEE Trans. Microw. Theory Tech.*, vol. 63, pp. 3909-3919, 2015.

[4] J. M. Yan, L. Z. Cao, J. Xu, and R. S. Chen, "Design of a Fourth-Order Dual-Band Bandpass Filter With Independently Controlled External and Inter-Resonator Coupling," *IEEE Microw. Wireless Compon. Lett.*, vol. 25, pp. 642-644, 2015.

[5] S. Wong, K. Wang, Z.-N. Chen, and Q.-X. Chu, "Design of Millimeter-Wave Bandpass Filter Using Electric Coupling of Substrate Integrated Waveguide (SIW)," *IEEE Microw. Wireless Compon. Lett.*, vol. 24, pp. 26-28, 2014.

[6] R. Zhang and L. Zhu, "Design of a Compact Dual-Band Bandpass Filter Using Coupled Stepped-Impedance Resonators," *IEEE Microw. Wireless Compon. Lett.*, vol. 24, pp. 155-157, 2014.

[7] C.-S. Chen, J.-F. Wu, and Y.-S. Lin, "Compact single-pole-double-throw switchable bandpass filter based on multicoupled line," *IEEE Microw. Wireless Compon. Lett.*, vol. 24, pp. 87-89, 2014.

[8] A. Ghaffari, E. A. M. Klumperink, F. van Vliet, and B. Nauta, "A 4-element phased-array system with simultaneous spatial- and frequency-domain filtering at the antenna inputs," *IEEE J. Solid-State Circuits*, vol. 49, pp. 1303-1316, 2014.

[9] R. Zhang and L. Zhu, "Synthesis of Dual-Wideband Bandpass Filters With Source-Load Coupling Network," *IEEE Trans. Microw. Theory Tech.*, vol. 62, pp. 441-449, 2014.

[10] R. Zhang and L. Zhu, "Synthesis and design of dual-wideband bandpass filters with internally-coupled microstrip lines," *IET Microw. Antennas Propag.*, vol. 8, pp. 556-563, 2014.

[11] H. Min-Hua and L. Cheng-Siou, "Novel Balanced Bandpass Filters Using Substrate Integrated Half-Mode Waveguide," *IEEE Microw. Wireless Compon. Lett.*, vol. 23, pp. 78-80, 2013.

[12] K. Ma, S. Mou, and K. S. Yeo, "A miniaturized millimeter-wave standing-wave filtering switch with high P1dB," *IEEE Trans. Microw. Theory Tech.*, vol. 61, pp. 1505-1515, 2013.

[13] R. Zhang and L. Zhu, "Synthesis and Design of Wideband Dual-Band Bandpass Filters With Controllable In-Band Ripple Factor and Dual-Band Isolation," *IEEE Trans. Microw. Theory Tech.,* vol. 61, pp. 1820-1828, 2013.

[14] J. Xu, W. Wu, and C. Miao, "Compact Microstrip Dual-/Tri-/Quad-Band Bandpass Filter Using Open Stubs Loaded Shorted Stepped-Impedance Resonator," *IEEE Trans. Microw. Theory Tech.,* vol. 61, pp. 3187-3199, 2013.

[15] C. J. You, Z. N. Chen, X. W. Zhu, and K. Gong, "Single-Layered SIW Post-Loaded Electric Coupling-Enhanced Structure and Its Filter Applications," *IEEE Trans. Microw. Theory Tech.,* vol. 61, pp. 125-130, 2013.

[16] X. Tang and K. Mouthaan, "Design of large bandwidth phase shifters using common mode all-pass networks," *IEEE Microw. Wireless Compon. Lett.,* vol. 22, pp. 55-57, 2012.

[17] Y.-Y. Huang, H. Jeon, Y. Yoon, W. Woo, C.-H. Lee, and J. S. Kenney, "An ultra-compact, linearly-controlled variable phase shifter designed with a novel RC poly-phase filter," *IEEE Trans. Microw. Theory Tech.*, vol. 60, pp. 301-310, 2012.

[18] S. Xu, K. Ma, F. Meng, and K. S. Yeo, "DGS embedded transformed radial stub for ultra-wide stopband lowpass filter," *IET Electronics Lett.*, vol. 48, pp. 1473-1475, 2012.

[19] W. Zhu-Dan, W. Feng, Z. Li, and S. Xiao-Wei, "Design of dual-band bandpass SIW filter with DGS," in *Int. Conf. Microw. Millimeter Wave Technol.*, 2012, pp. 1-3.

[20] A. L. Franc, E. Pistono, D. Gloria, and P. Ferrari, "High-Performance Shielded Coplanar Waveguides for the Design of CMOS 60-GHz Bandpass Filters," *IEEE Electron Devices,* vol. 59, pp. 1219-1226, 2012.

[21] R. Zhang and L. Zhu, "Synthesis Design of a Wideband Bandpass Filter With Inductively Coupled Short-Circuited Multi-Mode Resonator," *IEEE Microw. Wireless Compon. Lett.,* vol. 22, pp. 509-511, 2012.

[22] R. K. Pokharel, L. Xin, R. Dong, A. B. A. Dayang, H. Kanaya, and K. Yoshida, "60GHz-band low loss on-chip band pass filter with patterned ground shields for millimeter wave CMOS SoC," in *IEEE MTT-S Int. Microw. Symp. Dig.*, 2011, pp. 1-4.

[23] Y. Dong and T. Itoh, "Miniaturized dual-band substrate integrated waveguide filters using complementary split-ring resonators," in *IEEE MTT-S Int. Microw. Symp. Dig.*, 2011, pp. 1-4.

[24] D. Zelenchuk and V. Fusco, "Low insertion loss substrate integrated waveguide quasi-elliptic filters for V-band wireless personal area network applications," *IET Microw. Antennas Propag.*, vol. 5, pp. 921-927, 2011.

[25] W.-Y. Park and S. Lim, "Miniaturized substrate integrated waveguide (SIW) bandpass filter loaded with double-sided-complementary split

ring resonators (DS-CSRRs)," in *Proc. Eur. Microw. Conf. (EuMC)*, 2011, pp. 740-743.

[26] W. Shen, W.-Y. Yin, and X.-W. Sun, "Compact Substrate Integrated Waveguide (SIW) Filter With Defected Ground Structure," *IEEE Microw. Wireless Compon. Lett.*, vol. 21, pp. 83-85, 2011.

[27] L. Yo-Shen, Y. Chiou-Wen, and T. Chin-Lung, "On-Chip Single-to-Balanced Multicoupled Line Bandpass Filters With Good Selectivity," *IEEE Trans. Microw. Theory Tech.*, vol. 59, pp. 3322-3330, 2011.

[28] J. E. Page, J. Esteban, and C. Camacho-Penalosa, "Lattice Equivalent Circuits of Transmission-Line and Coupled-Line Sections," *IEEE Trans. Microw. Theory Tech.*, vol. 59, pp. 2422-2430, 2011.

[29] M. Kaixue and Y. Kiat-Seng, "New Ultra-Wide Stopband Low-Pass Filter Using Transformed Radial Stubs," *IEEE Trans. Microw. Theory Tech.*, vol. 59, pp. 604-611, 2011.

[30] Q.-L. Zhang, W.-Y. Yin, and S. He, "Evanescent-mode substrate integrated waveguide (SIW) filters implemented with complementary split ring resonators," *Prog. In Electromag. Res.*, vol. 111, pp. 419-432, 2011.

[31] A. Garcia-Lamperez and M. Salazar-Palma, "Single-Band to Multiband Frequency Transformation for Multiband Filters," *IEEE Trans. Microw. Theory Tech.*, vol. 59, pp. 3048-3058, 2011.

[32] W. S. Chang and C. Y. Chang, "Analytical Design of Microstrip Short-Circuit Terminated Stepped-Impedance Resonator Dual-Band Filters," *IEEE Trans. Microw. Theory Tech.*, vol. 59, pp. 1730-1739, 2011.

[33] A. K. Kunwer and S. Pal, "High Performance Wide Stopband Lowpass Filter Using Complementary Split Ring Resonators as Defected Ground Plane," in *Int. Conf. Devices Com.*, 2011, pp. 1-4.

[34] K. Ma and K. S. Yeo, "New Ultra-Wide Stopband Low-Pass Filter Using Transformed Radial Stubs," *IEEE Trans. Microw. Theory Tech.*, vol. 59, pp. 604-611, 2011.

[35] L. Ji-Chyun, L. Hsieh-Chih, Z. Bing-Hao, Y. Kuan-Dih, and C. Dau-Chyrh, "An Improved Equivalent Circuit Model for CSRR-Based Bandpass Filter Design With Even and Odd Modes," *IEEE Microw. Wireless Compon. Lett.*, vol. 20, pp. 193-195, 2010.

[36] S. Amari, F. Seyfert, and M. Bekheit, "Theory of Coupled Resonator Microwave Bandpass Filters of Arbitrary Bandwidth," *IEEE Trans. Microw. Theory Tech.*, vol. 58, pp. 2188-2203, 2010.

[37] Z. Qiao-Li, Y. Wen-Yan, H. Sailing, and W. Lin-Sheng, "Compact Substrate Integrated Waveguide (SIW) Bandpass Filter With Complementary Split-Ring Resonators (CSRRs)," *IEEE Microw. Wireless Compon. Lett.*, vol. 20, pp. 426-428, 2010.

[38] Y.-S. Lin, P.-C. Wang, C.-W. You, and P.-Y. Chang, "New designs of bandpass diplexer and switchplexer based on parallel-coupled bandpass filters," *IEEE Trans. Microw. Theory Tech.*, vol. 58, pp. 3417-3426, 2010.

[39] K. Ma and K. S. Yeo, "Novel low cost compact size planar low pass filters with deep skirt selectivity and wide stopband rejection," in *IEEE MTT-S Int. Microw. Symp. Dig.*, 2010, pp. 233-236.

[40] D. Yuandan and T. Itoh, "Substrate Integrated Waveguide Loaded by Complementary Split-Ring Resonators for Miniaturized Diplexer Design," *IEEE Microw. Wireless Compon. Lett.,* vol. 21, pp. 10-12, 2011.

[41] H. Miyake, S. Kitazawa, T. Ishizaki, T. Yamada, and Y. Nagatomi, "A miniaturized monolithic dual band filter using ceramic lamination technique for dual mode portable telephones," in *IEEE MTT-S Int. Microw. Symp. Dig.*, 1997, pp. 789-792 vol.2.

[42] C. F. Chen, T. Y. Huang, and R. B. Wu, "Design of Dual- and Triple-Passband Filters Using Alternately Cascaded Multiband Resonators," *IEEE Trans. Microw. Theory Tech.,* vol. 54, pp. 3550-3558, 2006.

[43] C.-S. Kim, J.-S. Park, D. Ahn, and J.-B. Lim, "A novel 1-D periodic defected ground structure for planar circuits," *IEEE Microw. Guided Wave Lett.,* vol. 10, pp. 131-133, 2000.

[44] D. Ahn, J. S. Park, C. S. Kim, J. Kim, Y. Qian, and T. Itoh, "A design of the low-pass filter using the novel microstrip defected ground structure," *IEEE Trans. Microw. Theory Tech.,* vol. 49, pp. 86-93, 2001.

[45] J.-S. Lim, C.-S. Kim, J.-S. Park, D. Ahn, and S. Nam, "Design of 10 dB 90° branch line coupler using microstrip line with defected ground structure," *IET Electronics Lett.,* vol. 36, pp. 1784-1785, 2000.

[46] J.-S. Lim, S.-W. Lee, C.-S. Kim, J.-S. Park, D. Ahn, and S. Nam, "A 4:1 unequal Wilkinson power divider," *IEEE Microw. Wireless Compon. Lett.,* vol. 11, pp. 124-126, 2001.

[47] M. Abdolhamidi and M. Shahabadi, "X-Band Substrate Integrated Waveguide Amplifier," *IEEE Microw. Wireless Compon. Lett.,* vol. 18, pp. 815-817, 2008.

[48] J.-S. Lim, Y.-T. Lee, J.-H. Han, J.-S. Park, D. Ahn, and S. Nam, "A technique for reducing the size of amplifiers using defected ground structure," in *IEEE MTT-S Int. Microw. Symp. Dig.*, 2002, pp. 1153-1156.

[49] J.-S. Lim, J.-S. Park, Y.-T. Lee, D. Ahn, and S. Nam, "Application of defected ground structure in reducing the size of amplifiers," *IEEE Microw. Wireless Compon. Lett.,* vol. 12, pp. 261-263, 2002.

[50] A. B. Abdel-Rahman, A. K. Verma, A. Boutejdar, and A. S. Omar, "Control of bandstop response of Hi-Lo microstrip low-pass filter using slot in ground plane," *IEEE Trans. Microw. Theory Tech.,* vol. 52, pp. 1008-1013, 2004.

[51] A. Balalem, A. R. Ali, J. Machac, and A. Omar, "Quasi-Elliptic Microstrip Low-Pass Filters Using an Interdigital DGS Slot," *IEEE Microw. Wireless Compon. Lett.,* vol. 17, pp. 586-588, 2007.

[52] H.-J. Chen, *et al.*, "A novel cross-shape DGS applied to design ultra-wide stopband low-pass filters," *IEEE Microw. Wireless Compon. Lett.*, vol. 16, pp. 252-254, 2006.
[53] Y.-C. Chen, A.-S. Liu, and R.-B. Wu, "A wide-stopband low-pass filter design based on multi-period taper-etched EBG structure," in *Microw. Conf. Proc.*, 2005, p. 3 pp.
[54] Y. Chung, S.-S. Jeon, S. Kim, D. Ahn, J.-I. Choi, and T. Itoh, "Multifunctional microstrip transmission lines integrated with defected ground structure for RF front-end application," *IEEE Trans. Microw. Theory Tech.*, vol. 52, pp. 1425-1432, 2004.
[55] J. S. Lim, C. S. Kim, D. Ahn, Y. C. Jeong, and S. Nam, "Design of Low-Pass Filters Using Defected Ground Structure," *IEEE Trans. Microw. Theory Tech.*, vol. 53, pp. 2539-2545, 2005.
[56] C.-S. Kim, J.-S. Lim, S. Nam, K.-Y. Kang, and D. Ahn, "Equivalent circuit modelling of spiral defected ground structure for microstrip line," *IET Electronics Lett.*, vol. 38, pp. 1109-1110, 2002.
[57] J.-S. Lim, C.-S. Kim, Y.-T. Lee, D. Ahn, and S. Nam, "A spiral-shaped defected ground structure for coplanar waveguide," *IEEE Microw. Wireless Compon. Lett.*, vol. 12, pp. 330-332, 2002.
[58] J. Yang and W. Wu, "Compact Elliptic-Function Low-Pass Filter Using Defected Ground Structure," *IEEE Microw. Wireless Compon. Lett.*, vol. 18, pp. 578-580, 2008.
[59] D.-J. Woo, T.-K. Lee, J.-W. Lee, C.-S. Pyo, and W.-K. Choi, "Novel U-slot and V-slot DGSs for bandstop filter with improved Q factor," *IEEE Trans. Microw. Theory Tech.*, vol. 54, pp. 2840-2847, 2006.
[60] R. C. Daniels and R. W. Heath, "60 GHz wireless communications: emerging requirements and design recommendations," *IEEE Vehi. Technol. Mag.*, vol. 2, pp. 41-50, 2007.
[61] W. J. Fleming, "New Automotive Sensors-A Review," *IEEE Sensors Jour.*, vol. 8, pp. 1900-1921, 2008.
[62] L. Yujiri, "Passive Millimeter Wave Imaging," in *IEEE MTT-S Int. Microw. Symp. Dig.*, pp. 98-101.
[63] K. Mizuno, *et al.*, "Millimeter-Wave Imaging Technologies and Their Applications," in *IEEE Int. Vac. Electronics Conf.*, 2007, pp. 1-2.
[64] F. Shigeki, "Waveguide line," *Japan Patent*, pp. 06-053 711, Feb. 25 1994.
[65] J. Hirokawa and M. Ando, "Single-layer feed waveguide consisting of posts for plane TEM wave excitation in parallel plates," *IEEE Transactions on Antennas and Propagation*, vol. 46, pp. 625-630, 1998.
[66] H. Uchimura, T. Takenoshita, and M. Fujii, "Development of a “laminated waveguide&rdquo," *IEEE Trans. Microw. Theory Tech.*, vol. 46, pp. 2438-2443, 1998.
[67] D. Deslandes and K. Wu, "Single-substrate integration technique of planar circuits and waveguide filters," *IEEE Trans. Microw. Theory Tech.*, vol. 51, pp. 593-596, 2003.

[68] F. Xu and K. Wu, "Guided-wave and leakage characteristics of substrate integrated waveguide," *IEEE Trans. Microw. Theory Tech.*, vol. 53, pp. 66-73, 2005.

[69] D. Deslandes and K. Wu, "Accurate modeling, wave mechanisms, and design considerations of a substrate integrated waveguide," *IEEE Trans. Microw. Theory Tech.*, vol. 54, pp. 2516-2526, 2006.

[70] K. Wu, "Towards system-on-substrate approach for future millimeter-wave and photonic wireless applications," in *Asia-Pacific Microw. Conf.*, 2006, pp. 1895-1900.

[71] H. J. Tang, W. Hong, Z. C. Hao, J. X. Chen, and K. Wu, "Optimal design of compact millimetre-wave SIW circular cavity filters," *IET Electronics Lett.*, vol. 41, pp. 1068-1069, 2005.

[72] J.-X. Chen, W. Hong, Z.-C. Hao, H. Li, and K. Wu, "Development of a low cost microwave mixer using a broad-band substrate integrated waveguide (SIW) coupler," *IEEE Microw. Wireless Compon. Lett.*, vol. 16, pp. 84-86, 2006.

[73] Y. Cassivi and K. Wu, "Low cost microwave oscillator using substrate integrated waveguide cavity," *IEEE Microw. Wireless Compon. Lett.*, vol. 13, pp. 48-50, 2003.

[74] C. Zhang, J. Xu, Z. Yu, and Y. Zhu, "Ka-Band Substrate IntegratedWaveguide Gunn Oscillator," *IEEE Microw. Wireless Compon. Lett.*, vol. 18, pp. 461-463, 2008.

[75] H. Jin and G. Wen, "A Novel Four-Way Ka-Band Spatial Power Combiner Based on HMSIW," *IEEE Microw. Wireless Compon. Lett.*, vol. 18, pp. 515-517, 2008.

[76] L. Yan, W. Hong, G. Hua, J. Chen, K. Wu, and T. J. Cui, "Simulation and experiment on SIW slot array antennas," *IEEE Microw. Wireless Compon. Lett.*, vol. 14, pp. 446-448, 2004.

[77] D. Deslandes and K. Wu, "Substrate integrated waveguide leaky-wave antenna: concept and design considerations," *Proc. Asia-Pacific Microwave Conf. (APMC'05),* 2005.

[78] Y. Cassivi, L. Perregrini, P. Arcioni, M. Bressan, K. Wu, and G. Conciauro, "Dispersion characteristics of substrate integrated rectangular waveguide," *IEEE Microwave and Wireless Components Letters*, vol. 12, pp. 333-335, 2002.

[79] F. Xu, Y. Zhang, W. Hong, K. Wu, and T. J. Cui, "Finite-difference frequency-domain algorithm for modeling guided-wave properties of substrate integrated waveguide," *IEEE Trans. Microw. Theory Tech.*, vol. 51, pp. 2221-2227, 2003.

[80] L. Yan, W. Hong, K. Wu, and T. J. Cui, "Investigations on the propagation characteristics of the substrate integrated waveguide based on the method of lines," *IET Microw. Antennas Propag.*, vol. 152, pp. 35-42, 2005.

[81] M. Bozzi, L. Perregrini, and W. Ke, "Modeling of Conductor, Dielectric, and Radiation Losses in Substrate Integrated Waveguide by the

Boundary Integral-Resonant Mode Expansion Method," *IEEE Trans. Microw. Theory Tech.*, vol. 56, pp. 3153-3161, 2008.

[82] M. Bozzi, M. Pasian, L. Perregrini, and K. Wu, "On the losses in substrate integrated waveguides and cavities," *Int. J. Microw. Wirel. Technol.*, vol. 1, pp. 395-401, 2001.

[83] A. F. Horn, J. W. Reynolds, and J. C. Rautio, "Conductor profile effects on the propagation constant of microstrip transmission lines," in *IEEE MTT-S Int. Microw. Symp. Dig.*, 2010, pp. 868-871.

[84] N. Grigoropoulos, B. Sanz-Izquierdo, and P. R. Young, "Substrate integrated folded waveguides (SIFW) and filters," *IEEE Microwave and Wireless Components Letters*, vol. 15, pp. 829-831, 2005.

[85] Q. Lai, F. C., W. Hong, and V. R., "Characterization of the Propagation Properties of the Half-Mode Substrate Integrated Waveguide," *IEEE Trans. Microw. Theory Tech.*, vol. 57, pp. 1996-2004, 2009.

[86] G. H. Zhai, *et al.*, "Folded Half Mode Substrate Integrated Waveguide 3 dB Coupler," *IEEE Microw. Wireless Compon. Lett.*, vol. 18, pp. 512-514, 2008.

[87] M. Bozzi, D. Deslandes, P. Arcioni, L. Perregrini, K. Wu, and G. Conciauro, "Efficient analysis and experimental verification of substrate integrated slab waveguides for wideband microwave applications," *Int. J. RF Microw. Comput. Aided Eng.*, vol. 15, pp. 296-306, 2005.

[88] W. Che, C. Li, R. P., and Y. L. Chow, "Propagation and band broadening effect of planar integrated ridged waveguide in multilayer dielectric substrates," in *IEEE MTT-S Int. Microw. Symp. Dig.*, 2008, pp. 217-220.

[89] M. Bozzi, S. A. Winkler, and K. Wu, "Broadband and compact ridge substrate-integrated waveguides," *IET Microw. Antennas Propag.*, vol. 4, pp. 1965-1973, 2010.

[90] G. L. Matthaei, L. Young, and E. M. T. Jones, *Microwave Filters, Impedance-Matching Networks, and Coupling Structures*: McGraw-Hill, Inc., 1964.

[91] C.-S. Kim, *et al.*, "The equivalent circuit modeling of defected ground structure with spiral shape," in *IEEE MTT-S Int. Microw. Symp. Dig.*, 2002, pp. 2125-2128.

[92] Y. L. Zhang, W. Hong, K. Wu, J. X. Chen, and H. J. Tang, "Novel substrate integrated waveguide cavity filter with defected ground structure," *IEEE Trans. Microw. Theory Tech.*, vol. 53, pp. 1280-1287, 2005.

[93] S.-C. Lin, P.-H. Deng, Y.-S. Lin, C.-H. Wang, and C. H. Chen, "Wide-stopband microstrip bandpass filters using dissimilar quarter-wavelength stepped-impedance resonators," *IEEE Trans. Microw. Theory Tech.*, vol. 54, pp. 1011-1018, 2006.

[94] M. Makimoto and S. Yamashita, "Bandpass Filters Using Parallel Coupled Stripline Stepped Impedance Resonators," *IEEE Trans. Microw. Theory Tech.*, vol. 28, pp. 1413-1417, 1980.

[95] M. Kaixue, M. Jian-Guo, Y. Kiat Seng, and A. V. Do, "A compact size coupling controllable filter with separate electric and magnetic coupling paths," *IEEE Trans. Microw. Theory Tech.*, vol. 54, pp. 1113-1119, 2006.
[96] J.-S. Hong and M. J. Lancaster, *Microstrip Filter for RF/Microwave Applications*: New York: Wiley, 2001.
[97] D. M. Pozar, *Microwave Engineering, 4th ed*: New York: Wiley, 2012.
[98] C. Monzon, "A small dual-frequency transformer in two sections," *IEEE Trans. Microw. Theory Tech.*, vol. 51, pp. 1157-1161, 2003.
[99] K. Ma, J.-G. Ma, K. S. Yeo, and M. A. Do, "A compact size coupling controllable filter with separate electric and magnetic coupling paths," *IEEE Trans. Microw. Theory Tech.*, vol. 54, pp. 1113-1119, 2006.
[100] L. Huang, I. D. Robertson, and N. Yuan, "Substrate integrated waveguide filters with face-to-face broadside-coupled complementary split ring resonators," in *Proc. Eur. Microw. Conf. (EuMC)*, 2013, pp. 29-32.
[101] Y. Dong, T. Yang, and T. Itoh, "Substrate Integrated Waveguide Loaded by Complementary Split-Ring Resonators and Its Applications to Miniaturized Waveguide Filters," *IEEE Trans. Microw. Theory Tech.*, vol. 57, pp. 2211-2223, 2009.
[102] F. Falcone, T. Lopetegi, J. D. Baena, R. Marques, F. Martin, and M. Sorolla, "Effective negative-ε stopband microstrip lines based on complementary split ring resonators," *IEEE Microw. Wireless Compon. Lett.*, vol. 14, pp. 280-282, 2004.
[103] Y. Cassivi, L. Perregrini, P. Arcioni, M. Bressan, K. Wu, and G. Conciauro, "Dispersion characteristics of substrate integrated rectangular waveguide," *IEEE Microw. Wireless Compon. Lett.*, vol. 12, pp. 333-335, 2002.
[104] D. Deslandes and W. Ke, "Single-substrate integration technique of planar circuits and waveguide filters," *IEEE Trans. Microw. Theory Tech.*, vol. 51, pp. 593-596, 2003.
[105] L. S. Wu, J. F. Mao, W. Y. Yin and Y. X. Guo, "A dual-band filter using stepped-impedance resonator (SIR) embedded into substrate integrated waveguide (SIW)," *2010 IEEE Electrical Design of Advanced Package & Systems Symposium*, Singapore, 2010, pp. 1-4.
[106] J. Shi and Q. Xue, "Novel Balanced Dual-Band Bandpass Filter Using Coupled Stepped-Impedance Resonators," *IEEE Microwave and Wireless Components Letters*, vol. 20, no. 1, pp. 19-21, Jan. 2010.
[107] W. Shen, W.-Y. Yin, and X.-W. Sun, "Miniaturized dual-band substrate integrated waveguide filter with controllable bandwidths," *IEEE Microw. Wireless Compon. Lett.*, vol. 21, no. 8, pp. 418–420, Aug. 2011.
[108] B. J. Chen, T. M. Shen, and R. B. Wu, "Dual-band vertically stacked laminated waveguide filter design in LTCC technology," *IEEE Trans. Microw. Theory Techn.*, vol. 57, no. 6, pp. 1554–1562, Jun. 2009.

[109] X. P. Chen, K. Wu, and Z. L. Li, "Dual-band and triple-band substrate integrated waveguide filters with chebyshev and quasi-elliptic responses," *IEEE Trans. Microw. Theory Techn.*, vol. 55, no. 12, pp. 2569–2578, Dec. 2007.

[110] Y. Shen, H. Wang, W. Kang, and W. Wu, "Dual-band SIW differential bandpass filter with improved common-mode suppression," *IEEE Microw. Wireless Compon. Lett.*, vol. 25, no. 2, pp. 100–102, Feb. 2015.

[111] L. Gao, X. Y. Zhang, B.-J. Hu, and Q. Xue, "Novel multi-stub loaded resonators and their applications to various bandpass filters," *IEEETrans. Microw. Theory Techn.*, vol. 62, no. 5, pp. 1162–1172, May 2014.

[112] T. Yan and X.-H. Tang, "Substrate integrated waveguide dual-band bandpass filter with complementary modified split-ring resonators," in Proc. IEEE Int. Wireless Symp. (IWS), Apr. 2015, pp. 1–4.